BioPixel Reveals How Podosomes and Microtubule +TIPs Regulate Intracellular Transport

Dissertation for the attainment of the doctoral degree
at the Faculty of Mathematics, Computer Science and Natural Sciences
Department of Biology
of the University of Hamburg

submitted by

Bryan Gerhard Jose Barcelona

from Burbank, California, USA

Universität Hamburg
DER FORSCHUNG | DER LEHRE | DER BILDUNG

UKE
HAMBURG

Hamburg

2025

University of Hamburg

Faculty: Mathematics, Informatics and Natural Sciences
Department: Biology

First Reviewer: Prof. Dr. rer. nat. Stefan Linder
Second Reviewer: Prof. Dr. rer. nat. Wolfgang Streit
Principal Supervisor: Prof. Dr. rer. nat. Stefan Linder

This work was conducted under the supervision of Prof. Dr. Stefan Linder at the Institute for Medical Microbiology, Virology and Hygiene of the University Medical Center Hamburg-Eppendorf between June 2022 and March 2025.

Date of Defense (Disputation): August 22, 2025

Acknowledgements

I would first like to express my deepest gratitude to my supervisor, Prof. Dr. rer. nat. Stefan Linder, for granting me the opportunity to work on this captivating and challenging project. His guidance, expertise, and dedicated efforts in reviewing this thesis have been pivotal in shaping its outcome.

I am also grateful to Prof. Dr. rer. nat. Wolfgang Streit for agreeing to review this thesis. His willingness to lend his expertise is greatly appreciated.

A heartfelt thank you goes to the members of our laboratory: Sven, Kevin, Kostja, Fan, Qifan, and Pasquale. Your collaboration, support, and camaraderie made the lab a vibrant and motivating environment, even when experiments pushed our limits. I also extend my appreciation to former lab members Lars, Rawan, Adria, Marie, Andrea, Kathrin, and Artur for their contributions and the shared moments that enriched my time in the lab.

Special thanks go to my fellow students Janina, Emily, Moritz, Felix, Sebastian, Daria, and Samantha, who have been part of my academic journey throughout my master's and doctoral studies. Your encouragement and companionship have been invaluable.

I am deeply grateful to my oldest friends Steffi, Marco, Jonas, and Caschi, whose steadfast friendship has been a constant source of strength.

To my family, I owe an immense debt of gratitude. My siblings Kevin, Kimberly, Marie, and Dennis, along with their partners Maureen and Nicole, and my stepfather Henning, have provided unwavering support. I dedicate this work to the memory of my late father and Julie, whose love continues to guide me. Above all, I am profoundly thankful for my mother, whose endless encouragement and belief in me have been my greatest motivation.

Declaration of authorship

English declaration of authorship

I hereby declare and affirm that this doctoral dissertation is my own work and that I have not used any aids and sources other than those indicated. If electronic resources based on generative artificial intelligence (gAI) were used in the course of writing this dissertation, I confirm that my own work was the main and value-adding contribution and that complete documentation of all resources used is available in accordance with good scientific practice. I am responsible for any erroneous or distorted content, incorrect references, violations of data protection and copyright law or plagiarism that may have been generated by the gAI.

Hamburg, May 21st, 2025

_____
Bryan Gerhard Jose Barcelona, M.Sc.

German declaration of authorship

Hiermit versichere ich an Eides statt, die vorliegende Dissertationsschrift selbst verfasst und keine anderen als die angegebenen Hilfsmittel und Quellen benutzt zu haben. Sofern im Zuge der Erstellung der vorliegenden Dissertationsschrift generative Künstliche Intelligenz (gKI) basierte elektronische Hilfsmittel verwendet wurden, versichere ich, dass meine eigene Leistung im Vordergrund stand und dass eine vollständige Dokumentation aller verwendeten Hilfsmittel gemäß der Guten wissenschaftlichen Praxis vorliegt. Ich trage die Verantwortung für eventuell durch die gKI generierte fehlerhafte oder verzerrte Inhalte, fehlerhafte Referenzen, Verstöße gegen das Datenschutz- und Urheberrecht oder Plagiate.

Hamburg, der 21. Mai 2025

_____
Bryan Gerhard Jose Barcelona, M.Sc.

Abstract

Podosomes are dynamic, actin-rich adhesive structures found in monocyte-derived cells such as macrophages, dendritic cells, and osteoclasts. These specialized cellular domains coordinate cellular motility, extracellular matrix remodeling, and intracellular trafficking by integrating cytoskeletal elements with membrane dynamics. Structurally, podosomes consist of a dense F-actin core surrounded by an adhesion ring containing integrins and cytoskeletal linker proteins. While their actin dynamics have been extensively studied, the mechanisms integrating podosome activity with microtubule-dependent transport and microtubule plus-end tracking proteins (+TIPs) remain incompletely understood.

This work introduces BioPixel, a computational platform combining deep learning-based podosome segmentation with spatial analysis of protein interactions, providing a robust alternative to existing tools like ImageJ, Poji, and proprietary software. BioPixel was developed to overcome limitations of conventional analysis methods, which rely on manual thresholding and lack 3D quantification capabilities. The platform offers dual functionality: precise quantification of protein localization patterns relative to podosome architecture, and statistical mapping of proximity ligation assay (PLA) signals with single-molecule resolution.

When applied to macrophage podosomes, this integrated approach generated comprehensive localization profiles for actin regulators including drebrin, resolving distinct subdomain targeting patterns. Structure-function analysis revealed that the coiled-coil (CC), helical (Hel), and C-terminal regions of drebrin are collectively required for cap localization, while the ADFH and proline-rich (PP) domains are dispensable. The platform's PLA analysis module identified preferential formation of drebrin-EB3-clathrin complexes at podosome peripheries, functionally linking actin remodeling to microtubule-based transport through interaction with the +TIP protein EB3. The spatial analysis provided by BioPixel suggests these molecular complexes may play a key role in podosome functions related to matrix interactions and cytoskeletal coordination.

This work provides evidence for podosomes as potential integrated hubs for cytoskeletal crosstalk and offers new insights into the spatial organization of molecular interactions within these structures. The BioPixel platform combines the flexibility of open-source tools with the precision typically associated with proprietary software, eliminating the need for multiple specialized programs. While initially developed for podosome research, its modular architecture is designed for expansion to diverse biological questions. This unified approach provides quantitative 3D mapping of protein organization and interactions at subcellular resolution, advancing studies of molecular architecture in both physiological and pathological contexts.

Kurzfassung

Podosomen sind dynamische, actinreiche Adhäsionsstrukturen, die in von Monozyten abgeleiteten Zellen wie Makrophagen, dendritischen Zellen und Osteoklasten vorkommen. Diese spezialisierten zellulären Domänen koordinieren Zellmotilität, extrazelluläre Matrixremodellierung und intrazellulären Transport, indem sie zytoskelettale Elemente mit Membrandynamik integrieren. Strukturell bestehen Podosomen aus einem dichten F-Actin-Kern, der von einem Adhäsionsring aus Integrinen und zytoskelettalen Verbindungsproteinen umgeben ist. Während die Actindynamik in Podosomen umfassend untersucht wurde, sind die Mechanismen, die Podosomen mit dem mikrotubuliabhängigen Transport und Mikrotubuli-Plus-End-Tracking-Proteinen (+TIPs) verknüpfen, bislang nur unvollständig verstanden.

Im Rahmen dieser Arbeit wurde BioPixel entwickelt, eine rechnergestützte Plattform, die Deep-Learning-basierte Segmentierung von Podosomen mit räumlicher Analyse von Proteininteraktionen kombiniert. Sie stellt eine leistungsfähige Open-Source-Alternative zu bestehenden Werkzeugen wie ImageJ, Poji und proprietärer Software dar. BioPixel überwindet die Einschränkungen herkömmlicher Analysemethoden, die häufig auf manueller Schwellenwertsetzung beruhen und keine 3D-Quantifizierung ermöglichen. Die Plattform bietet zwei Hauptfunktionen: präzise Quantifizierung von Proteinlokalisierung relativ zur Podosomenarchitektur sowie statistische Kartierung von Proximity Ligation Assay (PLA)-Signalen mit Einzelmolekülauflösung.

Die Anwendung von BioPixel auf Podosomen in Makrophagen ermöglichte umfassende Lokalisierungsanalysen von Actin-regulierenden Proteinen wie Drebrin und die Identifikation distinkter Subdomänen-Muster. Struktur-Funktions-Analysen zeigten, dass die Coiled-Coil-(CC)-, Helix-(Hel)- und C-terminalen Regionen gemeinsam für die Lokalisierung von Drebrin an die Podosomenkappe erforderlich sind, während die ADFH- und Prolin-reichen (PP) Domänen dafür entbehrlich sind. Die PLA-Analyse offenbarte eine bevorzugte Ausbildung von Drebrin-EB3-Clathrin-Komplexen an den Podosomenrändern, was auf eine funktionelle Verbindung zwischen Actin-Remodellierung und mikrotubuli-basiertem Transport über die Interaktion mit dem +TIP-Protein EB3 hinweist. Die räumliche Analyse legt nahe, dass diese molekularen Komplexe eine zentrale Rolle in der Regulation podosomenvermittelter Matrixinteraktionen spielen könnten.

Diese Arbeit liefert neue Hinweise darauf, dass Podosomen als integrierte Schaltstellen für das Zusammenspiel zytoskelettaler Netzwerke fungieren, und eröffnet neue Einblicke in die räumliche Organisation molekularer Interaktionen innerhalb dieser Strukturen. Die BioPixel-Plattform vereint die Flexibilität von Open-Source-Software mit der Präzision kommerzieller Speziallösungen und macht den Einsatz mehrerer Programme überflüssig. Obwohl ursprünglich für die Podosomenforschung entwickelt, ist ihre modulare Architektur auf verschiedenste biologische Fragestellungen übertragbar. Dieser integrierte Ansatz ermöglicht eine quantitative 3D-Kartierung von Proteinorganisation und -interaktionen auf subzellulärer Ebene und erweitert das Verständnis molekularer Architektur in physiologischen und pathologischen Kontexten.

Contents

1   Introduction

1.1   Macrophages

As phagocytic cells essential for tissue homeostasis Ilya Metchnikoff identified macrophages in the 19th century as vital components of innate immunity and inflammatory responses (Metchnikoff, 1883; Tauber, 2003). Macrophages develop from tissue-migrating monocytes which differentiate to perform multiple tasks such as phagocytosis and antigen presentation as well as tissue remodeling and homeostasis maintenance (Sica and Mantovani, 2012; Viola et al., 2019). Through phagocytosis, macrophages can ingest and break down cellular debris, including apoptotic cells through the specialized process of efferocytosis (deCathelineau and Henson, 2003), as well as foreign materials and pathogens. Macrophages use pattern recognition receptors (PRRs) to detect pathogens and destroy them through phagocytosis where they isolate the pathogens in a hostile environment of reactive oxygen species (ROS) and reactive nitrogen species (RNS), acidification, nutrient deprivation and antimicrobial peptides and coordinate immune responses by releasing cytokines and attracting additional immune cells (Weiss and Schaible, 2015). During the process of phagocytosis ROS together with RNS destroy pathogens (Guo et al., 2024). Macrophages function as antigen-presenting cells to T-cells which bridges the gap between innate and adaptive immunity (Hohl et al., 2009). Through cytokine and growth factor secretion macrophages control both cell proliferation processes and the rebuilding of tissue (Wynn and Vannella, 2016) along with extracellular matrix (ECM) modification (Voisin et al., 2023).

The classification of macrophages depends on their basic function and activation state. This classification system identifies three main types, namely classically activated (M1), wound-healing (a subset of alternatively activated (M2)), and regulatory (Mregs) (Mosser and Edwards, 2008). Macrophages display plasticity by changing their phenotypes according to environmental signals (Rasheed and Rayner, 2021). M1 macrophages function to generate inflammation while clearing pathogens and suppressing tumors whereas M2 macrophages work to suppress inflammation and aid tissue repair alongside angiogenesis (Mantovani et al., 2005). Macrophage activation states form a continuous range instead of separate discrete states (Murray and Wynn, 2011). Tissue-resident macrophages develop from embryonic precursors in addition to monocytes (Ginhoux and Guilliams, 2016). Specialized macrophages exist in specific tissues with examples including microglia found in the brain and Kupffer cells located in the liver along with alveolar macrophages in the lungs (Hume, 2006).

Macrophages move through tissues to reach infection or injury sites by employing various migration strategies (van Goethem et al., 2010). In two-dimensional environments macrophages migrate via a sequence of adhesion events controlled by selectins and integrins but within three-dimensional environments they demonstrate either amoeboid movement which relies on Rho-ROCK signaling or mesenchymal migration which depends on protease activity and involves extracellular matrix degradation and podosome formation (Gao et al., 2021). Macrophages with dysfunctional regulation support disease development in chronic inflammation and autoimmune disorders and cancer through their role in creating an immunosuppressive environment (Di Benedetto et al., 2019). In cancer, tumor-associated macrophages (TAMs) are a major component of the tumor microenvironment and can polarize into two main subtypes: The M1 subtype of macrophages functions as anti-tumor and cytotoxic while the M2 subtype acts as pro-tumor and immunosuppressive. TAMs are essential players in tumor progression through their involvement in metastasis and angiogenesis and demonstrate their function as dual agents who act as both guardians and adversaries in disease development (Pan et al., 2020).

1.2 Cytoskeleton

In 1931 French embryologist Paul Wintrebert first introduced the concept of a cytoskeleton which he referred to as "cytosquelette" (Frixione, 2000). While the term "skeleton" implies a fixed structure, the cytoskeleton remains a flexible and responsive framework which adjusts its organization based on the requirements of the cell. The cytoskeleton maintains cell shape and enables cell movement while also supporting intracellular traffic functions (Resnik et al., 2019). The cytoskeleton demonstrates significant involvement in cellular division and intracellular signaling as well as molecular trafficking functions which are partly mediated by crosstalk among the separate cytoskeletal systems (Huber et al., 2015). The cytoskeleton produces forces that enable both cellular movement and shape transformation (Fletcher and Mullins, 2010).

The cytoskeleton is composed of three primary components (microfilaments, intermediate filaments, and microtubules) which demonstrate fast growth and disassembly in response to cellular demands (McKinley et al., 2015). In addition, septins, a family of GTP-binding proteins that form filamentous structures, are increasingly recognized as an important part of the cytoskeletal system, contributing to processes such as cell division and membrane organization (Mostowy and Cossart, 2012). The cytoskeleton maintains a state of continuous restructuring which serves as its defining trait to allow quick responses to both internal and external signals (Pollard and Borisy, 2003).

Microtubules (MTs) consist of α- and β-tubulin dimers that form polymer-like hollow cylinders (Desai and Mitchison, 1997). MTs extend to 50 micrometers in length and display an outer diameter that spans 23 to 27 nanometers (Ledbetter and Porter, 1963) while their inner diameter measures between 11 and 15 nanometers (Chalfie and Thomson, 1979). MTs form crucial pathways inside cells that allow motor proteins such as kinesins and dyneins to transport organelles, vesicles, and other cellular materials along defined routes.

The heterogeneous polymers that form intermediate filaments (IFs) consist of multiple protein types such as vimentin, keratin, desmin, synemin, syncoilin, nestin, and lamin (Herrmann et al., 2007). The typical diameter of these structures measures about 10 nm (Ishikawa et al., 1968). Cells receive mechanical stability from intermediate filaments which helps them manage mechanical stress and sustain their structure unlike microtubules.

In most cells actin is the most abundant protein accounting for 1-5% of a typical cells' protein mass while specialized muscle cells can contain up to 10% of actin. Microfilaments form linear polymers in the cell and play a key role in cytoskeletal organization and function (Lodish et al., 2016).

The cytoskeleton functions as a dynamic network that continuously remodels to facilitate cellular activities. Through its complex network of microtubules and intermediate filaments combined with microfilaments the cell achieves structural stability while enabling effective molecular transport and adapting quickly to environmental and physiological shifts.

1.3   Actin

Albert Szent-Györgyi's laboratory discovered actin for the first time in 1942 (Bugyi and Kellermayer, 2020). This protein occurs most frequently in eukaryotic cells where it serves crucial functions in the structure and operation of cells (Lodish et al., 2016). Actin serves primarily as building blocks of linear polymers called microfilaments which support cellular structure and enable internal cellular activities.

Actin exists in two major forms: The monomeric globular actin (G-actin) assembles into the polymerized filamentous actin (F-actin) which forms linear microfilaments. The conversion from G-actin to F-actin depends on adenosine triphosphate (ATP) hydrolysis which regulates the polymerization and depolymerization dynamics (Straub and Feuer, 1950; Korn, 1982). Actin polymerization happens in three distinct stages. During the nucleation phase actin monomers aggregate to form small oligomers. The rate-limiting step of this process is the formation of a stable polymerization nucleus (Cooper, 2000) as dimers and trimers show inherent instability. The second phase termed elongation features actin filaments that grow rapidly while showing polarity as their barbed or plus-end extends faster than the pointed or minus-end which grows slower. Treadmilling represents the last phase during which actin monomers continuously attach at the barbed end as they detach from the pointed end to maintain dynamic equilibrium inside the cell (Wegner, 1976).

Vertebrates express six unique isoforms of actin, demonstrating its structural diversity. Skeletal muscle, cardiac muscle, and aortic smooth muscle contain three α-actin isoforms, which form the vascular α-actin group. In addition, there is one cytoplasmic β-isoform and two γ-isoforms. One γ-isoform is cytoplasmic, while the other is found in smooth muscle and is referred to as centric γ-actin. Various pathological conditions arise from mutations in these isoforms. Myopathy and angiopathy-related defects result from α-actin defects while mutations in β-actin and γ-actin can lead to cancer (Lohr et al., 2012), deafness, and developmental disorders (Procaccio et al., 2006; Hundt et al., 2014).

Actin generates cytokinetic structures like the contractile ring (Miller, 2011) and
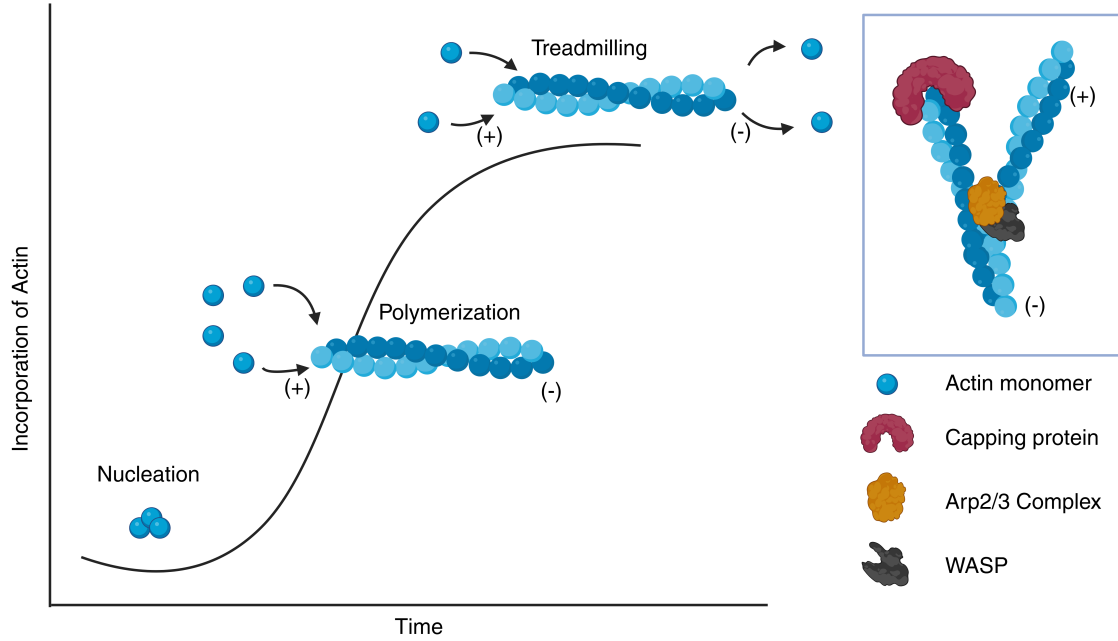
Figure 1.1: **Dynamics of Actin Filament Assembly and Branching.** (Left) Time course of actin polymerization showing three characteristic phases: initial nucleation (lag phase), rapid filament elongation (growth phase), and dynamic equilibrium between monomer addition and dissociation (steady state). Filament growth occurs preferentially at the barbed end (+), while depolymerization dominates at the pointed end (-). (Right) Branching mechanism mediated by the Arp2/3 complex. The activated Arp2/3 complex binds to existing filaments and initiates daughter filament formation at 70° angles. This process requires activation by WASP family proteins, which induce conformational changes in the Arp2/3 complex to enable new filament nucleation. (adapted from García Arguinzonis (2003))

helps maintain adherens and tight junctions with an actin circumferential belt (Niessen, 2007). It is also involved in forming cup-shaped invaginations such as phagocytic and macropinocytic cups (Swanson, 2008) and supporting cellular protrusions like lamellipo-dia, filopodia, invadopodia, and **podosomes** (Alblazi and Siar, 2015).

Actin polymerization regulation depends critically on the actin-related protein 2/3 (Arp2/3) complex which enables polymerization by creating daughter filaments from mother filaments at a seventy-degree angle. This mechanism enables branched network formation while serving a critical function in cytoskeleton restructuring (Mullins et al., 1998). Formins play a role in developing long unbranched actin filaments by initiating polymerization at the barbed end and blocking capping to regulate filament extension (Goode and Eck, 2007).

Specific proteins contribute to actin turnover by performing severing, while others regulate dynamics through processes like nucleation, capping, or stabilization. Gelsolin emerges as a key protein since it slices actin filaments through calcium-dependent mecha-nisms. The activity results in the creation of polymerization-ready ends which enable actin to quickly remodel according to cellular requirements (Sun et al., 1999). Cofilin functions as a key promoter of actin turnover through the severing of filaments which simultaneously improves polymerization and depolymerization. This dynamic remodeling is critical for the formation and function of podosomes, actin-rich adhesive structures that facilitate cell motility and extracellular matrix degradation. Podosomes allow cells to migrate through

11

tissue barriers and respond to external cues by dynamically assembling and disassembling their actin cores.

Actin stabilization relies on regulatory proteins which manage its dynamic properties. Tropomyosins attach across actin filaments lengthwise to strengthen their structural stability while facilitating connections between actin-binding proteins. The actin structure maintains its integrity through this regulatory mechanism while enabling precise reorganization based on cellular requirements (Khaitlina, 2015).

Actin regulation involves complex signaling pathways, including GTP-binding proteins, kinases, and phosphatases, which coordinate dynamic processes such as actin turnover, cytoskeletal remodeling, and the formation of specialized structures like podosomes. Through these signaling pathways cells can detect extracellular cues to manage essential functions like movement, secretion and phagocytosis. Ras homolog (Rho) GTPases such as Rho, Rac, and cell division control protein 42 homolog (CDC42) represent one of these regulatory systems. These molecules direct actin dynamics by managing polymerization and influencing cell behaviors like movement and adhesion. However, actin regulation is highly complex and involves numerous additional interactors, including kinases, adaptors, and scaffolding proteins. Knockout mouse studies have provided critical insights into the roles of Rho GTPases during development and disease, highlighting their central function within this broader regulatory network (Heasman and Ridley, 2008).

Actin operates through extensive interactions with other cytoskeletal components including microtubules and intermediate filaments instead of functioning in an insolated form. Cellular processes like migration, adhesion and division are based on the concerted operation formed by these interactions (Pradeau-Phélut and Etienne-Manneville, 2024). Actin filaments create a contractile ring during cytokinesis which helps separate daughter cells throughout during cell division (Pelham and Chang, 2002). Actin filaments enable short-range vesicle movement by transporting intracellular components such as Golgi vesicles and melanosomes through myosin motor interactions (DePina and Langford, 1999). The leading edge of cells generates the force needed for cell motility through actin polymerization while myosin motors further enhance this movement and traction process.

The regulation of actin involves strict control through numerous regulatory proteins and signaling pathways which include Rho GTPases as well as kinases and phosphatases. The regulatory systems allow actin to dynamically adjust its structure to meet cellular needs while playing crucial roles in maintaining cell shape, enabling movement through podosome-mediated matrix degradation and executing vital functions like phagocytosis and cytokinesis. These dynamic properties underscore actin's central role in cellular organization and function.

1.4 Podosomes

The discovery of podosomes occurred in 1982 when F-actin-rich micron-scale dot-like structures were identified at cell-substratum interfaces within osteoclasts and monocytes (Lehto et al., 1982), while similar cytoskeletal modifications were reported in Rous sarcoma virus-transformed cells in 1980 (David-Pfeuty and Singer, 1980). The term "podosomes" was

introduced in 1985 (Tarone et al., 1985) to describe structures which subsequent research confirmed could adhere to and degrade ECM components (Mizutani and et al., 2002). In 1989 Src-enriched degradation sites in cancer cells were identified and the term "invadopodia" was coined (Chen, 1989). They are considered the pathological counterpart to podosomes. The invadosome family includes both structures (Murphy and Courtneidge, 2011) yet podosomes remain dynamic and transient compared to invadopodia which create stable ECM-degrading protrusions (Baldassarre et al., 2003).

Podosomes naturally occur in immune cells including macrophages (Linder et al., 1999), dendritic cells (Burns et al., 2001), microglia (Vincent et al., 2012), and osteoclasts where they form belts that drive bone resorption (Zambonin-Zallone et al., 1988; Destaing et al., 2003; Miyauchi and et al., 1990). They also exist in other cell types such as smooth muscle cells (Gimona et al., 2003; Burgstaller and Gimona, 2005), endothelial cells (Moreau et al., 2003), megakaryocytes (Schachtner and et al., 2013), and eosinophils (Johansson and et al., 2004). Podosome dysregulation appears in diseases like Wiskott-Aldrich syndrome (WAS) and chronic myeloid leukemia (CML) WAS-patient macrophages, where macrophages cannot properly form podosomes (Linder et al., 1999), as well as in dendritic cells of CML patients (Dong et al., 2003). The adaptor protein Tks5 enhances invadopodia formation in cancer cells which leads to invasive its behavior (Seals et al., 2005) and invadopodia-associated proteins are essential for tumor aggression and metastasis as demonstrated by in vivo studies (Blouw et al., 2008; Weaver, 2008).

1.4.1 Functions

Podosomes serve as multifunctional hubs that integrate cell adhesion, ECM degradation, and mechanosensing. These primary functions are enabled by their unique architecture and molecular composition.

Adhesion is mediated through integrins, particularly β1, β2, and β3 subtypes (Gaidano et al., 1990) and CD44 (Chabadel et al., 2007), localized beneath the core. These adhesion molecules anchor the cell to the ECM, stabilizing cell-substrate contacts even in dynamic environments. For ECM degradation, podosomes localize matrix metalloproteinases (MMPs) such as membrane type 1-matrix metalloproteinase (MT1-MMP) to the ventral side of their core, allowing targeted proteolysis of ECM components. This was first demonstrated in macrophages (Wiesner et al., 2010), and MT1-MMP localization to podosomes plays a central role in enabling cell invasion, particularly in pathological contexts such as cancer (Nakahara and et al., 1997). Podosomes also function as mechanosensors, probing the stiffness and topographical features of the ECM. Through actomyosin-generated forces, they sense changes in substrate rigidity and help guide cellular migration strategies accordingly (Labernadie et al., 2014). In certain contexts, podosomes participate in more specialized processes. In osteoclasts, podosomes organize into ring-shaped sealing zones that enclose the resorption lacuna, a compartment into which protons and lytic enzymes are secreted for bone matrix degradation (Miyauchi and et al., 1990). Though podosomes are not the agents of resorption themselves, their role in spatial organization is essential to osteoclast function. During angiogenic sprouting, en-
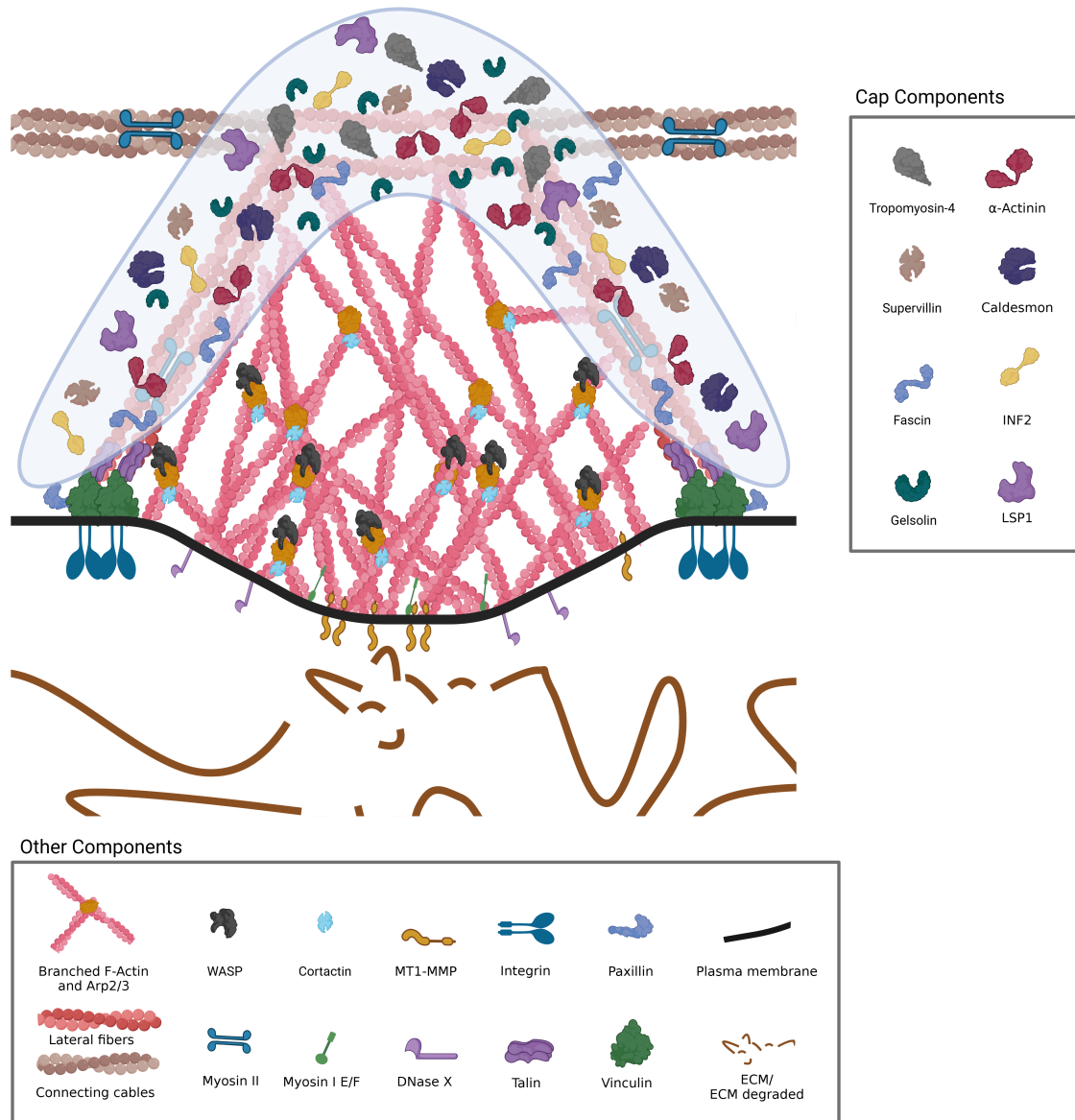
Figure 1.2: **Structural model of a podosome emphasizing cap-regulatory proteins.** The podosome (typical diameter ∼1 µm, though variable) exhibits three interconnected domains: (i) a branched **F-actin core** nucleated by Arp2/3-WASP complexes, (ii) a peripheral **adhesive ring** containing integrins, talin, and vinculin, and (iii) the apical **cap structure** that coordinates mechanochemical regulation. **Cap components** include: **Tropomyosin-4** (structural boundary), **INF2** (linear actin polymerization), **caldesmon** (stabilization), **supervillin-myosin IIA** (contractility-driven disassembly), **zyxin** (actin repair), and **fascin** (actin bundling). The cap orchestrates the transition from branched core actin to linear filaments while integrating mechanical cues from the adhesive ring and extracellular matrix.

dothelial cells form VEGF/Notch-induced podosomes that degrade basement membrane collagen-IV, enabling vessel outgrowth (Spuul et al., 2016). In the neuromuscular junction, podosomes contribute to remodeling by regulating acetylcholine receptor clustering (Proszynski et al., 2009). Another context-specific role occurs during osteoclastogenesis, where actin-rich, zipper-like structures sharing podosome components such as ARP2/3 and Tks5 drive cell-cell fusion (Oikawa et al., 2012). While not a canonical function, this suggests podosome-related architectures may participate in multicellular organization. Macrophages in three-dimensional (3D) environments have been shown to form "3D po-

dosomes", large (roughly 5 µm) actin-rich structures that retain degradative capacity by localizing ECM-lytic enzymes (van Goethem et al., 2010). These structures highlight the functional adaptability of podosomes beyond 2D culture systems (Gawden-Bone et al., 2010).

1.4.2 Structure & Regulation

Podosomes have an F-actin-rich core together with an adhesive ring and an apical cap structure. As described in the actin section, the Arp2/3 complex is a key regulator of branched actin network formation. While its precise role in podosome core generation remains to be fully defined, actin polymerization in this structure is thought to follow similar principles. This process relies on intact and sufficient Wiskott-Aldrich syndrome protein (WASP), which plays a crucial role in precisely recruiting and activating the Arp2/3 complex at specific cellular sites (Linder et al., 2000a). Additionally, the core includes actin-associated proteins cortactin (Tehrani et al., 2006) and Tks5 (Oikawa et al., 2008). Plaque proteins such as paxillin (Spinardi et al., 2004), talin (Zambonin-Zallone et al., 1989), and vinculin (Gaidano et al., 1990) associate with the surrounding adhesive ring to facilitate ECM binding through integrins (Gaidano et al., 1990; Zambonin-Zallone et al., 1989). The cap functions as a regulatory interface that connects core dynamics with extracellular force transmission, as evidenced by the localization of tropomyosin-4 at the podosome apex (McMichael et al., 2006). The cap is the most recent addition elevating podosomes from a previously bipartite to a tripartite cellular substructure.

Two distinct sets of unbranched actin filaments govern podosome architecture: The core connects to the adhesive ring via lateral filaments while dorsal actin cables establish interconnected podosome arrays through crosslinking by myosin IIA (van den Dries et al., 2019). Mid-range connectivity enables cells to probe basement membranes over extended distances to identify suitable sites for protrusions (Proag et al., 2015). Podosome assembly preferentially occurs in areas of low contractility, where Ras homolog family member A (RhoA) regulators such as p190 Rho GTPase-activating protein (p190RhoGAP) inactivate RhoA, thereby facilitating actin remodeling (Arthur and Burridge, 2001; Burgstaller and Gimona, 2004). This process requires intact microtubules (Linder et al., 2000b) alongside reactive oxygen species generated by nicotinamide adenine dinucleotide phosphate (NADPH) oxidase through NADPH oxidase 4 (Nox4) and Tks5 (Diaz et al., 2009). The CDC42 protein regulates core formation by activating WASP to trigger the Arp2/3 complex-dependent nucleation of branched actin networks (Linder et al., 1999, 2000a) and activating inverted formin 2 (INF2) (Kühn and Geyer, 2014) for the production of unbranched lateral actin filaments as part of the podosome cap (Panzer et al., 2016).

Podosomes exhibit a median lifespan of approximately 3 minutes in clusters (Destaing et al., 2003). In primary human macrophages, lifespans of 9.9 minutes have been observed (Cervero et al., 2018), while in IC-21 macrophages, Evans et al. (2003) identified two distinct podosome populations: "simple podosomes", which assemble and disassemble within 1 minute, and "branched podosomes", which persist for up to 7 minutes, often forming through fission from older structures. This study also introduced the concept of

"precursor podosomes" and described the podosome cluster precursor (PCP) which is a larger adhesion structure that can generate multiple new podosomes, particularly at the leading edge.

Podosomes are characterized by rapid actin turnover, as demonstrated by fluorescence recovery after photobleaching (FRAP), with an actin half-life of approximately 20 seconds (Evans et al., 2003).

The stiffness of podosomes changes in response to actin bundling and myosin contractility cycles (Labernadie et al., 2014). While their shape and width remain unchanged the podosome lifespan and spacing vary across different substrate rigidities (Collin et al., 2006). Mature podosomes generate myosin-independent tension through a transmission system linking core protrusion and ring adhesion (van den Dries et al., 2019) while depending on microtubule-driven transport systems for delivering proteolytic enzymes such as MMPs (Wiesner et al., 2010) and deoxyribonuclease-1-like 1 (DNaseX) (Pal et al., 2021) to degrade the extracellular matrix or extracellular DNA. Hyper-contractile microenvironments trigger disassembly (Rafiq et al., 2019) through supervillin-mediated myosin IIA activation (Bhuwania et al., 2012), Rho kinase-dependent contractility (van Helden et al., 2008), and calpain-mediated cleavage of talin, protein tyrosine kinase 2 beta (Pyk2), and WASP (Calle et al., 2006).

1.4.3 Cap Structure

The podosome cap combines multiple components that control both the activity and mechanical response of podosomes. The first mention of the cap emerged from studies showing tropomyosin-4 localizes at the top of podosomes (McMichael et al., 2006). The podosome formation and stability are believed to depend on proteins such as caldesmon which is hypothesized to stabilizes podosomes (Gu et al., 2007), gelsolin which is suggested to regulates podosome dynamics by capping and cleaving actin filaments, enabling protrusion and preventing rapid disassembly (Gawden-Bone et al., 2010), supervillin which likely recruits myosin IIA to initiate disassembly (Bhuwania et al., 2012), and INF2 which may be involved in forming de novo podosomes (Panzer et al., 2016). Fascin promotes podosome disassembly by shifting actin organization from a branched network to tightly bundled filaments (Van Audenhove et al., 2015), while lymphocyte-specific protein 1 (LSP1) and INF2 are thought to control podosome oscillation (Cervero et al., 2018; Panzer et al., 2016). Zyxin seems to regulates actin repair at the podosome cap, while α-actinin crosslinks linear actin filaments in the core periphery (Joosten et al., 2018; van den Dries et al., 2019). Podosome size is regulated by caldesmon (Gu et al., 2007), fascin (Van Audenhove et al., 2015), formin INF2 (Panzer et al., 2016), and tropomyosin-4 (McMichael et al., 2006), while cap components collectively regulate actomyosin contractility and mechanosensitivity (Bhuwania et al., 2012; Cervero et al., 2018). The cap appears to facilitate the transformation of branched core actin into linear actin filaments (Linder and Cervero, 2020) which provides precise regulation of protrusive force production and extracellular matrix remodeling.

1.5   Microtubules

Microtubules (MTs) support cellular structure and enable intracellular transport while also assisting in cell division. Microtubules are hollow polymers structured as tubes that consist of α/β-tubulin heterodimer pairs and form their 23-25 nm diameter through the lateral association of 13 protofilaments (Carlson, 2019). Protofilaments in microtubules are usually constructed from α- and β-tubulin subunits which are organized head-to-tail to providing intrinsic polarity within the structure (Lodish et al., 2007). The most common arrangement follows a 13-3 architecture, where 13 tubulin dimers form one turn of the helix. However, alternative protofilament architectures, such as 11-3, 12-3, 14-3, 15-4, or 16-4, have also been observed, albeit less frequently (Sui and Downing, 2010). The microtubule end exposed to β-tubulin (+) grows more rapidly than the α-tubulin capped end (-)which remains stable and typically anchored at the microtubule-organizing center (MTOC) (Nogales and Wang, 2006; Wu and Akhmanova, 2017). The intrinsic polarity of these structures directs motor proteins like kinesins and dyneins during transport operations by determining their movement paths towards designated cellular targets (Yildiz, 2021).

A defining property of microtubules is their dynamic instability (Mitchison and Kirschner, 1984) identified as a stochastical switch between polymerization and rapid depolymerization. The growth stability of microtubules depends on a guanine triphosphate (GTP) cap presence at the plus end. When the GTP cap at the microtubule's plus end disappears microtubules undergo a conformational change that starts their rapid disassembly, known as catastrophe (Caplow and Shanks, 1996; van Haren and Wittmann, 2019). Microtubules regain their growth capacity through rescue events which are precisely regulated by microtubule-associated proteins (MAPs) and other regulatory factors including post-translational modifications (PTMs) (Lawrence et al., 2023).

Microtubules perform essential cellular functions that include intracellular trafficking and organelle positioning alongside their structural roles and mitotic spindle formation (Quezada et al., 2022). Microtubule functional diversity results partially from tubulin isoform variations because humans produce at least nine different isoforms of both α- and β-tubulin which contribute to a specialized "tubulin code" that affects microtubule properties (Roll-Mecak, 2020). The specialized tubulin isoform γ-tubulin forms the γ-tubulin ring complex (γ-TuRC) at MTOCs which functions as a template for microtubule polymerization while initiating microtubule assembly (Kollman et al., 2010).

1.5.1   Regulation of Microtubules

Microtubule behavior is tigthly regulated by multiple factors which include MAPs, PTMs and motor proteins. These control systems maintain microtubule function through regulated dynamics while ensuring their stability and interaction with other cellular components.

MAPs function as primary regulators of microtubule behavior. MAP2, MAP4 and tau maintain microtubule structural integrity by promoting polymerization while preventing

disassembly (Nishida et al., 2023). Stathmin acts as a destabilizing protein that disrupts microtubule assembly by binding tubulin dimers or causing microtubule depolymerization (Lu et al., 2014). Proteins that sever microtubules like katanin manage microtubule turnover through fragmentation which enables microtubule reorganization and breakdown (McNally and Vale, 1993). Other MAPs, such as capping and motor proteins, further modulate microtubule behavior (Akhmanova and Steinmetz, 2010; Yildiz, 2021).

PTMs of tubulin play a role in microtubule regulation through stability changes and altered MAP and motor protein interactions. The only known PTM within the microtubule lumen occurs at lysine-40 of α-tubulin where acetylation increases microtubule stability and improves motor protein transport efficiency (Soppina et al., 2012). The removal of the terminal tyrosine from α-tubulin through detyrosination results in an increased landing rate for kinesin-1 which affects intracellular transport mechanisms (Kaul et al., 2014). Polyglutamylation and polyglycylation differ in their addition of glutamate or glycine chains to tubulin which regulates microtubule stability and enzymatic access and serves as crucial mechanisms in both neuronal function and ciliary motion (Garnham et al., 2015; Wloga et al., 2009). The combination of these modifications establishes the tubulin code which operates as a complex system that controls microtubule activity across various cellular environments (Roll-Mecak, 2020).

The function of microtubules is additionally controlled by motor proteins such as kinesins and dyneins. Kinesins transport cellular proteins and organelles as they move toward the plus end of microtubules (Gennerich and Vale, 2009). Dyneins transport cellular cargo to the minus end of microtubules and are essential for both mitotic spindle positioning and retrograde neuron transport (Yildiz, 2021). MAPs and PTMs work together with motor proteins to enable efficient cargo transport inside cells and proper cytoskeletal structure.

1.5.2 Microtubule plus-end tracking proteins (+TIPs)

Microtubule plus-end tracking proteins (+TIPs) represent a specialized subset of MAPs that bind selectively to growing microtubule ends and regulate their dynamics (Akhmanova and Steinmetz, 2010). These proteins regulate both the polymerization and stabilization of microtubules while managing their interactions with different cellular structures.

The end-binding (EB) proteins EB1, EB2, and EB3 represent some of the better-studied microtubule plus-end tracking proteins in mammalian cells (van de Willige et al., 2016). EB proteins function as primary regulators of microtubule plus-end dynamics through tip stabilization and catastrophe suppression while their polymerization impact changes with different cellular contexts (Komarova et al., 2009). EB1 and EB3 have been shown to drive microtubule elongation and support neurite extension (Geraldo et al., 2008; Stepanova et al., 2010), while EB2 functions oppositely by destabilizing microtubules through competition with EB1 for binding sites (Arens et al., 2013).

The cytoplasmic linker protein-170 (CLIP-170) functions as an essential +TIP that supports microtubule rescue and polymerization. CLIP-170 functions as a central site for dynein interaction to guide cargo to the microtubule plus-end for movement (Henrie et al.,

2020; Vaughan et al., 1999). Cytoplasmic linker-associated proteins (CLASPs) work to stabilize microtubules while facilitating rescue events that enable microtubule growth to meet cellular demands (Lawrence and Zanic, 2019).

The structural domains of +TIPs primarily determine their ability to track microtubule ends because domains like the calponin homology (CH) domain found in EB proteins allow them to recognize and attach to the unique structures at growing microtubule tips (Gimona et al., 2002). Fluorescence microscopy reveals that +TIPs form comet-like structures at the microtubule plus end demonstrating their function in following polymerizing microtubules (Mimori-Kiyosue et al., 2000).

A broad range of cellular activities such as cell polarization, migration, and intracellular transport rely on the functional contributions of +TIPs (Bouchet and Akhmanova, 2017). The function of +TIPs to connect microtubules with the cell cortex, organelles and signaling complexes establishes their crucial role in managing cytoskeletal dynamics and cellular organization (Lansbergen et al., 2006; Lomakin et al., 2009).

1.6   Endocytosis

Endocytosis serves as a crucial cellular mechanism where plasma membrane-derived vesicles transport external materials like nutrients, signaling molecules, or pathogens into the cell. This mechanism plays a vital role in cellular homeostasis, facilitating both nutrient absorption and dynamic interactions with the extracellular environment through surface-exposed molecules (Doherty and McMahon, 2009). Far from being a mere passive uptake system, endocytosis operates by influencing plasma membrane composition and receptor regulation which by extension adjusts vital cellular signaling pathways essential for growth and immune responses as well as the overall operation of cells (Antonescu et al., 2014). Christian de Duve established the term "endocytosis" in 1963 while building upon Elie Metchnikoff's early research on phagocytosis that led to his Nobel Prize in 1908 (Pathak et al., 2023). Research has shown that this mechanism has preserved its functionality throughout eukaryotic evolution while playing essential roles in defense mechanisms and metabolic processes.

The process of endocytosis includes multiple separate pathways which are specialized for different cargo types and cellular requirements. The process of phagocytosis which is commonly known as "cell eating" captures large particles like bacteria or apoptotic cells that measure more than 0.5 micrometers in size. Actin-driven membrane extensions form the basis of this pathway which serves critical functions in immune defense and tissue clearance (Caron and Hall, 1998; May et al., 2000). Through the process known as pinocytosis or "cell drinking," cells absorb extracellular fluid together with minute dissolved solutes as a non-specific method for nutrient uptake (Amyere et al., 2000; West et al., 2000). Receptor-mediated endocytosis on the other hand functions as a more selective cellular process that allows internalization of specific molecules like hormones and growth factors via plasma membrane receptors (Sorkin, 2004). Clathrin-mediated endocytosis (CME) stands out as a thoroughly studied cellular uptake mechanism that utilizes a clathrin protein coat to form a lattice structure which surrounds invaginating membrane
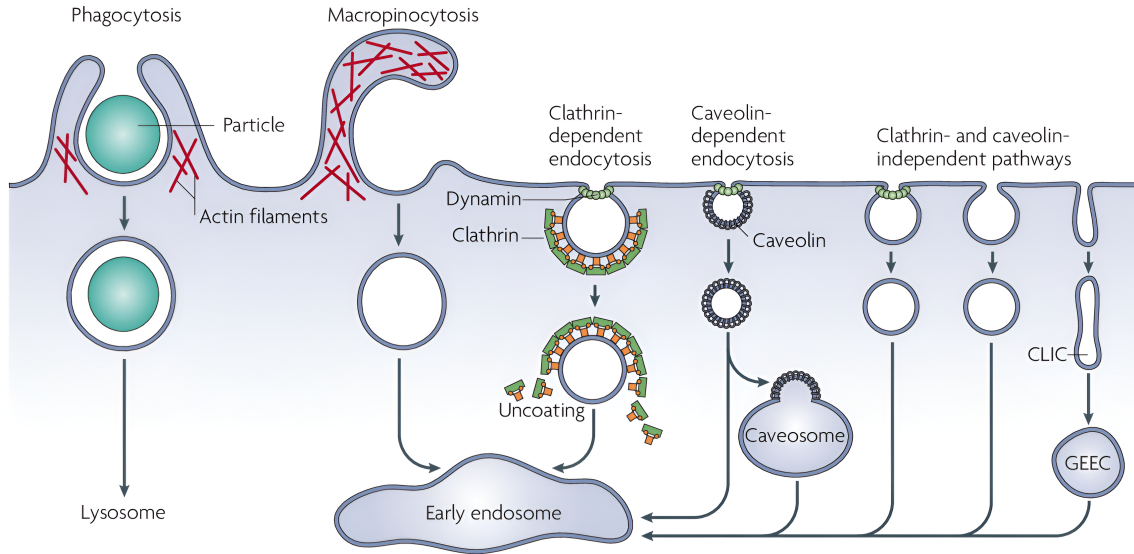
Figure 1.3: **Diversity of Endocytic Mechanisms in Eukaryotic Cells.** Cellular internalization occurs through several distinct pathways: phagocytosis for large particles, macropinocytosis for fluid-phase uptake, clathrin-mediated endocytosis (CME), caveolin-dependent uptake, and clathrin- and caveolin-independent routes (including CLIC/GEEC). These mechanisms differ in their initiation signals, vesicle size, molecular machinery, and intracellular trafficking routes. **Clathrin-mediated endocytosis** proceeds through sequential stages: (1) receptor-ligand binding initiates curvature generation, (2) adaptor proteins (e.g., AP2) recruit clathrin triskelia to form a coated pit, (3) dynamin-mediated membrane scission releases the vesicle, and (4) uncoating exposes vesicle fusion machinery. This tightly coordinated process enables selective uptake while maintaining membrane composition through compensatory recycling. Reproduced from Mayor et al. (2014).

pits and helps concentrate and internalize necessary materials (Ford et al., 2002).

The functional process of CME functions through a highly orchestrated sequence of events which involve more than 50 proteins and has been thoroughly researched over many years (Kaksonen and Roux, 2018). The initiation stage of the process occurs when pioneer proteins such as FCHo label designated areas on the plasma membrane to start pit formation (Henne et al., 2010). The AP2 complex mediates cargo selection and coat assembly by binding cargo and lipids while it recruits clathrin to form a coat through polymerization (Kelly et al., 2014). The membrane undergoes invagination during pit deepening due to the combined effects of clathrin assembly together with actin dynamics and curvature-inducing proteins such as epsin (Ford et al., 2002). Dynamin and BAR domain proteins facilitate the membrane scission step which pinches off vesicles from the plasma membrane by constricting and severing the membrane neck (Daumke et al., 2014). The final step of uncoating occurs when auxilin and ATP-dependent Hsc70 work in tandem to break down the clathrin coat which releases the vesicle as an endosome to engage in intracellular trafficking (Massol et al., 2006). Throughout the process phosphoinositides including phosphatidylinositol-(4,5)-bisphosphate maintain crucial regulatory control over pit initiation and stabilization which helps determine vesicle size resulting in precise and efficient endocytosis (Antonescu et al., 2011).

Endocytosis extends its functions beyond material uptake by playing a crucial role in modifying cellular signaling pathways. Although receptor internalization is primarily associated with material uptake, it also functions as a de facto regulatory switch by modu-

lating signaling pathways. After internalization certain receptors maintain their signaling capabilities inside endosomes which introduces additional spatial and temporal factors to signaling pathways. The ability of endocytosis to both uptake materials and regulate signaling highlights its intricate nature that goes beyond the basic function of transport (Sigismund et al., 2012). The implications of these mechanisms extend to health and disease, as disruptions in endocytosis are linked to conditions like cancer, where altered receptor trafficking can drive uncontrolled growth, and viral infections, where pathogens exploit endocytic pathways for entry (Mercer et al., 2010), notably this includes severe acute respiratory syndrome coronavirus via ACE2 (Inoue et al., 2007; Bayati et al., 2021). Moreover, its integration with cellular structures like microtubules, which guide vesicle transport, hints at broader coordination with processes such as immune cell motility and function.

The variety of endocytic pathways demonstrate their unique functional roles through distinct mechanisms. The actin-dependent machinery enables phagocytosis to capture large particles without the involvement of clathrin while membrane ruffling drives pinocytosis for bulk fluid uptake (West et al., 2000). CME, with its reliance on clathrin and dynamin (Praefcke and McMahon, 2004), excels at specific, receptor-driven internalization, contrasting with caveolin-mediated endocytosis, which uses lipid raft-derived caveolae (Parton and Simons, 2007), and various clathrin-independent pathways like flotillin-dependent uptake (Glebov et al., 2006). The specific molecular requirements and cargo selectivity of different endocytic pathways demonstrate how endocytosis as a whole adjusts to meet cellular needs. The complex system functions through mechanisms like CME to maintain cellular life while establishing a basis for studying its interactions with other cellular elements like microtubules during immune reactions or disease conditions for future research exploration.

1.7   Computational Tools in Bioimage Analysis

The development of computational tools for bioimage analysis has advanced in parallel with programming languages with each playing a historical role in advancing the field of biology and continuing to hold different levels of relevance today. MATLAB (available at `https://www.mathworks.com/`) secured its place as a essential tool in both academic and industrial research because of its Image Processing Toolbox which appeared in the 1990s and made matrix-based image manipulation more straightforward. MATLAB became the go-to option for developing algorithms in microscopy and medical imaging because its optimized matrix computations and visualization capabilities provided great value in settings where licensing fees were a non-issue. Similarly, Java (available at `https://www.oracle.com/`) earned widespread recognition because ImageJ, which is an open-source system released in 1997 to analyze microscopy images, established itself as a critical platform in this research field. The plugin architecture of ImageJ which utilizes Java's cross-platform abilities and effective memory management led to extensive use in biological research and developed into Fiji Is Just ImageJ (Fiji) with improved scripting and library support. R (available at `https://cran.r-project.org/`) serves as a statistical

language but gained specialized use in bioimage analysis through packages like EBImage which helped merge imaging data with genomics and transcriptomics statistical workflows. Even Ruby (available at `https://www.ruby-lang.org/`) maintained a presence in small-scale projects by utilizing OpenCV bindings and because of its readable syntax that supports rapid scripting.

Python (available at `https://www.python.org/downloads/`) became a central language by leveraging the advantages of its predecessors. The open-source ecosystem of Python developed by incorporating MATLAB-like matrix operations through NumPy, with ImageJ's microscopy-processing tools from PyImageJ and R's statistical methodologies from SciPy and improved scalability and interoperability performance. Industrial-grade image processing libraries such as OpenCV and scikit-image enabled advanced tool usage and TensorFlow and PyTorch frameworks brought machine learning (ML) capabilities to bioimaging workflows leading to a significant shift in the field because artificial intelligence (AI)-driven analysis are becoming increasingly central. Python's flexible nature enables interfacing with older software systems like ImageJ plugins through Java bridges and enabled workflow advancements through automation, graphics processing unit (GPU) acceleration and cloud computing capabilities. Python's widespread community support and extensive documentation combined with its capabilities for reproducible research (e.g., Jupyter or Google Colab Notebooks) have established it as the most adaptable programming language for current bioimage analysis challenges while Java remains dominant in ImageJ/Fiji systems and MATLAB persists in academic legacy workflows.

Table 1.1: Strengths and limitations of programming languages for biological image analysis.

Language	Strengths	Limitations
Python	- Extensive libraries: OpenCV, scikit-image, PyTorch, TensorFlow. - Deep learning integration (AlphaFold (Jumper et al., 2021)). - Interoperability (ImageJ, MATLAB). - Reproducible workflows (Jupyter).	- Slower than C/C++/Java. - Memory-intensive for large datasets.
MATLAB	- Specialized toolboxes (Image Processing, Deep Learning). - Optimized matrix computation.	- Expensive licensing. - Limited scalability and ML support.
Java	- ImageJ/Fiji backbone. - High performance.	- Complex syntax. - No native ML frameworks.
R	- Statistical analysis (Bioconductor). - Bioimaging packages (EBImage).	- Poor scalability for large images. - No GPU/ML integration.
Ruby	- Scripting simplicity. - BioRuby legacy.	- Minimal adoption in imaging. - No ML libraries.

MATLAB continues to play a significant role in algorithm development for particular specialized areas like educational applications and proprietary medical imaging technologies because its ready-to-use toolboxes simplify and speed up development tasks. The proprietary nature of MATLAB and the licensing expenses conflict with the open collaboration ethos essential to current bioinformatics. Despite Java's importance in sustaining ImageJ/Fiji which serves as a core tool in microscopy research the platform struggles with AI integration because it lacks a comprehensive deep learning framework alongside

its verbose coding structure which impedes fast prototyping. R remains indispensable for datasets that demand strict statistical analysis like spatial transcriptomics and high-content screening yet its computational inefficiency prevents its use for large-scale image processing. Ruby demonstrates the historical function of specialized languages that provided scripting flexibility before Python became the dominant language.

A comparison between Python and ImageJ reveals their unique advantages and disadvantages. The Java-based ImageJ tool depends on graphical user interface (GUI) macros that restrict automation capabilities while Python allows complete scripting of data processing workflows. ImageJ performs well in basic image processing and domain-specific extensions yet doesn't support Python's advanced AI/ML integration capabilities found in PyTorch and TensorFlow. Python showcases strong reproducibility capabilities through script version control using Git or Jupyter Notebooks while ImageJ macros are dependent on GUI versions which makes replication more difficult. Java's complexity creates scripting limitations for ImageJ while PyImageJ allows users to access its functionality through Python offering simpler coding solutions. ImageJ encounters scalability issues due to its single-threaded design when working with large datasets but Python handles large datasets better because it supports parallel computing and GPU acceleration. ImageJ proves effective for visualization and GUI-based tasks when used in conjunction with Python.

These languages demonstrate how technology trends are moving in favor of open-source programming solutions which are both modular and scalable. Python's popularity demonstrates the field's need to integrate several domains by merging image processing with ML, statistical analysis, and high-performance computing. Legacy software such as ImageJ remains essential for tasks like interactive visualization and specialized microscopy plugins yet Python has accelerated bioimage analysis by creating unified workflows through tools such as Napari and CellProfiler. Python has enabled wider access to artificial intelligence through frameworks like PyTorch and TensorFlow which has led to faster adoption of deep learning applications in segmentation. Python's ecosystem matches the field's desire for reproducibility, scalability, and cross-disciplinary collaboration by learning from other languages and continuously innovating through community contribution to overcome limitations.

1.7.1 Python in Bioinformatics and Computational Biology

Python's adaptability establishes it as a fundamental tool in bioinformatics and computational biology which enables breakthroughs in fields ranging from molecular modeling to high-throughput imaging analysis. One notable application is Alias4SBML (Heydarabadipour and Sauro, 2025), which addresses a perennial challenge in systems biology: visualizing highly connected molecular networks. Alias4SBML creates duplicate nodes (aliases) for highly connected molecules in Systems Biology Markup Language (SBML) models to decrease visual clutter while maintaining network topology thus improving the understanding of metabolic pathways and signaling cascades. QuantumDNA (Herb et al., 2025) uses Python's scientific libraries to model DNA charge transfer through quantum-

physical approaches including linear combination of atomic orbitals (LCAO) and tight-binding models for biophysical research. The program combines open quantum systems theory with a GUI interface to facilitate cross-disciplinary research between biophysics and computational chemistry.

Python-powered denoising diffusion probabilistic models (DDPMs) (Bachimanchi and Volpe, 2025) have added to the field of image restoration within microscopy. The PyTorch-based models execute an iterative denoising process on low-resolution images to approach theoretical resolution limits essential for biological imaging studies of subcellular structures and dynamic processes like vesicle trafficking. AlphaFold (Jumper et al., 2021) stands out as a structural biology milestone that showcases Python's ability to manage complex scientific tasks. Performance-critical components employ JAX to accelerate GPU/tensor processing unit (TPU) operations through accelerated linear algebra (XLA) while its Python-centric architecture allows seamless integration of TensorFlow and NumPy for data handling. AlphaFold 3 (Abramson et al., 2024) recently expanded its framework to predict biomolecular interactions with proteins through diffusion-based deep learning for non-commercial research access.

Python proves powerful in bioimage analysis because of its ability to operate with multiple technologies. The combination of traditional image processing libraries OpenCV and scikit-image with deep learning frameworks PyTorch and TensorFlow supports workflows from basic pixel filtering to advanced phenotype classification through AI. The library PyImageJ enables interoperability between legacy tools and modern Python scripts by embedding ImageJ/Fiji functions which lets users integrate Java plugins with Python scalability features. The use of Compute Unified Device Architecture (CUDA)-enabled GPU acceleration with PyTorch/TensorFlow combined with distributed computing frameworks such as Dask and Ray solves performance issues when processing extensive datasets. Jupyter and Google Colab Notebooks act as standard tools to enforce reproducibility throughout team-based research projects. Python merges scripting capabilities with high-performance computation to dissolve traditional barriers and enable faster conversion of theoretical models into biological applications.

1.7.2 Past Approaches to Podosome Analysis

The initial podosome analysis techniques depended on manual or semi-automated processes because they were limited by the available technology and computing power of their era. The primary analyses by Bhuwania et al. (2012) and Kopp et al. (2006) utilize ImageJ for manual thresholding to measure podosome density and lifetime together with tracking dynamic events like fission and microtubule interactions through manual examination of 2D time-lapse datasets. The foundational nature of these methods was undermined by their use of 2D projections and time-consuming procedures which hindered understanding of 3D podosome structures and processing of extensive datasets.

The development of semi-automated tools offered partial solutions to these challenges. Meddens et al. (2013) introduced a 2D detection algorithm for fluorescence microscopy images which uses local/global thresholding along with size/shape filtering and watershed

segmentation but does not incorporate 3D analysis or ML integration. While Cervero et al. (2013) used ImageJ macros to perform thresholding and watershed segmentation they require manual adjustments to parameters like gamma correction and convolution kernels which made their procedures resemble an expert-dependent "recipes" instead of a standardized tools. Berginski et al. (2014) enhanced invadopodia detection via dual-channel fluorescence imaging and region-growing algorithms yet neglected molecular composition on single-podosome level. Proag et al. (2016) combined fluorescence microscopy with atomic force microscopy (AFM) to analyze podosome mechanics while depending on manual parameter validation. Joosten et al. (2018) used super-resolution correlative light and electron microscopy (SR-CLEM) to achieve 3D ultrastructural resolution but lacks volumetric reconstruction and automated population-wide quantification. The tool "Poji" (Herzog et al., 2020) automated F-actin maxima detection in Fiji/ImageJ but still needed user-defined thresholds and expert validation which highlights ongoing challenges in full automation.

Table 1.2: **Podosome Detection Tools and Methods.** This table summarizes historical approaches for podosome detection, including manual, semi-automated, and computational workflows. Global limitations across studies include 2D-focused analysis, dependency on GUI-based tools (e.g., ImageJ macros), and absence of machine learning integration.

Tool (Year)	Method	Automation Level	Key Limitations
Bhuwania et al. (2012)	Manual ImageJ thresholding	Manual	- Labor-intensive. - 2D-only analysis. - Observer bias.
Kopp et al. (2006)	Manual tracking of dynamics	Manual	- 2D projections. - No scalability.
Meddens et al. (2013)	MATLAB/DIPimage thresholding + watershed	Semi-Automated	- 2D-only. - No ML. - Manual parameter tuning.
Cervero et al. (2013)	ImageJ macros + manual adjustments	Semi-Automated	- GUI-dependent. - Expert validation required.
Berginski et al. (2014)	MATLAB/Perl invadopodia tracking	Semi-Automated	- No molecular analysis. - Static actin markers.
Proag et al. (2016)	ImageJ/AFM mechanics tracking	Semi-Automated	- Focused on mechanics. - No degradation links.
Joosten et al. (2018)	ImageJ/MATLAB SR-CLEM 3D analysis	Semi-Automated	- Complex sample prep. - Specialized equipment.
Herzog et al. (2020)	Fiji/Poji (F-actin maxima)	Semi-Automated	- User-tuned thresholds. - No 3D/ML.

Three key trends characterized these historical approaches. First, software fragmentation dominated workflows: The development of separate MATLAB, ImageJ/Fiji macros, and Perl scripts resulted in isolated processing pipelines. Commercial license costs above $2,350 per year makes MATLAB financially inaccessible for many potential users. Third, technical limitations persist: The available methods only achieved semi-automation and suffer from observer bias due to manual parameter settings and lack AI/ML features for 2D/3D analysis.

The solution to this problem requires the integration of these divided systems into a single framework. A Python tool that uses deep learning methods like CellPose or custom networks can remove manual bias in podosome detection while modular pipelines enable standard analysis of different imaging modalities. The scalability problems which used to cripple large dataset workflows can now be overcome through GPU acceleration and

distributed computing methods. Open-source Python libraries can replace outdated tools to help researchers overcome 2D limitations while automating 3D or even 4D spatiotemporal tracking and enabling open access through community-based development. The proposed transition will address long-standing reproducibility problems while providing fresh biological understanding of podosome heterogeneity on a single and population-wide scope.

1.7.3 Cellpose and Machine Learning for 3D Podosome Detection

The Cellpose framework marks a major progress in bioimage analysis by providing strong support for automated podosome detection. The initial Cellpose algorithm (Stringer et al., 2021) developed a universal segmentation approach that manages various microscopy images without additional training and replaced standard thresholding and watershed techniques through flow-based spatial gradient predictions. The system underwent training with more than 70,000 manually segmented objects to develop adaptive dynamic style vectors that function across variable imaging conditions and an open-source GUI to enable access to ML-based workflows. The Cellpose 2.0 (Pachitariu and Stringer, 2022) and Omnipose (Cutler et al., 2022) iterations of this framework offered tailored model training alongside reduced annotation needs and segmentation capabilities that function regardless of morphology. The upcoming version of Cellpose 3 (Stringer and Pachitariu, 2025) combines image restoration with perceptual loss to improve noisy and undersampled data and meets the demands of live-cell podosome imaging.

Given that podosomes' punctate actin cores resemble nuclei in size and shape, Cellpose's pretrained nuclei model serves as an effective initial detection tool. The method eliminates manual biases found in previous semi-automated techniques like Poji's user-tuned maxima detection (Herzog et al., 2020) and Meddens' watershed-based approach (Meddens et al., 2013) by employing neural networks for automated segmentation. The combination of Cellpose with Python's ML platforms (PyTorch and TensorFlow) allows for scalable large dataset processing and its 2D-to-3D feature will enable volumetric analysis of podosome architecture, which are features not available in previous MATLAB or ImageJ macro-based workflows.

Cellpose implementation for podosome analysis tackles reproducibility problems such as variable thresholding and observer bias through standardized detection methods across different datasets. The implementation of automation reduces the ergonomic dangers from extended manual analysis like carpal tunnel syndrome (Andersen et al., 2003) and makes possible complex measurements such as 4D spatiotemporal tracking that traditional point-and-click methods cannot perform. The ability of ML to reveal subtle patterns like podosome fission and mechanoresponsive behavior leads to more precise results than manual methods that often miss transient or low-contrast details.

The shift towards automated workflows faces obstacles such as overcoming resistance to change while managing computational demands and meeting validation needs. Although manual processes are standard practice they become obsolete when automation decreases analysis duration and minimizes human mistakes while delivering uniform out-

comes across various users and institutions. Although experts used to manual approaches may feel like they are losing control during automated processes transparent pipeline design maintains control because it features steps that are easy to understand and parameters that can be modified. The complex setup phase is justified by long-term benefits since automation removes repetitive manual tasks like thresholding and region of interest (ROI) selection. Cloud-based solutions along with parallel processing frameworks help overcome GPU memory constraints while democratizing access to high-performance computing resources. The model's training data limitations and reliability issues are resolved by employing fine-tuning and transfer learning to specialize generalist models such as Cellpose for podosome applications. The use of open-source tools and file formats such as Open Microscopy Environment TIFF (OME-TIFF) resolves standardization problems which were traditionally caused by isolated workflows like ImageJ macros and MATLAB scripts and enhances reproducibility and cross-lab cooperation. Python provides a free scalable solution that eliminates the cost barriers associated with proprietary software such as MATLAB. Manual ground truth benchmark validation demonstrates that automated outputs deliver higher consistency yet preserve expert adaptability for further refinement.

1.8 Aim of Thesis

This thesis seeks to develop and assess BioPixel, a deep learning-based algorithm tailored for the segmentation and detection of macrophages and podosomes in fluorescence microscopy images. The algorithm employs advanced machine learning methods to automate and refine the quantitative analysis of cellular structures in both 2D and 3D datasets. The work addresses the demand for efficient, reproducible tools in cell biology research by offering an alternative to existing semi-automated techniques. Alongside this, the thesis examines the biological role of drebrin in podosome organization within macrophages, focusing on its domain-specific localization and interactions with EB3 and clathrin. The study explores how drebrin's domains contribute to its positioning and its coordination with the actin cytoskeleton and microtubule network. Additionally, the thesis investigates +TIP heterogeneity, analyzing how proteins such as EB3 and CLIP-170 may define distinct microtubule subsets linked to endocytic and adhesive processes. Through this dual focus, the thesis integrates computational and biological perspectives, using BioPixel as a tool to support these investigations.

2 Materials and consumables

The following section documents general reagents used during this thesis.

2.1 Chemicals, media and reagents

The chemicals or reagents used during this research with details on the manufacturer and catalog number are listed in the Table 2.1 below.

Table 2.1: Chemicals and reagents used in this thesis.

Reagent name	Catalog number	Vendor
2-Propanol	190764	Sigma-Aldrich[1]
Accutase Cell Detachment Solution	A30104	Capricorn Scientific GmbH[2]
Alexa Fluor Plus 405 Phalloidin	A30104	Invitrogen[3]
DPBS	14190144	Gibco[3]
EDTA acid disodium salt dihydrate	ED2SS	Sigma-Aldrich[1]
Fluoromount-G Mounting Medium	00-4958-02	Invitrogen[3]
Kanamycin sulfate	K1637	Sigma-Aldrich[1]
LB Agar (Luria/Miller)	X969	Carl Roth GmbH + Co. KG[4]
LB Broth (Luria/Miller)	X968	Carl Roth GmbH + Co. KG[4]
Methanol	P717	Carl Roth GmbH + Co. KG[4]
Paraformaldehyde	0964	Carl Roth GmbH + Co. KG[4]
Penicillin-Streptomycin	P4333	Sigma Aldrich [1]
Potassium chloride	P017	Carl Roth GmbH + Co. KG[4]
Potassium phosphate monobasic	3904	Carl Roth GmbH + Co. KG[4]
RPMI 1640 Medium	11875093	Gibco [3]
Sodium chloride	9265	Carl Roth GmbH + Co. KG[4]
Sodium phosphate dibasic	T876	Carl Roth GmbH + Co. KG[4]
SYBR Safe DNA Gel Stain	S33102	Invitrogen[3]
TRIS-Acetat	7125	Carl Roth GmbH + Co. KG[4]
Triton X 100	3051	Carl Roth GmbH + Co. KG[4]
UltraPure Agarose	16500-500	Invitrogen[3]

[1] Merck Group, Darmstadt, Germany. [2] Ebsdorfergrund, Germany. [3] Thermo Fisher Scientific, Inc., Waltham, MA, USA. [2] Karlsruhe, Germany.

2.2 Kits

During this project following kits were used (see table 2.2). All products were used according to the manufacturers recommendations.

Table 2.2: Kits used in study.

Product name	Catalog number	Vendor
Duolink In Situ Detection Reagents Red	DUO92008	Sigma Aldrich[1]
Duolink In Situ Wash Buffers, Fluorescence	DUO82049	Sigma Aldrich[1]
Neon Transfection System 10 µL Kit	MPK1025	Invitrogen[2]
QIAquick Gel Extraction Kit	28704	QIAGEN[3]
ZR Plasmid Miniprep - Classic	D4054	Zymo Research[4]

[1] Merck Group, Darmstadt, Germany. [2] Thermo Fisher Scientific, Inc., Waltham, MA, USA. [3] Hilden, Germany. [4] Irvine, CA, USA.

2.3 Antibodies

The following antibodies listed in table 2.3 were used throughout this thesis.

Table 2.3: List of antibodies.

Antibody	Clone	Catalog number	Vendor	RRID
Rabbit α-human Drebrin	polyclonal	PA5-84319	Invitrogen[1]	AB_2791471
Rabbit α-human EB3	monoclonal	ab157217	Abcam[2]	AB_2890656
Mouse α-GFP	monoclonal	MAB3580	Chemicon[3]	AB_2313783
Mouse α-human Clathrin Heavy Chain	X22	MA1-065	Invitrogen[1]	AB_2083179
Mouse α-human β-Tubulin	TUB 2.1	T4026	Sigma-Aldrich[3]	AB_477577
Mouse IgG1 Isotype Control	15H6	5415	Cell Signaling Technology[4]	AB_10829607
Duolink In Situ PLA Probe Anti-Rabbit PLUS	proprietary	DUO92002	Sigma-Aldrich[3]	AB_2810940
Duolink In Situ PLA Probe Anti-Mouse MINUS	proprietary	DUO92004	Sigma-Aldrich[3]	AB_2713942

[1] Thermo Fisher Scientific, Inc., Waltham, MA, USA. [2] Cambridge Biomedical Campus, Cambridge, UK. [3] Merck Group, Darmstadt, Germany. [4] Danvers, MA, USA.

2.4 Oligonucleotides

During this project following primers were used (see Table 2.4). All products were used according to the manufacturers recommendations.

Table 2.4: Primers used in study.

Oligonucleotide Name	Sequence	Vendor
dreb Start phos rev	[PHO]CATGGCGGCCGCTAGCGGATCTGACGGTTCACTAAAC	Eurofins
PP phos fw	[PHO]CCTCCACCACTGCCACCGCC	Eurofins
ΔADFH phos fw	[PHO]GGGCTGGCGCGACTCTCC	Eurofins
ΔPP phos fw	[PHO]GCAGAGGACTTGATGTTCATGGAGTCTGC	Eurofins
ΔPP phos rev	[PHO]CTGCGAGGAGGTGACCTCATCC	Eurofins
dreb end phos fw	[PHO]CCGGTCGCCACCATGGTGAG	Eurofins

2.5 Enzymes

The following enzymes were used during this project (see table 2.5). All enzymes were used according to the manufacturers' recommendations.

Table 2.5: Enzymes used in study.

Enzyme	Catalog number	Vendor
DpnI (10 U/µl)	ER1705	Thermo Scientific[1]
Phusion High-Fidelity DNA Polymerase (2 U/µl)	F530S	Thermo Scientific[1]
T4 DNA Polymerase	M4211	Promega[2]

[1] Thermo Fisher Scientific, Inc., Waltham, MA, USA. [2] Madison, WI, USA.

2.6 Vector Constructs

The following vector constructs were used during this project (see Table 2.6). The construct *wt-drebrin-GFP* was kindly provided by the Division of Cell Biology, German Cancer Research Center, Heidelberg, Germany (Dr. med. Wiebke Peitsch) first generated and used in the publication Peitsch et al. (2005), and served as the template for several downstream constructs.

Table 2.6: Constructs and cloning strategy used in the study.

Construct Name	Template	Primers Used
ΔADFH-GFP	wt-drebrin-GFP	dreb Start phos rev and ΔADFH phos fw
ΔADFH-ΔPP-drebrin-GFP	ΔADFH-GFP	ΔPP phos fw and ΔPP phos rev
CC-Hel-GFP	ΔADFH-GFP	dreb end phos fw and ΔPP phos rev
PP-C-term-GFP	wt-drebrin-GFP	dreb Start phos rev and PP phos fw
C-term-GFP	wt-drebrin-GFP	dreb Start phos rev and ΔPP phos fw

2.7 Laboratory consumables

Standard consumables were used for all experiments during this study.

2.8 Instruments

Fluorescence imaging was performed using the Leica TCS SP8 X system (Leica Microsystems, Wetzlar, Germany). The system was equipped with the Leica DMi8 microscope and operated with Leica LAS X SP8 software. Key specifications for the microscope are summarized in Table 2.7.

For cell transfection, the Neon Transfection System (Thermo Scientific, Waltham, USA) was used following the manufacturer's protocol. The transfection was performed using two pulses of 40 ms at 1000 V.

Table 2.7: Leica TCS SP8 X system specifications.

Component	Specification
Objective	63x HC PL APO Oil CS2 (NA: 1.40, WD: 0.14 mm)
Detectors	3x HyD, 2x PMT, 1x Trans-PMT
Laser Lines	White Light Laser (470-670 nm, pulsed)
Pinhole Size	Variable
Spectral Separation	AOBS + Spectral Detectors
Fluorescence Filters	Filter system (em.-color, dye): excitation — beamsplitter — emission L5 ET (green; AF488, GFP): BP 480/40 — FP 505 — BP 527/30 A (blue; DAPI): BP 340-380 — FP — LP 425 I3 (green; AF488, GFP): BP 450-490 — FP — LP 515 N2.1 (red; AF568, mCherry): BP 515-560 — FP — LP 590
UV Lamp	EL 6000 120W (LQHXP 120 LEJ)
Halogen lamp	100W 12V
Piezo Focus Drive	SuperZ Galvo type H (Travel range: 1500 µm, Reproducibility: 40 nm)
Tandem Scanner	Variable resolution (512×512 @ 7 fps, max. 8192×8192 px, 3600 lines/s)
Optical Table	Actively Damped (Newport)

2.9   Software and Hardware

BioPixel was developed using Python 3.11.9 in Visual Studio Code 1.98.0, with mask labeling performed via Cellpose GUI 1.0.2. The development hardware consisted of an Intel i9-10900K CPU, 32 GB RAM, and an NVIDIA RTX 3080 Ti GPU, leveraging CUDA 12.5 for accelerated computations. Third-party packages integral to its implementation include `OpenCV` for computer vision tasks, `NumPy` for numerical operations, `scikit-image` for feature detection, `Matplotlib` for visualization, `Pillow` for image manipulation, `PyTorch` for deep learning, `Cellpose` for segmentation, and libraries such as `tifffile`, `oiffile`, `readlif`, and `czifile` for handling various microscopy image formats, while the `logging` module supported debugging efforts.

3   Methods

The following chapter covers the methods used in this thesis.

3.1   Cloning of Drebrin Domain Constructs

The target DNA fragment underwent amplification through polymerase chain reaction (PCR), which utilized a 5'-phosphorylated forward primer and a reverse primer, both at a 10 µM concentration. The DNA template was adjusted to 10 ng/µL to prepare a 25 µL reaction volume (see Table 3.1) using a high-fidelity DNA polymerase system. The thermocycling program started with an initial denaturation at 98°C for 1 minute before proceeding with 30 cycles of 98°C denaturation for 30 seconds each, primer annealing at a temperature determined by primer melting temperature (T_m) for 30 seconds, followed by extension at 72°C for 1 minute per kilobase of amplicon length. After the final extension at 72°C for 10 minutes, the samples were stored at 4°C before further processing.

Table 3.1: PCR reagents and thermocycling program.

PCR Reaction Mixture (25 µL)		
Reagent	**Concentration**	**Volume (µL)**
Template DNA	10 ng/µL	1
dNTPs	10 mM	0.5
Forward Primer	10 µM	1.25
Reverse Primer	10 µM	1.25
DNA Polymerase	2 U/µL	0.25
Reaction Buffer	5X	5
H$_2$O	-	15.75
Total		25

Thermocycling Program			
Step	**Temp. (°C)**	**Time**	**Cycles**
Initial Denaturation	98	1 min	1
Denaturation	98	30 s	30
Annealing	60*	30 s	–
Extension	72	7 min**	–
Final Extension	72	10 min	1
Hold	4	∞^{+}	1

*Annealing temperature varies based on primer (T_m)
**Extension time is 1 min per kilobase of amplicon length
$^{+}$Indefinite hold at 4°C

The PCR product underwent restriction digestion with 1 µL FastDigest DpnI enzyme

(Thermo Scientific) and 3 µL FastDigest Buffer (Thermo Scientific) at 37°C for 3 hours to remove residual DNA templates. The digested products underwent separation through electrophoresis using a 1% agarose gel in Tris-acetate-EDTA (TAE) buffer with SYBR Safe DNA Gel Stain (Thermo Scientific). The samples underwent electrophoresis at 100 V for 25 minutes before excision of the target DNA band and purification using the QIAquick Gel Extraction Kit (QIAGEN). The purified DNA's $A_{260/280}$ ratio was considered pure DNA when the ratio was around 1.8.

The ligation step required mixing 8 µL of purified DNA with 1 µL of 10× ligation buffer and 1 µL of T4 DNA Ligase (Promega) and then incubating the mixture overnight at 16°C. Competent *E. coli* cells were transformed through an incubation on ice for 30 minutes with the ligation mixture, followed by a 42°C heat shock of 40 seconds and then a 1-hour recovery period in antibiotic-free lysogeny broth (LB) medium with 5% glucose at 37°C. The transformed cells were plated on agar with kanamycin and incubated overnight at 37°C.

Individual bacterial colonies selected after transformation were transferred to 2.5 mL of LB medium containing kanamycin. After overnight growth at 37°C with shaking, the cultures underwent plasmid DNA extraction using the ZR Plasmid Miniprep - Classic kit (Zymo Research) according to the manufacturer's protocol. The bacterial pellets were resuspended in 200 µL of P1 buffer followed by lysis with 200 µL of P2 buffer and neutralization with 400 µL of P3 buffer. Following centrifugation, the supernatant passed through a purification column, with sequential Endo-Wash and Plasmid Wash buffer washes before elution using 30 µL DNA Elution Buffer. The plasmid DNA output yielded an average concentration of 500 ng/µL and an $A_{260/280}$ absorption ratio of roughly 1.80.

The DNA sequencing was outsourced to Microsynth Seqlab (Göttingen, Germany) using their standard sequencing primers. Clones with proper sequences were further expanded, and the NucleoBond Xtra Maxi-Kit (Macherey-Nagel) was used for large-scale plasmid production.

To generate the domain-specific drebrin constructs, a sequential PCR-based cloning strategy was employed using phosphorylated primers to introduce domain deletions or truncations (see Tables 2.4 and 2.6 for details). The initial construct, *wt-drebrin-GFP* (Supp. Fig. A.1), served as the template for generating ΔADFH-GFP (Supp. Fig. A.2) via amplification with the *dreb Start phos rev* and ΔADFH *phos fw* primers. This intermediate construct was then used as a template for producing further deletions, including ΔADFH-ΔPP-drebrin-GFP (Supp. Fig. A.3) and CC-Hel-GFP (Supp. Fig. A.4), using combinations of ΔPP-specific primers. Additional constructs targeting the C-terminal region, PP-C-term-GFP (Supp. Fig. A.5) and C-term-GFP (Supp. Fig. A.6), were generated directly from *wt-drebrin-GFP* using primer pairs designed to include or exclude the ΔPP domain, respectively. All constructs were assembled using blunt-end ligation following DpnI digestion to remove template DNA, and verified by Sanger sequencing.

3.2   Isolation and Cultivation of Primary Human Macrophages

Primary human monocytes were isolated from buffy coats (provided by Dr. Franz Bentzien, UKE Transfusion Medicine, Hamburg). For each donor, 20 mL of buffy coat were layered over 15 mL of lymphocyte separation medium in 50 mL conical tubes and centrifuged at 450–460 × g for 30 minutes at 4°C with slow acceleration and deceleration. The leukocyte interphase was collected, washed twice with cold RPMI 1640 medium, and centrifuged at 450 × g for 10 minutes at 4°C.

The cell pellet was resuspended in 1.5 mL of cold monocyte buffer (DPBS with 2 mM EDTA and 0.5% human serum albumin) and incubated with 250 μL of CD14-conjugated magnetic beads for 15 minutes on ice. The labeled cells were applied to pre-equilibrated MS+ columns in a magnetic separator, washed twice with 1 mL monocyte buffer, and eluted with 3 mL buffer after column removal from the magnet.

Isolated CD14$^+$ monocytes were counted and seeded at 2×10^6 cells per well in 6-well plates with RPMI 1640 medium. After 4–5 hours adherence at 37°C (5% CO_2, 90–95% humidity), the medium was replaced with monocyte culture medium (composition not specified in source protocols). Cells were cultured for 6–7 days with one medium change after 24 hours to allow differentiation into macrophages.

3.3   Detachment of Macrophages for Experimental Procedures

Adherent primary human macrophages were detached from culture plates for experimental use. The culture medium was removed and cells were washed with sterile DPBS. Subsequently, 500 µL Accutase was added per well and incubated for 50 minutes at room temperature (22-25°C). The detachment reaction was stopped by adding 500 µL monocyte medium, and cells were dislodged by gentle pipetting.

The cell suspension was collected in 15 mL tubes and centrifuged at 450 × g for 5 minutes at room temperature. After supernatant removal, cells were resuspended in 5 mL sterile DPBS. Cell concentration was determined using a Neubauer counting chamber.

Detached macrophages were then prepared for immediate experimental use, either through transfection procedures or by direct seeding onto coverslips at appropriate densities.

3.4   Overexpression of Drebrin Domain Constructs

To evaluate protein overexpression, macrophages were washed three times with Dulbecco's Phosphate-Buffered Saline (DPBS) and subsequently detached using Accutase according to a standard protocol. Transfection was performed with the NEON electroporation system using a plasmid encoding the drebrin construct fused to green fluorescent protein (GFP). For each reaction, 500 ng of plasmid was transfected per 1×10^5 cells using a 10 µL transfection tip under optimized electroporation parameters (1000 V, two 40 ms pulses). Transfected cells were resuspended in antibiotic-free 90 µL Roswell Park Memorial Institute medium (RPMI) medium, and the resulting 100 µL suspension was seeded

onto 12 mm coverslips. After a 1 hour incubation at 37°C under 5% CO_2, monomedium was added, and cells were cultured until sufficient overexpression was achieved. Cells were then fixed with 3.7% methanol-stabilized formaldehyde for subsequent analysis.

3.5   Immunofluorescence Staining

The 12 mm sterile glass coverslips for cell seeding were placed into a 12-well plate at a density of 5×10^4 cells per coverslip. The plate was incubated at 37°C with 5% CO_2 to enable cell adherence. Following adequate incubation time, cells underwent fixation via a methanol-formaldehyde two-step protocol. The coverslips were quickly submerged in ice-cold 100% methanol before being moved to a 3.7% paraformaldehyde (PFA) phosphate-buffered saline (PBS) solution where they stayed for 10 minutes at ambient temperature. After fixation, cells underwent three PBS washes with five-minute intervals to eliminate the remaining fixative.

Coverslips underwent a 10-minute incubation with 0.5% Triton X-100 in PBS at room temperature to permeabilize cells and enable antibody penetration before undergoing three PBS washes. The coverslips were blocked against nonspecific binding sites by incubating them at room temperature for 30 minutes in a blocking buffer composed of 5% normal goat serum (NGS), 5% normal horse serum (NHS), 5% bovine serum albumin (BSA) in 0.05% Triton X-100 dissolved in PBS. The blocking procedure took place inside a humidified chamber as a measure to stop the samples from drying out.

The primary antibody staining process began with the preparation of a 30 µL droplet containing the primary antibody solution diluted in blocking buffer. The droplet containing the primary antibody solution was placed on Parafilm within a humidified chamber before coverslips were carefully flipped onto it to achieve uniform distribution of the antibody. Samples were incubated overnight at 4°C. The following day, coverslips returned to the 12-well plate and underwent three PBS washes for 5 minutes each on a rocker to eliminate non-specifically bound antibodies.

A 30 µL droplet of fluorescently conjugated secondary antibody solution diluted in blocking buffer was prepared for secondary antibody staining after primary antibody incubation and washing. Fluorescently labeled phalloidin was added to the solution for actin staining when required. The coverslips were set inverted over the antibody droplet and left to incubate for 30 minutes at room temperature in a humidity-controlled chamber while keeping them protected from light. Coverslips received three PBS washes for five minutes each after incubation to eliminate excess antibody and lower background fluorescence signals.

Fluoromount-G (Invitrogen) was utilized to attach coverslips onto glass slides for imaging purposes to maintain fluorescence. The coverslip was carefully lowered onto a small Fluoromount-G droplet placed on the slide while making sure no air bubbles were trapped. Samples mounted on slides were kept at 4°C and shielded from light until they were imaged. The fluorescence microscopy procedure utilized a confocal microscope system while maintaining uniform exposure settings for all samples.

3.6 Proximity Ligation Assay (PLA)

The DUOLINK proximity ligation assay (PLA) Kit (Red Detection, Sigma-Aldrich) was used to perform a PLA as per the manufacturer's instructions for studying the spatial proximity between two proteins of interest. The technique identifies protein interactions occurring within 40 nm molecular distances and uses species-matched isotype control antibodies for assay specificity validation. After detachment through the standard protocol, cultured cells were placed onto glass coverslips at a density of 5×10^4 cells per coverslip. The cells were incubated for one hour at 37°C with 5% CO_2 to allow adherence before adding culture medium for three more hours. The coverslips were briefly submerged in ice-cold methanol for fixation before being incubated for ten minutes in 3.7% methanol-stabilized formaldehyde at room temperature.

Cells underwent permeabilization through a 10-minute incubation in 0.5% Triton X-100 in PBS before blocking for one hour at room temperature in a buffer containing 5% BSA, 5% NGS, and 5% NHS with 0.05% Triton X-100 in PBS. Species-specific primary antibodies and their respective isotype controls were applied at a 1:100 concentration in blocking buffer to tag the proteins of interest. A 40 µL droplet of the primary antibody solution was applied to coverslips and then incubated overnight at 4°C within a humidified chamber.

After primary antibody incubation, coverslips were washed in buffer A provided in the DUOLINK kit before incubation with species-matched PLA probes (PLUS and MINUS probes). The species-matched PLA probes were diluted 1:5 in antibody diluent and Phalloidin-405 for actin visualization before incubation for one hour at 37°C. The reaction proceeded with a ligase-containing solution at 37°C for 30 minutes during the ligation step. The signal amplification process involved incubating the coverslips in a polymerase solution within a preheated humid chamber at 37°C for 100 minutes. To reduce nonspecific background signals, the sample underwent stringent washing with buffers A and B between each step.

The coverslips were mounted onto slides with Fluoromount-G Mounting Medium and then stored until imaging at 4°C away from light. Confocal microscopy detected PLA signals as distinct puncta at an emission wavelength of λ_{em} 624 nm.

3.7 BioPixel Development

The BioPixel Suite is a Python-based image analysis framework designed to facilitate the processing of multidimensional microscopy images. The suite is built on top of the `numpy` and `scikit-image` libraries, providing a user-friendly interface for analyzing complex imaging data. The project is structured into several modules, each responsible for specific tasks within the image processing pipeline.

The pipeline is designed to be modular, allowing for easy integration of new features and functionalities as needed. The core modules include:

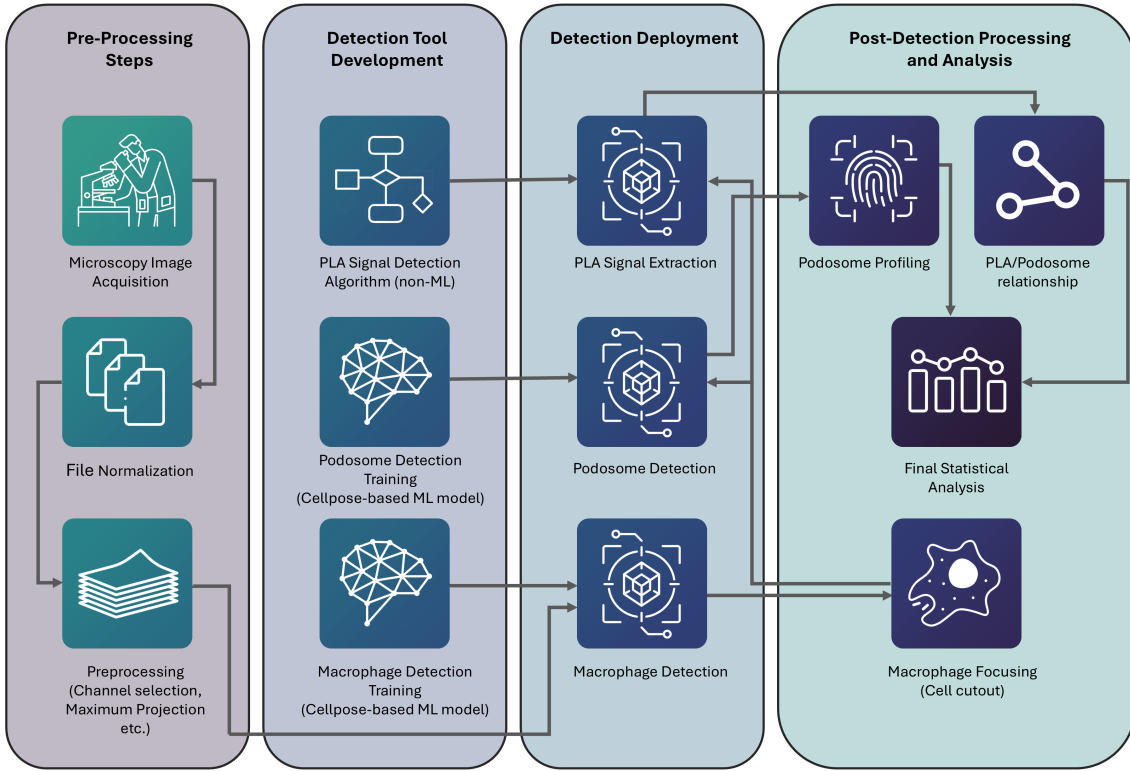- `image_tensors.py`: This module handles the reading and conversion of microscopy

Figure 3.1: **BioPixel pipeline.** Schematic of the BioPixel workflow: from inital data acquisition to feature extraction and data presentation.

images into a standardized format, ensuring compatibility with downstream analysis tools.

- `image_processor.py`: This module contains the core image processing algorithms, including projection operations and tensor manipulation.

- `detector.py`: This module implements the detection algorithms for podosomes and PLA signals, providing a comprehensive suite of tools for analyzing cellular structures.

- `cell_analysis.py`: This module focuses on the analysis of data such as the spatial distribution of podosomes and PLA signals, as well as podosome profiling.

- `visualization.py`: This module provides tools for visualizing the results of the analysis, in particular plotting results and generating publication-ready figures.

- `experiment_runner.py`: This module serves as the main entry point and orchestrator for the entire pipeline, allowing users to run the analysis on their data with minimal setup. It currently provides a command-line interface for easy execution and configuration of the pipeline.

The BioPixel pipeline is designed to be user-friendly, with a focus on providing clear documentation and examples to help users navigate the various modules and functionalities. The suite is intended for use by researchers in the field of cell biology, particularly those interested in studying the dynamics of cellular structures and their interactions. While

the current implementation is as described in this thesis, the project remains dynamic and is subject to ongoing development and changes that cannot be fully anticipated at this time.

3.7.1 Standardizing Microscopy Images via Modular Conversion

The pipeline enables seamless user interaction with the `ImageReader` class that automatically chooses file formats for Leica LIF, Olympus OIB, Nikon ND, Zeiss CZI and standard TIFF files without requiring manual input. Users access one interface while the framework assigns tasks to specific classes including `LifImageReader` and `CziImageReader` which inherit from the `BaseImageReader` class. The design maintains uniform treatment of metadata and dimensional information alongside TIFF conversion regardless of the file format. The system's modular design supports effortless integration of new file types through base class extension and format-specific logic implementation which guarantees adaptability for future development. The system transforms metadata details including pixel resolutions, z-stack intervals, and channel properties into ImageJ-compatible tags via a dataclass while maintaining essential acquisition data such as spatial calibration and temporal sequencing.

The image processing pipeline ensures consistent data structure by converting all input images to a five-dimensional TZCYX format, regardless of the original input dimensions. The algorithm processes images incrementally through a generator-based technique which outputs arrays one by one to avoid full dataset storage in memory to manage large or multi-series files efficiently. Images with lower dimensions like 3D z-stacks get transformed to match the TZCYX axis arrangement and handles multi-series acquisitions through iterative processing of discrete 5D arrays. Normalization creates a unified format for downstream processing to eliminate the need to handle differences from various proprietary or non-proprietary data sources. Outputs are generated as multidimensional TIFF files that contain embedded metadata to ensure both analysis tool compatibility and ensures original experimental parameters remain traceable. The pipeline minimizes computational demands in later analysis steps by abstracting format-specific differences while maintaining reproducibility across different datasets.

The module is part of the BioPixel project under `image_tensors.py`.

3.7.2 Tensor Processing for Downstream Detection

The module's core functionality is implemented in the `Projection` class, which initializes 5D image tensors using the `TifImageReader` class imported from the `image_tensors` module. The module connects raw tensor normalization with downstream detection through processing of multidimensional imaging data. The module processes tensors which follow a structure with separate dimensions for time sequences, optical sections (Z-slices), channels, and spatial coordinates. Users have the option to examine dynamic processes by selecting specific timepoints or ranges, limit Z-slices to target a specific area of interest, or choose channels that highlight particular fluorescent markers.

The module continues processing the selected data by applying projection operations. maximum intensity projection (MIP) works by detecting the brightest pixel value at each spatial position throughout Z-slices to highlight structures with high-intensity signals like fluorescently labeled cells. Average projection calculates the mean pixel intensity from all Z-slices which removes noise but maintains spatial structure. The two operations transform Z-dimensional data into 2D representations with the help of NumPy's optimized array functions. This step preserves spatial metadata such as pixel resolution and formats outputs to work with downstream tools which allows seamless integration with object detection and intensity-based quantification tasks.

The BioPixel project includes this specialized submodule, `image_processor.py`, which is responsible for handling image processing tasks.

3.7.3   Macrophage Detection

The macrophage detection and processing pipeline is implemented through two main Python classes: `CellPoseDetector` and `MacrophageDetector`. The `CellPoseDetector` class serves as a general-purpose detection module that interfaces with the Cellpose deep learning model, while `MacrophageDetector` specializes this for macrophage-specific analysis. The `CellPoseDetector` initializes with an input image array and a comprehensive set of parameters controlling the detection process. Key parameters include the model type (defaulting to the macrophage model described in Section 3.8), detection and auxiliary channel specifications, object diameter estimation, 3D processing capability, and segmentation thresholds for flow and cell probability. The detector automatically handles channel extraction from multi-dimensional input arrays, supporting both 4D (czyx) and 5D (tczyx) data structures through its tensor extraction method, allowing time-lapse processing at the single-frame level, though full temporal tracking across sequences is not yet supported. For optimal processing, the implementation includes functionality to pad images to a minimum specified canvas size, addressing cases where macrophages were acquired with narrow margins (e.g., due to high zoom) that could otherwise cause model failures from insufficient surrounding context. The system maintains the ability to precisely trim outputs back to original dimensions post-detection.

The core detection method employs the Cellpose model evaluation, generating labeled masks through deep learning-based segmentation. The `MacrophageDetector` builds upon this foundation with macrophage-specific optimizations. It operates by first extracting the specified channel from the input volume and identifying the 2D slice with highest intensity through z-axis analysis. This intensity-based slice selection ensures analysis focuses on the most biologically relevant plane. The detector then applies the Cellpose model with macrophage-optimized parameters, including an adjustable diameter parameter and flow threshold. Post-processing options include the ability to isolate only the centermost detected macrophage, particularly useful for single-cell analyses. The implementation provides functionality to extract and yield only the masked regions of interest through its blackout method, which generates cropped subvolumes containing just the detected macrophage areas while zeroing out all background pixels. This combined approach en-

ables robust macrophage identification and isolation while maintaining flexibility through parameter customization at both the general Cellpose and macrophage-specific processing levels.

BioPixel Suite implements the full detection pipeline through its `MacrophageDetector` class in `detector.py`.

3.7.4 Podosome Detection

The podosome detection pipeline, implemented in the `PodosomeDetector` class, begins by preprocessing the 3D image stack, extracting the F-actin channel to define podosome cores. The highest-intensity slice is chosen for initial analysis as it provides the most accurate representation of podosome localization. To enhance feature visibility, this 2D projection undergoes contrast-limited adaptive histogram equalization (CLAHE), improving local contrast while suppressing noise.
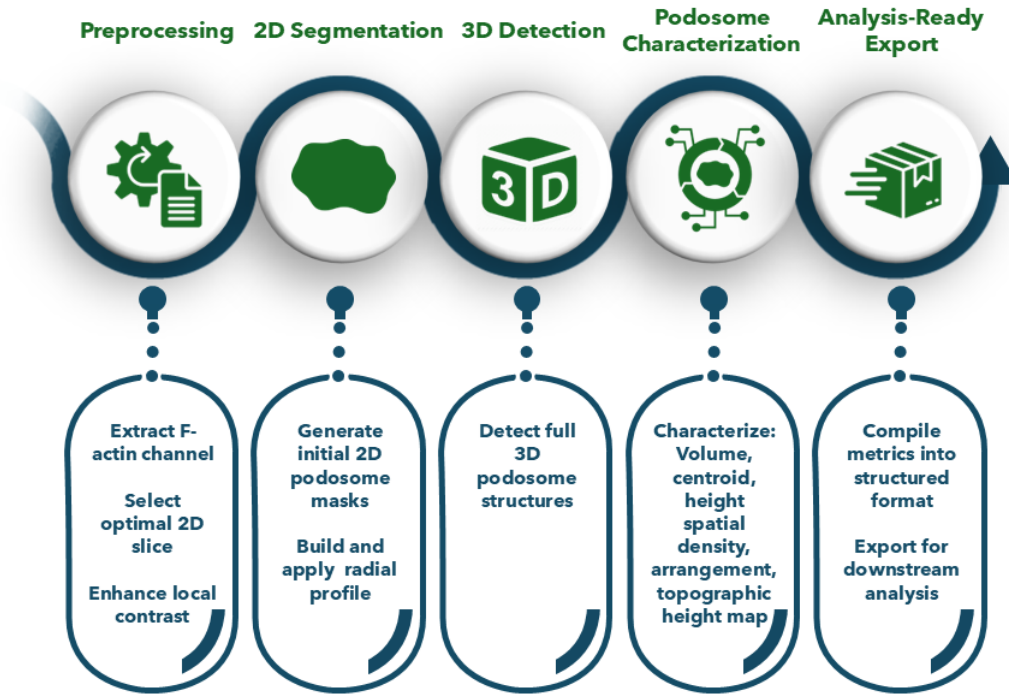
Figure 3.2: **Podosome characterization pipeline.** Schematic of the 3D podosome detection workflow: from preprocessing F-actin images to feature extraction and data export. Each stage represents an automated step, culminating in quantitative podosome metrics and microenvironment mapping.

For segmentation, a podosome-specific pretrained CellPose model (as described in Section 3.8) is utilized in a two-pronged approach. The first stage generates an initial 2D mask from the highest-intensity slice to construct a tapered intensity profile that assigns voxel weights based on their proximity to the podosome core. When applied to the original 3D stack, the processing enhances the visibility of podosome structures through legitimate contrast adjustment while suppressing distant background, without altering the underlying data or introducing artificial features. The second stage performs full 3D segmentation by running the same 2D model on orthogonal slices (xy, xz, yz), averaging the resulting flow fields and cell probabilities, then stitching masks across adjacent z-slices

using an Intersection over Union (IoU) threshold of ≥ 0.25. Masks from consecutive z-planes are merged into a single 3D podosome when they share $\geq 25\%$ overlap, ensuring biologically plausible reconstruction while avoiding over-merging of distinct objects. The reconstruction process excludes any 3D structures with volumes lower than 10% of the median podosome volume which ensures only structurally coherent podosomes are included in detection (Stringer et al., 2021).

The 3D analysis treats all podosomes as independent entities at single timepoints. The modular data structure (bounding boxes/centroids/volumes) is inherently compatible with – though not currently implemented for – temporal tracking of fusion/fission events. A critical step involves 3D dilation of the masks using resolution-adjusted elliptical kernels (accounting for anisotropic voxel dimensions in XY vs Z) scaled to $1.5\times$ the median podosome core diameter. This dilation is not intended to correct under-segmentation, but rather to define a podosome-associated volume surrounding the core structure, capturing both the dense actin core and its immediate microenvironment, such as the ring structure and the cap.

For spatial analysis, the system supplies a topographic map encoding each podosome's relative vertical position, where voxel intensities represent normalized height values with the base defined as $\frac{1}{n}$ (with n set as the number of slices that are positive for an individual podosome's mask) and the apex as 1.0. The mapping system keeps three-dimensional structural data intact after projection while allowing quantitative examination of signals along the z-axis. Each voxel is assigned a height value that corresponds to its position in a podosome's z-stack during the initial map construction to yield smooth vertical gradients. The algorithm computes average height values in areas where multiple dilated podosome regions intersect to accurately reflect their shared microenvironment space. Finally, original core boundaries are preserved by having undilated voxels override any calculated values, maintaining precise podosome architecture while realistically modeling overlap regions.

This systematic approach enables comprehensive characterization of podosome architecture and associated molecular distributions while maintaining clear distinction between core and associated dilated volumes. The resulting data structure extracts both individual podosome features (including spatial coordinates, volume, and bounding boxes) and population-level representations, allowing flexible access to either single-podosome metrics or collective representations such as binary 3D masks of all detected structures. These outputs provide base data for downstream analyses including the correlation of podosome morphology with spatial PLA signals while maintaining a logical separation between detection and quantification processes from statistical interpretation.

The full pipeline is implemented in the `PodosomeDetector` class and available as part of the BioPixel Suite contained in the `detector.py` module.

3.7.5 PLA Signal Detection

Through a multi-phase analytical process the signal detection pipeline progressively refines signal identification while maintaining comprehensive coverage in its structured rigorous

framework. Analytical integrity is maintained throughout all processing stages by two core principles. Every processing stage deliberately processes an excess of candidate signals to minimize missed detections, particularly important in 3D stacks where physical structures are likely to appear across multiple slices or intensity thresholds. The program creates thresholding intervals beginning at 40% of the image maximum intensity and increases these values in 10-unit increments to apply them on Gaussian-blurred images for candidate region isolation. These values were determined through empirical testing across a range of images to ensure consistent and accurate region identification. Validated signals are immediately masked to avoid redundant detection results while ensuring each analytical method maintains its unique contribution. The initial phase of this non-ML algorithm processes the raw 3D image stack through extraction of the specific channel of interest and creation of a maximum intensity projection (MIP). CLAHE is applied to this MIP to optimize its performance for following detection operations.
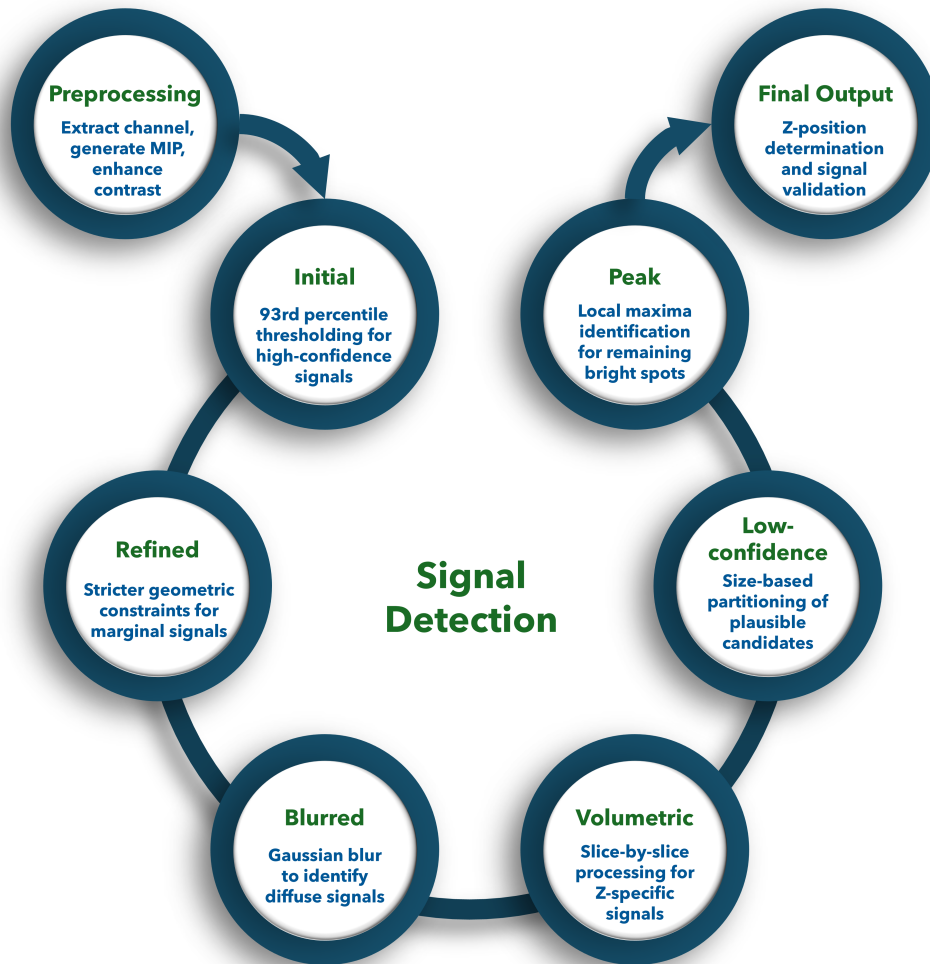
Figure 3.3: **Multi-phase Signal Detection Pipeline.** Schematic representation of the non-ML signal detection algorithm showing the progressive refinement process from raw 3D image stack to validated signals. Each phase employs complementary detection strategies with intermediate masking steps to ensure comprehensive signal identification while preventing redundant detections.

The initial detection stage prioritizes capturing solitary, well-defined signals through conservative thresholding at the 93rd percentile of intensities in the MIP. The 93rd per-

centile intensity threshold was selected to balance specificity (avoiding noise) and sensitivity (capturing faint signals), as validated in testing. A solid high-confidence baseline is achieved that allows further sensitive analysis techniques to be applied afterwards. The second phase applies stricter geometric limits and increased intensity requirements to find marginally visible signals which passed the initial filtering on the residual image after masking initial detections. The algorithm then reduces the resolution by applying Gaussian blurring to the remaining image data for detection purposes. The method is highly effective at pinpointing diffuse or low-contrast signals that may not be apparent at full resolution.

During volumetric analysis each slice from the original 3D stack is subjected to the same identical iterative thresholding technique applied in 2D detection. The procedure facilitates detection of signals at precise Z-positions or specific intensity ranges in the stack and resolves overlapping signals which would remain ambiguous using MIP detection. The subsequent non-strict detection pass finds low-confidence candidates with plausible characteristics but fell short of stricter upstream criteria. This ensures minimal false negatives. These signals are partitioned into two groups: (1) signals meeting the minimum size threshold, which are retained without further filtering due to their higher inherent reliability, and (2) smaller signals below the threshold, which undergo additional validation to mitigate elevated risks of noise or artifactual detection.

Peak detection functions as the final detection measure and works separately from contour-based techniques to locate local intensity maxima within remaining image sections. This method proves highly effective in locating small bright spots that earlier thresholding stages might have missed. Once all signal candidates are identified, the exact Z-positions are calculated through the evaluation of intensity sums within circular regions of interest throughout the original 3D stack before assigning each signal to its optimal axial position. The analysis process maintains integrity through sequential signal removal between stages which guarantees clean data for every processing step and eliminates duplicate detections. The analysis produces a comprehensive suite of verified signals with defined spatial coordinates and geometric characteristics along with intensity measurements that enable quantitative biological analysis.

The `SignalDetector` class in the BioPixel Suite's `detector.py` module contains the full implementation of this processing pipeline.

3.7.6   Spatial Association Analysis of Podosomes and PLA Signals

The spatial relationship between podosomes and protein-protein proximity signals was analyzed using a custom Python-based image analysis framework. The `PLAAnalyzer` class serves as a tool for quantitatively measuring the relationship between podosomes and PLA signals from three-dimensional confocal microscopy images. The `PLAAnalyzer` processes multi-channel image data that contains separate fluorescence channels for podosomes and PLA signals. When initialized the analyzer receives a multi-dimensional image array which it processes automatically through specialized detection modules. The `PodosomeDetector` class enables podosome detection within the specified channel by iden-

tifying each podosome structure and producing a detailed label map that represents their spatial arrangement (Section 3.7.4). Concurrently, PLA signals are identified in a separate channel using the `SignalDetector` class (Section 3.7.5). A critical feature of the `PLAAnalyzer` is its ability to establish spatial relationships between detected PLA signals and podosome structures. This association is mapped through several sequential operating steps. The analyzer begins by acquiring a dilated mask from the `PodosomeDetector` which represents the peripheral areas around podosome structures. The `PLAAnalyzer` assesses each detected signal to check if it resides inside the expanded podosome area and records this information as a boolean value. The analyzer conducts additional spatial analysis of signals linked to podosomes to determine the most pertinent podosome linked with each signal. To establish the closest podosome for each signal the system calculates the three-dimensional Euclidean distance between the signal's coordinates and the centroid of each neighboring podosome. The podosome that shows the minimum distance is identified as the nearest podosome while the relationship and computed distance value are stored together for downstream analysis. The analyzer integrates topographical data by mapping relative height values to signals according to their locations inside the three-dimensional volume. Topographical mapping delivers additional context to study how signals spatially associate with podosome structures. Multiple analytical features within the `PLAAnalyzer` enable quantitative assessments of spatial relationships. The analysis includes both counts of podosome-associated signals and non-associated signals and provides methods for extracting detailed spatial information about each signal. The comprehensive method allows meticulous statistical evaluation of spatial distribution patterns which quantitatively analyzes protein-protein proximity dynamics with podosome structures under a multitude of experimental settings. This analytical framework enables objective assessment of spatial correlations between protein-protein proximity and podosomes which reveals the molecular composition and functional organization of these dynamic cellular structures.

3.7.7 Structural Scores

The calculation of the four scores (core, cap, ring, and diffusion) is a systematic process designed to quantify specific structural properties of the analyzed aggregate podosome profiles. Each step in the computation is motivated by a clear rationale that ensures the scores are meaningful and interpretable. The following provides a detailed description of how each score is computed, along with the reasoning behind each step.

The **core score** (S_c) quantifies the relative intensity and structural prominence of the core region compared to the rest of the podosome. To begin, the global median (m) and global mean (μ) of the intensity distribution across the entire structure are calculated as

$$m = \text{median}(I), \tag{3.1}$$

$$\mu = \text{mean}(I). \tag{3.2}$$

The median (3.1) is chosen because it is robust to outliers, ensuring that extreme values do not skew the baseline intensity measure. The mean (3.2) provides a complementary

measure of central tendency, capturing the overall intensity level. An adjusted standard deviation (σ_{adj}) is then computed using the formula

$$\sigma_{\text{adj}} = \frac{\sigma(I) \cdot m}{\mu}, \tag{3.3}$$

to account for overall intensity variation. This adjustment normalizes the standard deviation by the ratio of the median to the mean, ensuring that the variability is scaled appropriately relative to the central tendency. Next, the core region's statistics are evaluated. The normalized core sum (S) is defined as

$$S = \frac{\sum I_{\text{core}}}{m}, \tag{3.4}$$

which scales the total intensity of the core region by the global median. This normalization ensures that the core's contribution is expressed relative to the overall intensity distribution, making it comparable across different structures. Similarly, the normalized core mean (μ_c) is given by

$$\mu_c = \frac{\text{mean}(I_{\text{core}})}{m}. \tag{3.5}$$

This normalization allows for a direct comparison of the core's intensity to the global baseline. The core standard deviation (σ_c) is computed as

$$\sigma_c = \text{std}(I_{\text{core}}), \tag{3.6}$$

to quantify the variability within the core region. To assess the core's dominance over its surroundings, the adjacent regions—the ring and cap—are considered. Their respective means,

$$\mu_r = \text{mean}(I_{\text{ring}}), \tag{3.7}$$

$$\mu_p = \text{mean}(I_{\text{cap}}), \tag{3.8}$$

are used to compute the core prominence (P_c) as

$$P_c = \frac{\mu_c}{\mu_r + \mu_p}. \tag{3.9}$$

This formula (3.9) captures the relative intensity of the core compared to its surroundings, emphasizing its prominence. Finally, the core score (S_c) is computed by combining these components into the formula

$$S_c = \left(\frac{S}{\sigma_c}\right) \times \sigma_{\text{adj}} \times P_c. \tag{3.10}$$

This formula (3.10) balances the core's total intensity, variability, and prominence, providing a comprehensive measure of its structural significance.

The **cap score** (S_p) evaluates the structural relationship between the ring and cap

regions in terms of their relative organization and distribution within the averaged po-
dosome profile. To begin, the variability of the ring and cap regions is quantified through
their respective standard deviations,

$$\sigma_r = \text{std}(I_{\text{ring}}), \tag{3.11}$$

$$\sigma_p = \text{std}(I_{\text{cap}}). \tag{3.12}$$

These measures quantify the variability in signal distribution within each region, where
higher values indicate more heterogeneous or punctate patterns. Additionally, the median
intensity of the cap region (m_p) is calculated as

$$m_p = \text{median}(I_{\text{cap}}). \tag{3.13}$$

The median (3.13) is chosen here to ensure robustness against outliers in the cap region. A
variability ratio (R_v) is then computed to compare the heterogeneity of signal distribution
between the ring and cap regions, using the formula

$$R_v = \frac{\sigma_r}{\sigma_p}. \tag{3.14}$$

This ratio (3.14) provides insight into the relative smoothness or roughness of the two
regions, which can be indicative of structural differences. The final cap score (S_p) is
obtained by normalizing the sum of the variability ratio and the cap median by the core
score, as shown in the formula

$$S_p = \frac{R_v + m_p}{S_c}. \tag{3.15}$$

This normalization (3.15) ensures that the cap score reflects the structural relationship
between the ring and cap regions while accounting for the overall prominence of the core.

The **ring score** (S_r) quantifies the distinctness of the ring region. To compute this
score, the median (m_r) of the ring region is first determined as

$$m_r = \text{median}(I_{\text{ring}}), \tag{3.16}$$

while the mean of the ring region (μ_r) is already defined in Equation (3.7). A standard
deviation ratio (R_s) is then computed to compare the variability of the ring and cap
regions, using the formula

$$R_s = \frac{\sigma_r}{\sigma_p}. \tag{3.17}$$

This ratio (3.17) provides a measure of the relative texture of the two regions. To measure

how distinct the ring is from the cap, a ring-cap contrast (Q) is defined as

$$Q = \frac{\mu_r / \mu_p}{R_s}.$$ (3.18)

This formula (3.18) captures the relative intensity difference between the ring and cap, normalized by their variability, ensuring that the contrast is not confounded by differences in texture. The final ring score (S_r) combines the ring's strength and quality by incorporating the ring median, contrast, and normalization by the core and cap scores. It is computed as

$$S_r = \left(\frac{m_r}{m} \right) \times \frac{Q}{S_p + S_c}.$$ (3.19)

This formula (3.19) ensures that the ring score reflects both the ring's prominence and its distinctness from the cap, while being normalized by the contributions of the core and cap.

The **diffusion score** (S_d) measures the degree of structural disorganization. To begin, the podosomal median (m_{podo}) is calculated as the median intensity of the combined core, ring, and cap regions,

$$m_{\text{podo}} = \text{median}(I_{\text{core}} \cup I_{\text{ring}} \cup I_{\text{cap}}).$$ (3.20)

This measure (3.20) provides a robust estimate of the central intensity of the entire podosome structure. Additionally, the background mean (μ_{bg}) is determined as

$$\mu_{\text{bg}} = \text{mean}(I_{\text{bg}}).$$ (3.21)

The Structural Predictability Index (SPI) detects repeating patterns by comparing the maximum to median autocorrelation strength, using the formula

$$SPI = \frac{\max\limits_{m,n} \left(\sum\limits_{x,y} I(x, y) \cdot I(x + m, y + n) \right)}{\text{median} \left(\left\{ \sum\limits_{x,y} I(x, y) \cdot I(x + m, y + n) \right\}_{\forall m,n} \right)}$$ (3.22)

This measure (3.22) identifies the presence of organized structures, with higher values indicating more pronounced patterns. Finally, the diffusion score (S_d) is obtained by combining the autocorrelation peak, the podosomal median, the background mean, and the previously computed scores. It is given by the formula

$$S_d = \frac{SPI}{S_c \cdot S_p \cdot S_r \cdot (m_{\text{podo}} / \mu_{\text{bg}}) \cdot Q}.$$ (3.23)

This formula (3.23) balances the degree of organization (captured by SPI) against the structural prominence of the core, cap, and ring regions, as well as the intensity contrast

between the podosome and the background. Higher values of S_d indicate greater structural disorganization, making this score a sensitive indicator of structural integrity.

To ensure the interpretability and comparability of the structural scores, each score was benchmarked against established biological markers representing the core components of podosome structures. Specifically, the **core score** (S_c) was benchmarked against F-actin, a key structural protein in the podosome core; the **ring score** (S_r) against vinculin, a marker of the stabilizing ring region; the **cap score** (S_p) against α-actinin, associated with actin bundling in the cap region; and the **diffusion score** (S_d) against GFP-only signal, which serves as a proxy for disorganized or diffuse fluorescence patterns. For each benchmark, the corresponding score was assigned a reference value of 10, representing an idealized structural profile. All computed scores were normalized relative to these benchmarks, enabling quantitative comparisons and ensuring that deviations from the reference values could be meaningfully assessed.

3.8   BioPixel Model Training and Evaluation

A rigorous evaluation framework was implemented to quantify BioPixel detection performance on both macrophage and podosome imaging datasets. Each dataset underwent randomized partitioning into training, validation, and test subsets to eliminate sampling bias. The macrophage dataset consisted of 114 images containing a total of 408 macrophage cells, split into 80 images (70%) with 278 cells (68%) for training, 12 images (11%) with 56 cells (14%) for validation, and 22 images (19%) with 74 cells (18%) for testing. This split followed the conventional 70/10/20 rule, ensuring a balanced representation of macrophage cells across all subsets.

For the podosome dataset, which contained only 21 images but a much higher object density (10,991 podosomes in total), the split ratio was adjusted to 60/20/20, diverging from the conventional 70/10/20 rule. In this case, 12 images (57%) with 4,977 podosomes (45%) were used for training, 4 images (19%) with 3,244 podosomes (30%) for validation, and 5 images (24%) with 2,770 podosomes (25%) for testing. This adjustment was necessary due to the smaller total number of images in the podosome dataset. Despite the smaller image count, the high object density ensured that each subset maintained sufficient data representation for robust evaluation.

Model training was performed using Cellpose's train_seg function with the cytoplasmic ("cyto3") architecture. Hyperparameters, including learning rate (0.05), weight decay (0.0001), batch size (8), and number of epochs (200), were manually selected. The model was trained on the training set, with performance evaluated on the validation set during training. The train_seg function saves model weights at regular intervals, and the first saved checkpoint is returned. Although a more robust approach would involve evaluating all saved checkpoints on the validation set to select the best-performing model, limited computational resources and minimal differences observed in validation metrics during initial experiments justified the use of the first checkpoint for all downstream evaluations. During testing, this saved model was applied to the macrophage and podosome test images to generate binary segmentation masks, which were then evaluated against

Table 3.2: Training, validation, and testing splits for macrophage and podosome datasets

	Images	**Objects**
Macrophages		
Training	80 (70%)	278 (68%)
Validation	12 (11%)	56 (14%)
Testing	22 (19%)	74 (18%)
Total	114	408
Podosomes		
Training	12 (57%)	4977 (45%)
Validation	4 (19%)	3244 (30%)
Testing	5 (24%)	2770 (25%)
Total	21	10991

expert-annotated ground truth using a mask-matching protocol that paired predicted and true masks whenever their intersection-over-union exceeded 0.2. Future implementations should incorporate a systematic evaluation of all saved checkpoints, selecting the highest-performing model based on predefined validation metrics before proceeding to final testing and deployment.

Detection performance was summarized by counting true positives, false positives, and false negatives. For each matched pair of predicted and ground truth masks, the Intersection over Union (IoU) metric was calculated as the ratio of intersecting pixels to the union of the two masks and then aggregated across all matches. Recall overlap was defined as the ratio of intersecting pixels to the total number of pixels in each ground truth mask. The F1 score, equivalent to the Dice coefficient, was computed as twice the overlap divided by the sum of the predicted and ground truth mask sizes. Radial shape similarity, which evaluates geometric concordance, was assessed by comparing radial distances sampled in 360 directions from the centroids of matched masks and reported as mean, median, and standard deviation values. Additionally, error rates were quantified by calculating the false positive rate, defined as the proportion of predicted mask pixels not belonging to any ground truth object, and the false negative rate, representing the proportion of ground truth mask pixels missed by the detector. These metrics collectively provide a comprehensive and reproducible assessment of detection accuracy, spatial localization fidelity, and morphological agreement for the models on both macrophage and podosome datasets.

The trained models for macrophage and podosome detection, as described above, were subsequently utilized for the analysis of experimental datasets presented in Section 3.7.4 for podosome detection as well as macrophage segmentation (Section 3.7.3) for cell-focused analysis. The entire training, validation, and testing pipeline, along with the implementation of the evaluation metrics, was integrated into the BioPixel suite and is available in the module utils/cellpose_training_and_testing.py, ensuring reproducibility and ease of adaptation for future studies.

4 Results

4.1 Drebrin subdomains

To investigate the localization of drebrin to specific substructures within podosomes, a series of GFP-fused deletion constructs were designed and overexpressed in primary macrophages. These constructs were engineered to systematically probe the role of individual domains in targeting drebrin to distinct podosome substructures. Drebrin's multidomain architecture includes an N-terminal actin-depolymerizing factor homology (ADFH) (Larbolette et al., 1999) region (aa 1-135), a coiled-coil (CC) region regulating homodimerization (aa 176-256), a helical domain (Hel; aa 257-355), a polyproline region (PP; aa 364-417) known to bind afadin (Rehm et al., 2013), and a long unstructured C-terminal region (Worth et al., 2013). Notably, the CC and helical (Hel) regions contain a "cryptic domain" capable of independently binding F-actin and cooperatively bundling actin filaments upon phosphorylation of Ser142, which relieves an intramolecular interaction. The experimental series consisted of five GFP-fused deletion constructs including ΔADFH-GFP that lacks the N-terminal ADFH region: ΔADFH-ΔPP-GFP which excludes both the N-terminal ADFH and polyproline (PP) regions; CC-Hel-GFP that retains only the coiled-coil and helical regions; PP-C-term-GFP that combines the PP region with the C-terminal region; and C-term-GFP which features only the unstructured C-terminal region. A schematic representation of these constructs, along with the domain organization of full-length drebrin, is provided in Figure 4.1.

Fluorescence microscopy data displayed in Figure 4.2 demonstrated unique localization patterns for each construct that were quantified and scored according to their enrichment in the podosome core, cap, ring, or cytoplasmic diffusion (Figure 4.3).

All localization scores (range: 0–10) are normalized to reference markers, where 10 indicates ideal colocalization (Methods 3.7.7). The ΔADFH-GFP construct, which lacks the ADFH domain, exhibited a strong cap-like localization at podosomes, as evidenced by a cap score of 8.03. This suggests that the ADFH domain is dispensable for targeting drebrin to the podosomal cap. Similarly, the ΔADFH-ΔPP-GFP construct, which additionally lacks PP, retained a pronounced cap-like localization with an even higher cap score of 9.45. This further confirms that neither the ADFH nor the PP regions are essential for drebrin's association with the podosome cap. Both constructs also displayed moderate enrichment at the ring, with scores of 3.60 and 4.49, respectively, while showing minimal diffusion into the cytoplasm, as reflected by their low diffusion scores of 0.92 and 0.44. These localization patterns are visually represented in Figure 4.2, rows 1 and 2.
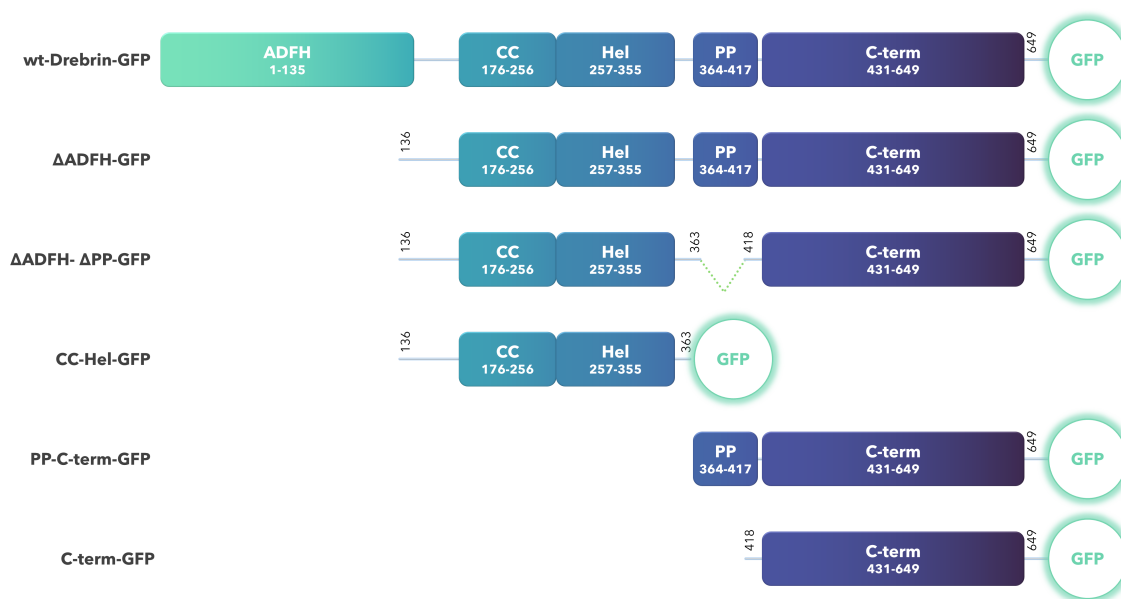
Figure 4.1: **Drebrin Deletion Constructs Used for Podosomal Localization Analysis.** Schematic representation of drebrin deletion constructs used to identify domains involved in podosomal localization, shown from top to bottom: wildtype drebrin domain structure, a construct lacking the ADFH domain (ΔADFH-GFP), a construct lacking both the ADFH and PP domains (ΔADFH-ΔPP-GFP), a construct containing only the coiled-coil and helical domains (CC-Hel-GFP), a construct containing the PP and C-terminal regions (PP-C-term-GFP), and a construct containing only the C-terminus of drebrin (C-term-GFP). Domain boundaries are indicated by their first and last amino acid residues, and all constructs are C-terminally tagged with GFP.

In contrast, the CC-Hel-GFP construct, which contains only the CC and Hel regions, exhibited a markedly different localization pattern. This construct preferentially localized to the podosome core, achieving a core score of 5.75, while showing minimal enrichment at the cap (1.15) and diffusion (0.27). These findings suggest that the CC and Hel regions are critical for targeting drebrin to the podosome core, potentially through their ability to bind F-actin or mediate cooperative actin bundling. However, the absence of the C-terminal region in this construct appears to limit its ability to localize to the cap, highlighting the importance of the C-terminal region in facilitating cap-specific localization. The core localization of the CC-Hel-GFP construct is illustrated in Figure 4.2, row 3.

The PP-C-term-GFP construct, which includes the PP and C-terminal regions, showed a more dispersed localization pattern. While it exhibited moderate enrichment at the core (2.60), cap (2.39), and ring (2.22), its relatively high diffusion score of 3.04 indicates significant cytoplasmic dispersion. This suggests that the PP and C-terminal regions alone are insufficient to confer robust localization to any specific podosome substructure. Notably, the apparent enrichment of the PP-C-term-GFP construct at the core may be influenced by fixation artifacts, as methanol-based fixation has been known to precipitate fusion proteins, potentially leading to artificial accumulation at dense structures such as the podosome core. This possibility warrants further investigation using live-cell imaging approaches to confirm the true localization dynamics of this construct under physiological conditions. Similarly, the C-term-GFP construct, which consists solely of the unstructured C-terminal region, displayed a predominantly diffuse localization with a diffusion score of
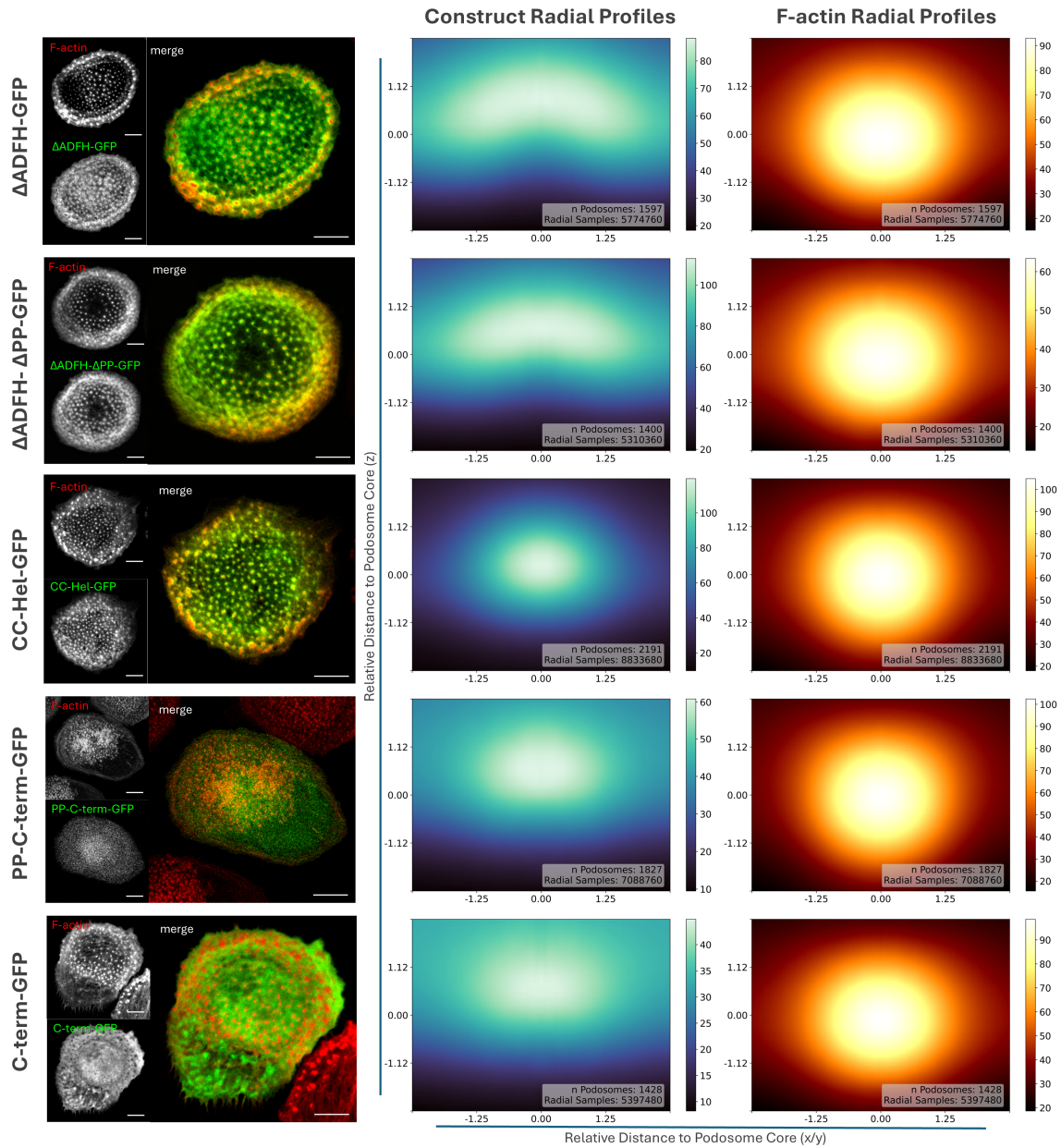
Figure 4.2: **Spatial Localization of Drebrin Constructs At Podosomes.** The figure is organized into three columns, each providing complementary information about the localization and distribution of various drebrin constructs around podosomes. **(Left Column)** Confocal imaging data for five tested drebrin constructs: a construct lacking the ADFH domain (ΔADFH-GFP), a construct lacking both the ADFH and PP domains (ΔADFH-ΔPP-GFP), a construct containing only the coiled-coil and helical domains (CC-Hel-GFP), a construct containing the PP and C-terminal regions (PP-C-term-GFP), and a construct containing only the C-terminus of drebrin (C-term-GFP). Each row corresponds to one construct and includes GFP signal (expressed construct), F-actin channel, and a merged image of the two channels. **(Middle Column)** Normalized intensity profiles (in x, y, and z dimensions) of the GFP-labeled constructs around podosomes, showing either sagittal or frontal views (equivalent in this context due to the side-on perspective of podosomes). The number of podosomes analyzed and radial profiles are indicated in each profile visualization. **(Right Column)** Normalized intensity profiles of the F-actin channel around podosomes, used to analyze the podosome core structure, with corresponding counts for podosomes and radial profiles.

9.93. Its low scores for core (2.96), cap (1.73), and ring (1.35) further underscore the inability of the C-terminal region to independently target drebrin to podosomes. The dispersed patterns of these constructs are depicted in Figure 4.2, rows 4 and 5.
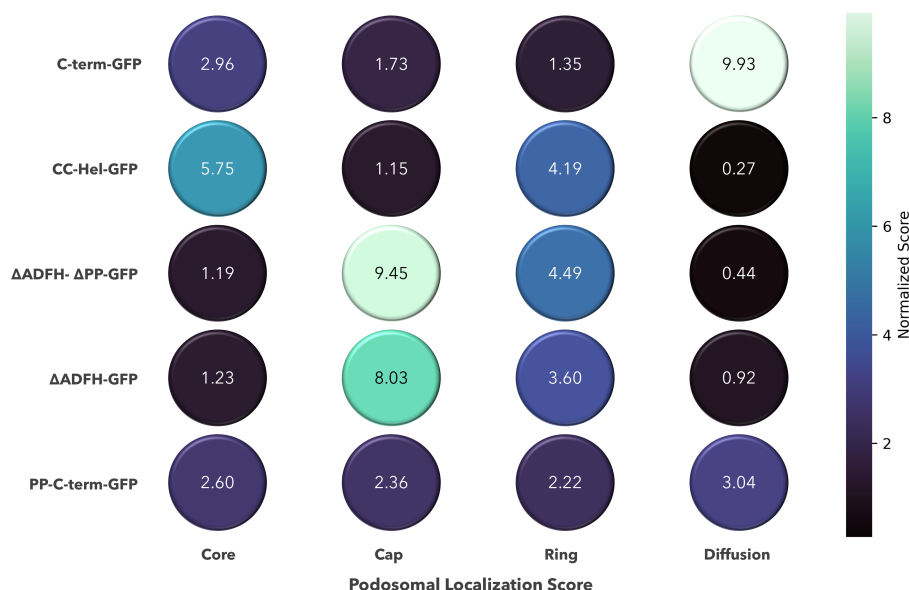
Figure 4.3: **Heatmap of Drebrin Construct Localization Scores.** Localization scores for five drebrin constructs (ΔADFH-GFP, ΔADFH-ΔPP-GFP, CC-Hel-GFP, PP-C-term-GFP, C-term-GFP) are displayed for four metrics: core, cap, ring, and diffusion. The heatmap represents the relative localization intensity of each construct across these categories, providing insights into their spatial distribution around podosomes.

Taken together, these results indicate that the localization of drebrin to the podosome cap is mediated by the combined presence of the CC, Hel, and C-terminal regions. Neither the ADFH nor the PP regions appear to play a significant role in this process. The CC and Hel regions are crucial for targeting drebrin to the podosome core, likely due to their actin-binding properties, but the inclusion of the C-terminal region is necessary for cap-specific localization. These findings, supported by the fluorescence profiles in Figure 4.2 and the quantification in Figure 4.3, provide insight into the modular organization of drebrin and highlight the interplay between its structural domains in determining subcellular localization. However, further validation using live-cell imaging techniques will be essential to rule out potential artifacts introduced by fixation protocols and to fully elucidate the dynamic behavior of drebrin constructs within podosomes.

4.2 Proximity of Drebrin, EB3 and Clathrin-coated Vesicles

To further elucidate the spatial relationships between drebrin and its potential interacting partners at podosomes, proximity ligation assays (PLA) were employed to investigate the nanoscale associations of drebrin with both clathrin heavy chain (CHC) and EB3. The PLA technique enables visualization of protein proximity with high sensitivity by generating fluorescent signals when two proteins are within 40 nm of each other.
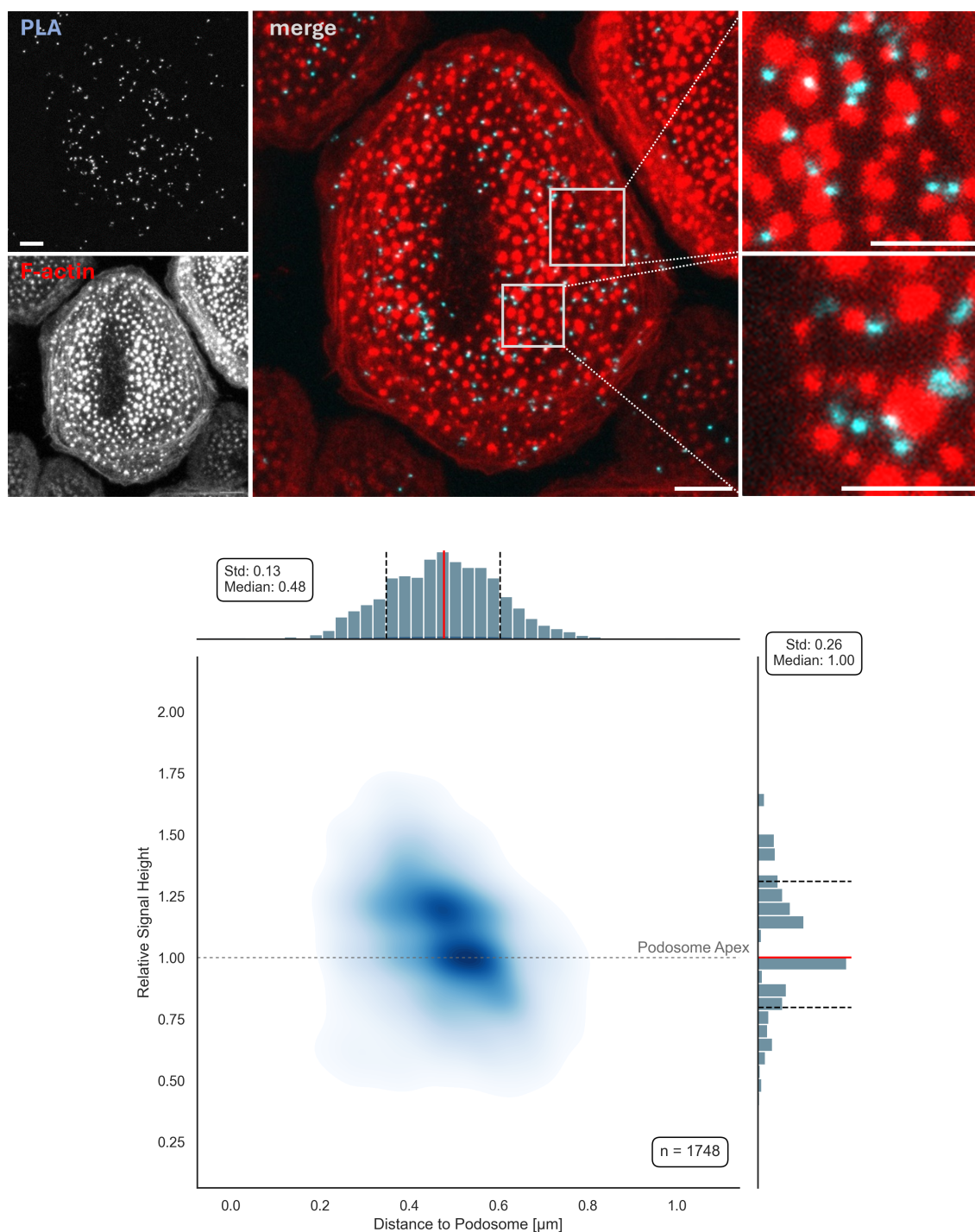
Figure 4.4: **Drebrin-clathrin proximity and spatial association with podosomes. Top:** Confocal micrographs of macrophages, with single channel images showing Proximity Ligation Assay (PLA) signal (blue in merge), using anti-drebrin and anti-clathrin heavy chain antibodies, and F-actin (red in merge), both in the left column with merge in the center. White boxes in merge indicate selected regions of interest shown enlarged in the right column, highlighting PLA signals in close proximity to podosomes, while being absent in podosome-poor regions. All images are maximum intensity projections from z-stacks. Scale bars: 5 μm for whole cell images, 2 μm for selected regions. **Bottom:** KDE plot with x-axis representing distance to podosome in μm and y-axis showing relative signal height to the podosome. Frequency distributions of both measurements are shown along their respective axes. Gray horizontal line demarks the podosome apex. Distance to podosome has a median of 0.48 μm with standard deviation of 0.13 μm. Relative height has a median of 1.00 with standard deviation of 0.26. n = 1,748 podosomes. Only podosome-associated signals were considered, which are signals in a 1 μm radius around a 3D podosome. The data comes from 3 donors with 10 cells acquired in z-stack per donor.

Initial investigations focused on the spatial relationship between CHC and drebrin. Primary macrophages were processed for PLA using antibodies specific for drebrin and CHC, followed by F-actin staining to identify podosome structures. Confocal microscopy revealed numerous distinct PLA signals throughout the processed cells (Fig. 4.4; top), with specificity confirmed by isotype controls and antibody verification detailed in Supp. Fig. A.7(a,b). Notably, these PLA signals were predominantly localized adjacent to podosomes while being conspicuously absent from podosome-free areas (Fig. 4.4; ROIs). This spatial distribution pattern strongly indicates a close association between drebrin and CHC specifically at podosome sites.
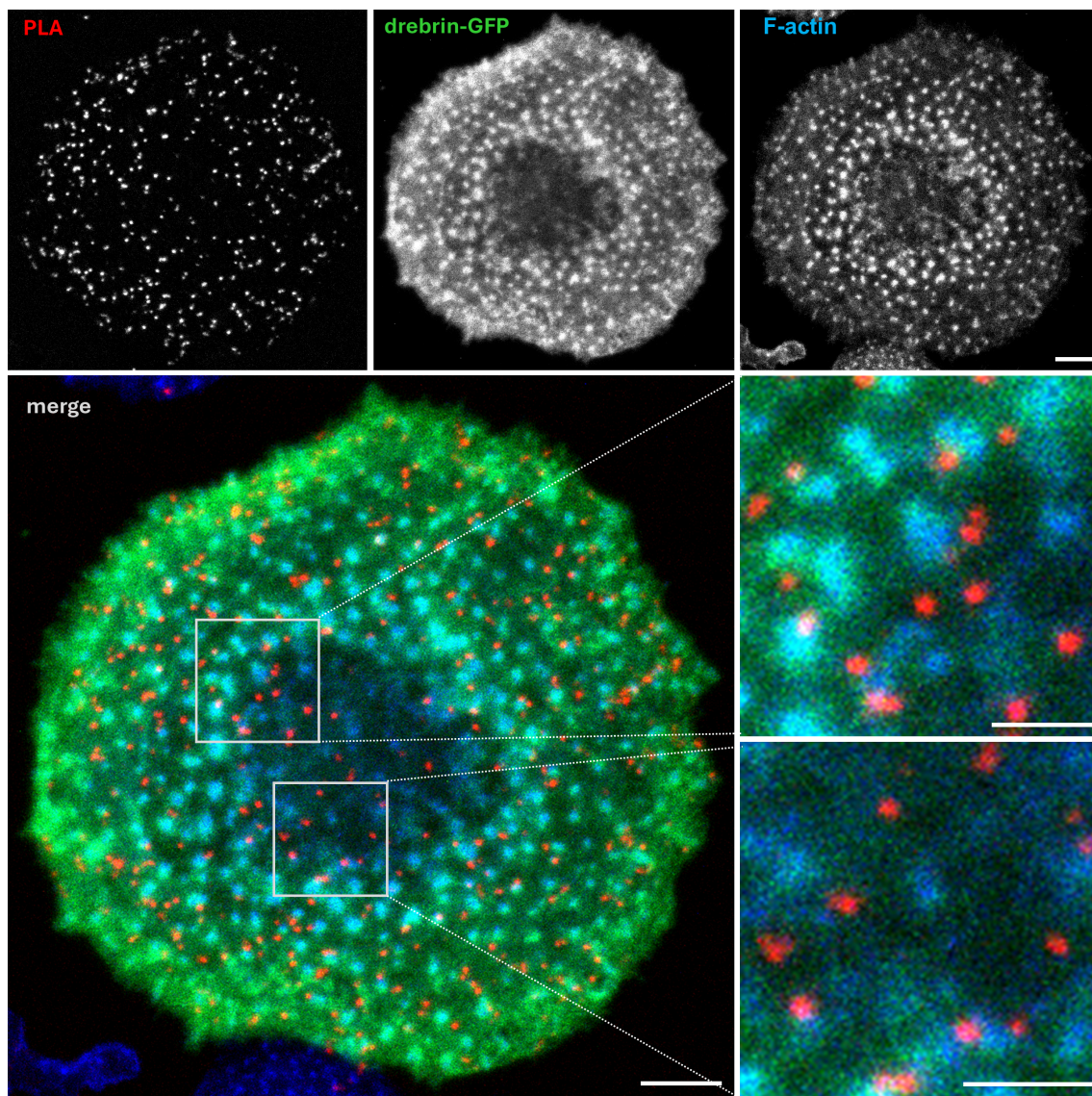
Figure 4.5: **Drebrin-GFP and EB3 are closely associated at podosomes.** Confocal micrographs of macrophage processed for proximity ligation assay (PLA) using GFP- and EB3-specific antibodies, with respective PLA signals in red, with cell overexpressing drebrin-GFP, and stained with Alexa405 phalloidin for F-actin to label podosome cores (top row). Left bottom is merge. White boxes in merge indicate detail regions shown in the bottom right. Note PLA signals adjacent to podosomes, but absent in podosome-free areas. Scale bars: 5 µm in overviews, 2 µm in detail images.

Quantitative analysis of the spatial distribution of these PLA signals was performed using tools from the BioPixel Suite. The analysis focused on podosome-associated signals, defined as those within a 1 µm radius of three-dimensional podosomes. Kernel density estimation (KDE) plots with accompanying distance and height distribution histograms revealed that the CLH1-drebrin PLA signals exhibited a median distance of 0.48 µm (standard deviation 0.13 µm) from podosome centers. In terms of relative height, these signals demonstrated a median value of 1.00 (standard deviation 0.26) relative to the podosome apex (Fig. 4.4; bottom). These quantitative measurements were derived from the analysis of 1,748 podosomes across cells obtained from three independent donors, with ten cells analyzed per donor.
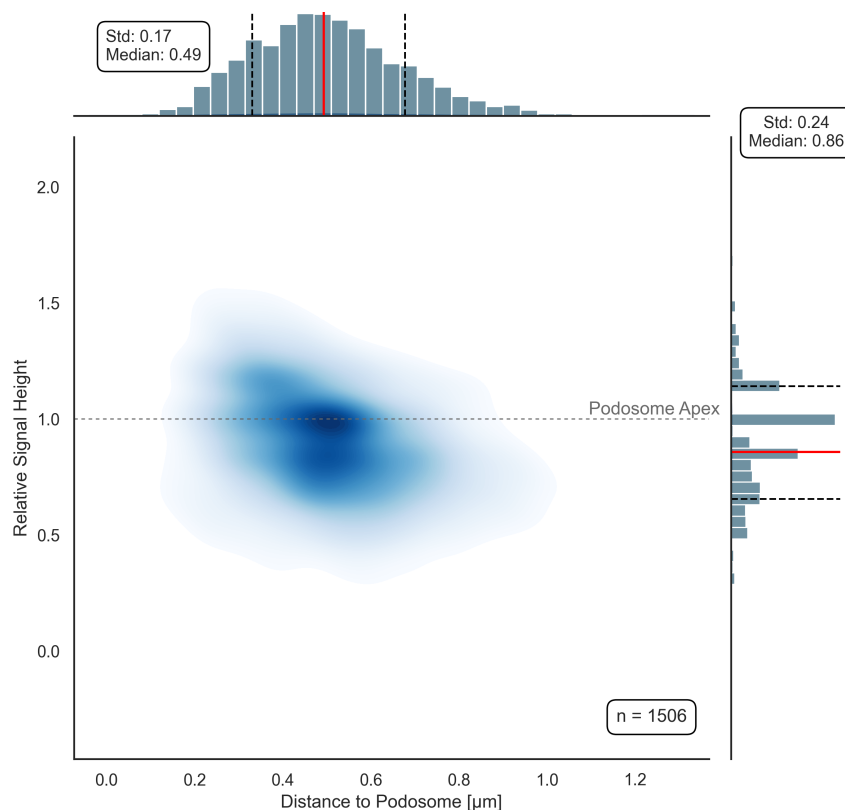
Figure 4.6: **Spatial relationship between drebrin-EB3 PLA signals and podosomes.** KDE plot with x-axis representing distance to podosome in µm and y-axis showing relative signal height to the podosome. Frequency distributions of both measurements are shown along their respective axes. Gray horizontal line demarks the podosome apex. Distance to podosome has a median of 0.49 µm with standard deviation of 0.17 µm. Relative height has a median of 0.86 with standard deviation of 0.24. n = 1,506 podosomes. Only podosome-associated signals were considered, which are signals in a 1 µm radius around a 3D podosome. The data comes from 3 donors with 10 cells acquired in z-stack per donor.

The spatial relationship between drebrin and EB3 was subsequently examined. While the direct binding between drebrin and EB3 is well established in the literature (Geraldo et al., 2008; Bazellières et al., 2012; Worth et al., 2013), the subcellular localization of this interaction remained unclear. To address this question, proximity ligation assays were conducted using primary macrophages overexpressing drebrin-GFP, together with anti-EB3 and anti-GFP antibodies. Overexpression of drebrin-GFP was necessitated by the incompatibility of primary antibodies against drebrin and EB3 for PLA protocols. F-actin was visualized using Alexa405 phalloidin to identify podosome structures.

As anticipated, the overexpressed drebrin-GFP localized to the cap structure of po-dosomes. The PLA experiment revealed numerous signals, with specificity validated through isotype controls and antibody verification as shown in Supp. Fig. A.7(c,d). Detailed examination of the spatial distribution demonstrated that the drebrin-EB3 PLA signals were predominantly located adjacent to podosomes, while being largely absent from podosome-free regions (Fig. 4.5). This observation provides strong evidence that drebrin and EB3 maintain a close spatial relationship (less than 40 nm) specifically at podosome sites.

Quantitative analysis of the drebrin-EB3 PLA signals, again performed using the BioPixel Suite, revealed a median distance of 0.49 µm (standard deviation 0.17 µm) from podosome centers. The relative height of these signals showed a median value of 0.86 (standard deviation 0.24) compared to the podosome apex (Fig. 4.6). These measurements were based on the analysis of 1,506 podosomes across cells from three independent donors, with ten cells analyzed per donor.

Collectively, these findings demonstrate that both clathrin and EB3 exhibit close spatial associations with drebrin specifically at podosome sites, suggesting potential functional interactions between these proteins in podosome regulation or dynamics.

4.3 +TIP Heterogeneity in Macrophages

To better understand the molecular mechanisms underlying cytoskeletal organization, fluorescence microscopy was performed to investigate the potential heterogeneity of microtubule plus-end tracking proteins (+TIPs) in macrophages (Fig. 4.7). The localization of CLIP-170 and EB3, two key +TIPs, was visualized relative to the microtubule network. Microtubules and EB3 were visualized using immunofluorescence staining with anti-β-tubulin and anti-EB3 antibodies, respectively. CLIP-170 was detected through overexpression of a GFP-tagged construct.

A clearly heterogeneous pattern of decoration of microtubule plus ends by +TIPs was observed. In some regions, plus ends were predominantly decorated by either CLIP-170 or EB3. In other regions where both proteins localized to the same plus end, they were often positioned on opposite sides of the microtubule cylinder. This suggests that even within a single cell, microtubule plus-end composition can vary at a fine spatial scale. This spatial arrangement was consistently observed, with images obtained from three independent donors and three fields of view analyzed per donor.

At this stage, a quantitative analysis of +TIP distribution was not performed due to the lack of automated tools for assessing heterogeneity. Future studies should aim to quantify the proportions of plus ends decorated by CLIP-170 alone, EB3 alone, or both proteins to provide a more comprehensive understanding of +TIP dynamics.

Taken together, the results demonstrate that +TIP composition at microtubule plus ends is highly dynamic and context-dependent, reflecting potential differences in microtubule regulation within macrophages.
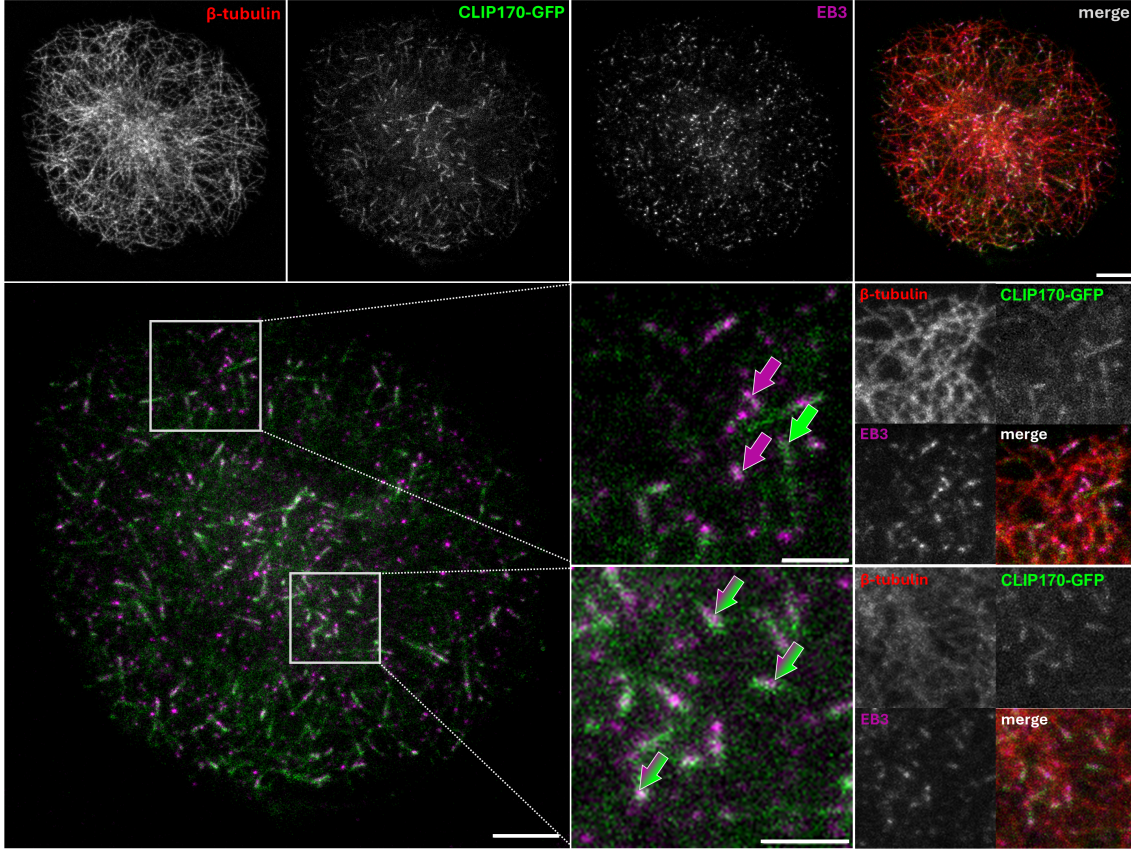
Figure 4.7: **Localization of +TIP proteins CLIP-170 and EB3 in macrophages.** Top row: single-channel images of β-tubulin (AF568), CLIP-170-GFP, and EB3 (AF405), followed by a merged image of all three channels (β-tubulin in red, CLIP-170 in green, and EB3 in purple). Bottom left: wider field of view showing CLIP-170-GFP and EB3 distribution without the tubulin channel, with two white boxes marking regions of interest (ROIs). The ROI above highlights microtubule plus ends with preferential decoration by either CLIP-170 or EB3 (arrows); the ROI below shows plus ends with comparable levels of both signals (arrows). Each ROI is presented alongside corresponding single-channel and merged images including β-tubulin. Images were acquired from macrophages derived from three independent donors, with three fields of view per donor. Scale bars: 5 μm (single-channel and merged full-cell images); 2 μm (ROI images).

4.4 BioPixel Macrophage Detection

The performance of BioPixel in detecting macrophages was evaluated using a comprehensive set of metrics aimed at capturing both detection accuracy and segmentation quality. An example segmentation is presented in Fig. 4.8. Out of a total of 75 ground truth masks, BioPixel correctly identified 70 instances (true positives), missed 5 (false negatives), and did not produce any false positives, reflecting a strong detection outcome with a false positive rate of zero (Fig. 4.9a).

Segmentation quality was assessed primarily using the Intersection over Union (IoU), which evaluates the overlap between predicted and ground truth masks. BioPixel achieved a mean IoU of 0.85 with a median of 0.91 and a standard deviation of 0.19 (Fig. 4.9b), indicating high spatial agreement. The model achieved high recall overlap scores, indicating substantial coverage of the ground truth regions. The mean recall overlap reached 0.96, with a median of 0.99 and a standard deviation of 0.15 (Fig. 4.9c), suggesting that the model rarely failed to cover relevant regions of interest.
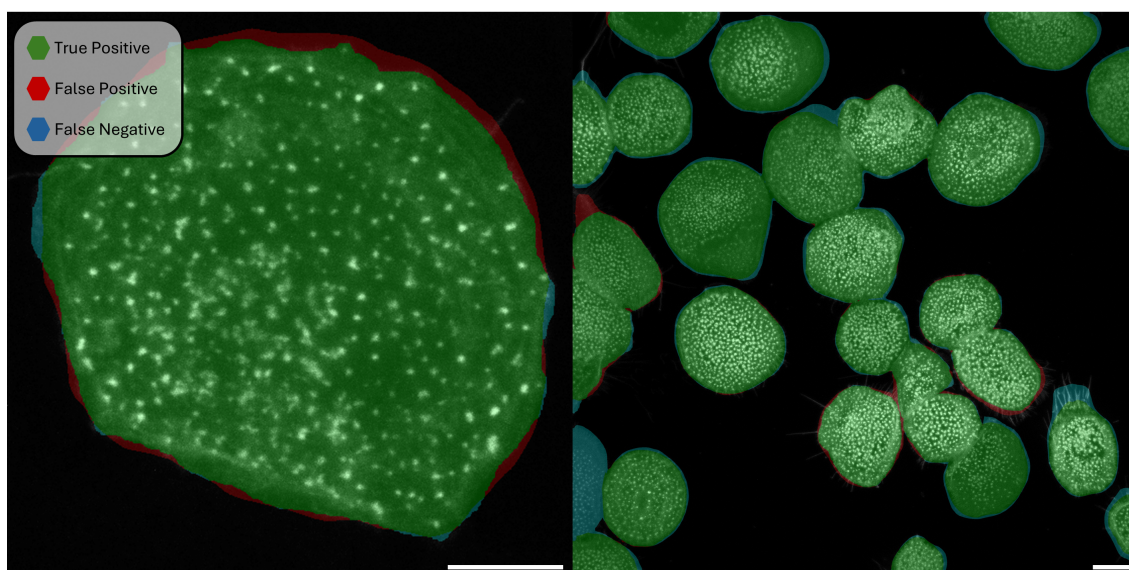
Figure 4.8: **Macrophage segmentation results.** Left: Single cell with error overlay (TP: green, FP: red, FN: blue). Right: Multi-cell overview showing detection consistency. Scale bars: 5 μm .
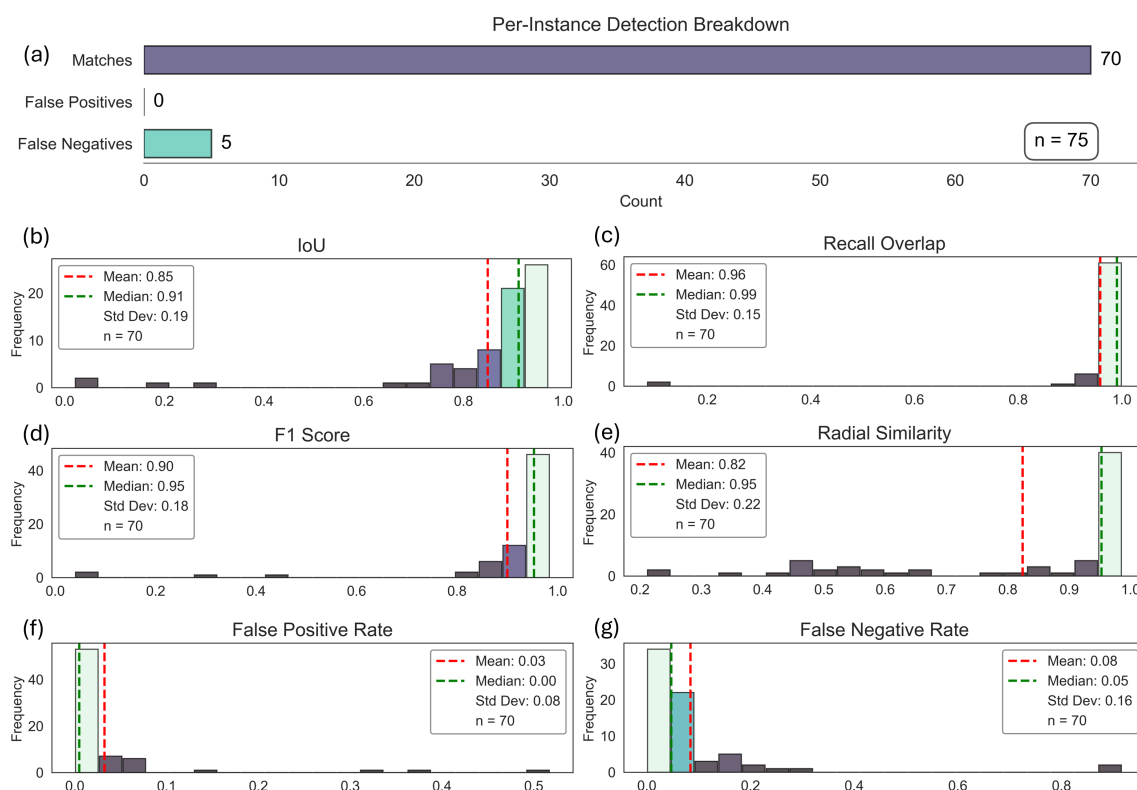

Figure 4.9: **Evaluation of BioPixel for Macrophage Detection and Segmentation.** (a) Summary of detection outcomes across all annotated macrophage instances, including True Positives (Matches), False Positives, and False Negatives (n = 75). (b-g) Metrics derived from the set of matched macrophage pairs (n = 70), where each predicted mask was successfully aligned with a corresponding ground truth annotation. (b) Distribution of Intersection over Union (IoU) scores, measuring pixel-wise overlap between predicted and ground truth masks. (c) Recall Overlap, assessing the extent to which predicted masks cover their corresponding ground truth objects. (d) F1 Score, balancing precision and recall across the matched dataset. (e) Radial Similarity, evaluating shape fidelity by comparing predicted macrophage contours to idealized radial profiles. (f) False Positive Rate (FPR), defined as the proportion of predicted mask pixels not overlapping with the corresponding ground truth, calculated individually for each matched pair. (g) False Negative Rate (FNR), representing the proportion of ground truth macrophage pixels not captured by the predicted mask, also computed per object pair. All metrics in subplots (b-g) reflect per-object, pixel-level comparisons within the matched set, offering detailed insights into detection accuracy and morphological consistency.

59

To evaluate the balance between precision and recall, the F1 score was calculated and showed consistently high values, with a mean of 0.90, a median of 0.95, and a standard deviation of 0.18 (Fig. 4.9d). This metric underscores the reliability of BioPixel in providing both accurate and comprehensive segmentations.

In recognition of the limitations of global overlap metrics for objects with irregular morphology, a radial similarity metric was employed to assess shape fidelity. The results yielded a mean radial similarity of 0.82 and a median of 0.95, with a standard deviation of 0.22 (Fig. 4.9e), reflecting strong conformity to expected macrophage morphologies despite local boundary variability.

The model's reliability was further reflected in its minimal error rates. The mean false positive rate was just 0.03 (median 0.00, SD 0.08; Fig. 4.9f), and the false negative rate was similarly low, with a mean of 0.08 (median 0.05, SD 0.16; Fig. 4.9g). Together, these values illustrate the robustness of BioPixel in distinguishing macrophages from background or irrelevant structures.

In addition to the metrics presented in the figure, Boundary IoU was also computed for reference. While this metric offers increased sensitivity to contour misalignment, especially for complex or irregular shapes, BioPixel achieved lower values (mean = 0.11, median = 0.04, SD = 0.11). Given the dynamic and flexible nature of macrophage morphology, particularly their fine pseudopodial extensions, Boundary IoU may over-penalize minor discrepancies, limiting its biological interpretability in this context.

4.5   BioPixel Podosome Detection

The BioPixel `PodosomeDetector` class, a Cellpose-based machine learning model trained for podosome detection in 2D fluorescence microscopy images, was evaluated using a comprehensive set of segmentation performance metrics applied to n = 2683 segmented podosome instances. The evaluation compared algorithm-generated segmentations to manually curated ground truth annotations, focusing on both object-level detection accuracy and pixel-level shape fidelity. An example of the segmentation results is shown in Fig. 4.10.

At the most fundamental level, the confusion matrix revealed strong detection performance: 2683 true positives were identified, indicating successful alignment between predicted and annotated podosome masks. Only 80 false positives were recorded, demonstrating the algorithm's high specificity and low tendency to erroneously detect non-existent podosomes. A total of 87 false negatives were observed, pointing to cases where actual podosomes were not fully captured by the predicted masks, potentially due to low signal intensity, overlapping structures, or morphological variability (Fig. 4.11a).

To assess spatial overlap between predicted and ground truth masks, the Intersection over Union (IoU) metric was calculated. IoU evaluates the degree of pixel-wise overlap, providing a direct measure of localization accuracy. Across all matched podosomes, the algorithm achieved a mean IoU of 0.64, a median of 0.72, and a standard deviation of 0.21, indicating generally strong alignment with the ground truth, albeit with some variation across samples (Fig. 4.11b).
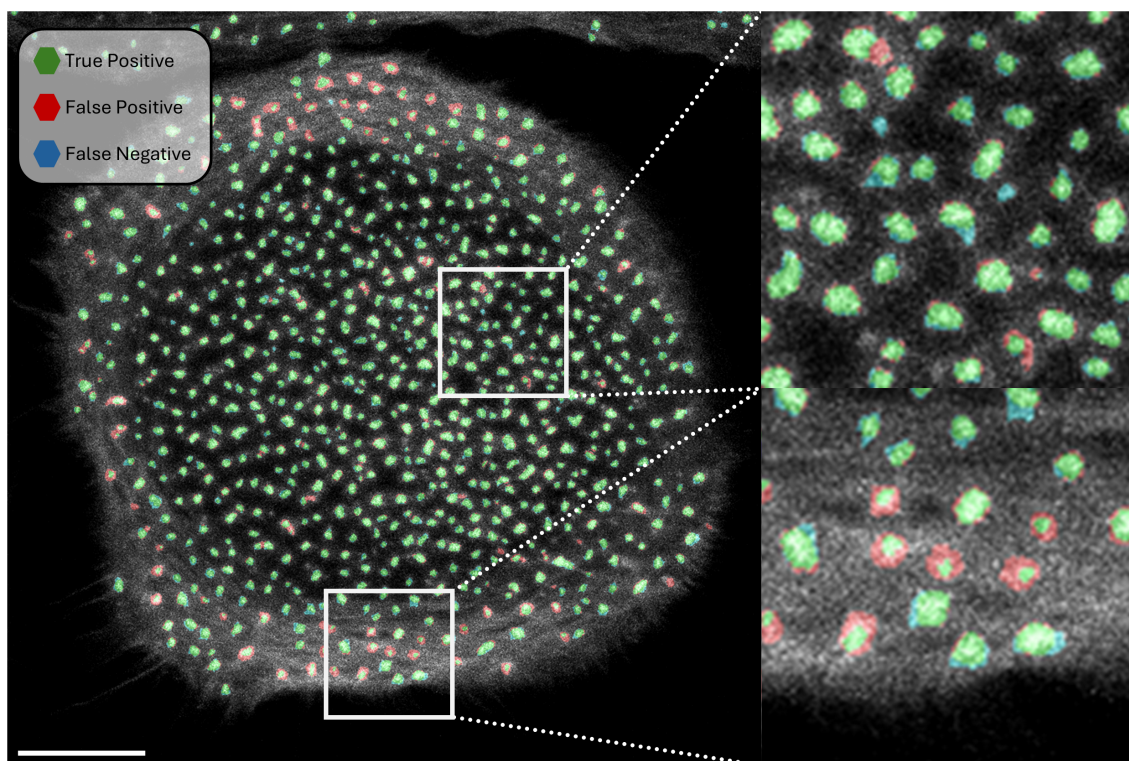
Figure 4.10: **Podosome segmentation results in a macrophage.** The left panel shows the original image with error overlay: true positives (TP, green), false positives (FP, red), and false negatives (FN, blue). Insets highlight regions of interest (ROIs) — top-right: exemplary FN (blue, missed podosomes); bottom-right: predominant FP (red, over-detections). Scale bar: 5 μm.

The Recall Overlap, which measures the extent to which the predicted mask covers the ground truth podosome, yielded a mean of 0.93 and a median of 0.97, with a relatively low standard deviation of 0.13 (Fig. 4.11c). These results suggest that, in most cases, the algorithm successfully captures nearly the full extent of each podosome, contributing to its robust recall performance.

Balancing precision and recall, the F1 Score provides a composite view of detection accuracy. The algorithm attained a mean F1 score of 0.76, with a median of 0.84 and a standard deviation of 0.20 (Fig. 4.11d), indicating overall solid performance, though with some variability depending on image characteristics and podosome morphology.

An important indicator of segmentation reliability is the False Positive Rate (FPR), which here reflects the proportion of pixels in a predicted mask that do not overlap with the corresponding ground truth. Across all matched podosomes, the mean and median FPR were both 0.00, with no standard deviation, indicating that the vast majority of predicted podosome masks contained no extraneous background pixels (Fig. 4.11f). This suggests that the algorithm rarely includes irrelevant regions when defining podosome boundaries. In contrast, the False Negative Rate (FNR) - defined as the proportion of ground truth podosome pixels not included in the predicted mask - showed a mean of 0.17, a median of 0.07, and a relatively high standard deviation of 0.24 (Fig. 4.11g). This indicates that while many predicted masks closely align with the ground truth, certain podosomes exhibit significant under-segmentation, particularly in edge cases involving irregular shapes or weak fluorescence signals.
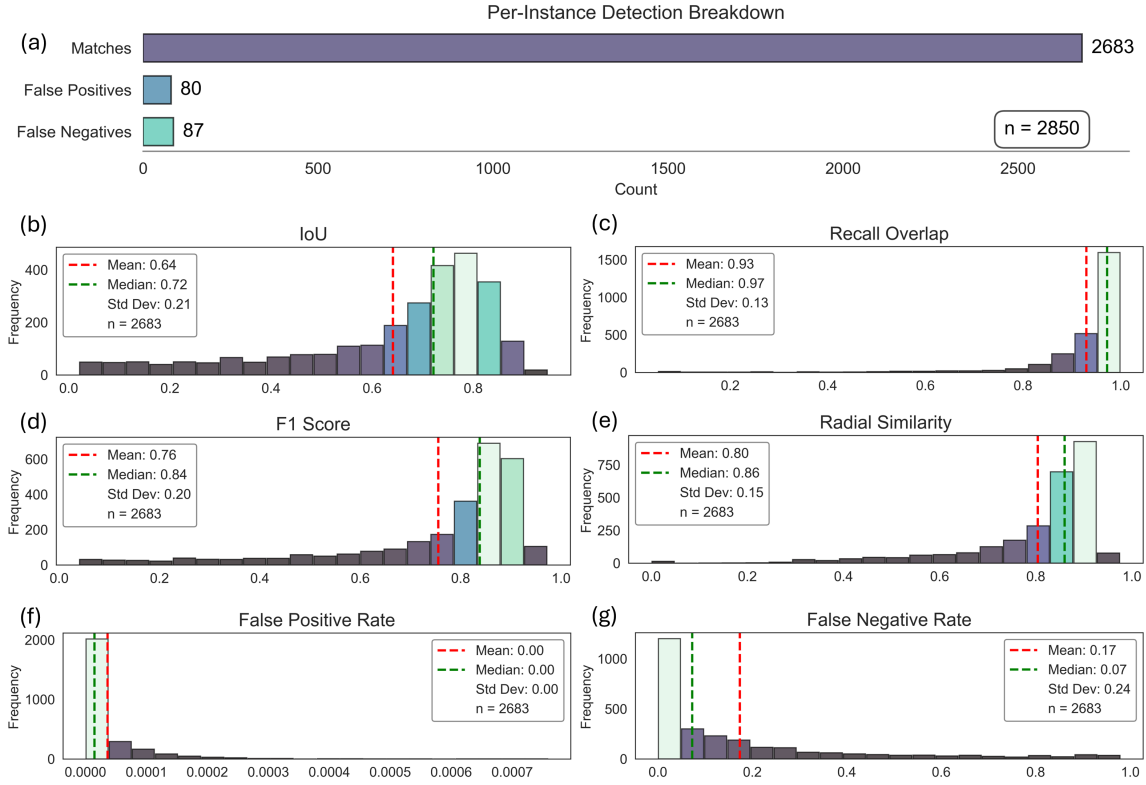
Figure 4.11: **Evaluation of BioPixel for 2D Podosome Segmentation.** (a) Summary of confusion matrix detection outcomes across all segmented and annotated podosome instances, including True Positives (Matches), False Positives, and False Negatives. (b-g) Metrics derived from the set of matched podosome pairs (n = 2683), where each predicted mask was successfully aligned with a corresponding ground truth annotation. (b) Distribution of Intersection over Union (IoU) scores, measuring pixel-wise overlap between predicted and ground truth masks. (c) Recall Overlap, assessing the extent to which predicted masks cover their corresponding ground truth objects. (d) F1 Score, balancing precision and recall across the matched dataset. (e) Radial Similarity, evaluating shape fidelity by comparing radial intensity profiles of segmented and ground truth podosomes. (f) False Positive Rate (FPR), defined as the proportion of predicted mask pixels not overlapping with the corresponding ground truth, calculated individually for each matched pair. (g) False Negative Rate (FNR), representing the proportion of ground truth podosome pixels not captured by the predicted mask, also computed per object pair. All metrics in subplots (b-g) reflect per-object, pixel-level comparisons within the matched set, offering fine-grained insight into segmentation accuracy and morphological consistency.

Finally, Radial Similarity, a custom metric designed to evaluate shape fidelity by comparing radial profiles of segmented and ground truth podosomes, returned a mean score of 0.80 and a median of 0.86, with a standard deviation of 0.15 (Fig. 4.11e). These values suggest that the segmented podosomes largely preserve expected radial symmetry and structural integrity, although deviations occur in more complex or asymmetric cases.

Taken together, these results demonstrate that the `PodosomeDetector` achieves strong performance in detecting and segmenting podosomes with high precision, minimal inclusion of background pixels, and good morphological consistency. While the model performs exceptionally well in terms of false positive control and overall shape fidelity, opportunities remain to improve sensitivity in capturing all ground truth pixels, especially in challenging imaging conditions.

5 Discussion

5.1 Drebrin subdomains

The molecular determinants responsible for the localization of drebrin to the podosome cap were identified through overexpression of constructs with different combinations of drebrin subdomains in primary macrophages. Experimental results showed that drebrin constructs without the ADFH region, like ΔADFH-GFP, and those lacking both the ADFH and PP regions, such as ΔADFH-ΔPP-GFP, maintained a cap-like localization at podosomes, similar to full-length drebrin. When the construct contained only CC and Hel regions, as in CC-Hel-GFP, it localized mainly to the podosome core, whereas constructs with only the PP and C-terminal regions (PP-C-term-GFP) or only the C-terminus (C-term-GFP) distributed throughout the cell in a dispersed manner. These findings suggest that the CC, Hel, and C-terminal regions are collectively essential for targeting drebrin to the podosomal cap, whereas the ADFH and PP regions appear nonessential for this specific localization in macrophages.

The observed localization patterns result from the specific functional interactions between drebrin's domains and the actin cytoskeleton. F-actin binding and bundling by the CC and Hel regions occur under regulation from the C-terminal region, which acts as an intramolecular inhibitor (also referred to as the blue box (BB) domain in Worth et al. (2013)). Without the C-terminal region, such as in CC-Hel-GFP, intrinsic inhibition disappears, resulting in constitutive F-actin binding and bundling. Despite the cap having bundled actin, CC-Hel-GFP likely accumulates in the podosome core, where the dynamic branched actin network supports binding. The core's dense, mechanically stressed actin filaments, which store elastic energy to produce protrusive forces (Jasnin et al., 2022), may provide a favorable environment for the unregulated actin-binding activity of CC-Hel. This could explain its core-preferential localization, as the constitutive binding of CC-Hel to the compressed filaments overrides its potential bundling function in the cap. Conversely, when constructs maintain the C-terminal region (ΔADFH-GFP, ΔADFH-ΔPP-GFP), they localize to the podosome cap, which surrounds the core (Linder and Cervero, 2020), indicating that the C-term prevents CC-Hel-mediated actin bundling to redirect drebrin away from the core. Cdk5-induced phosphorylation at S142 of drebrin's CC domain removes BB-mediated inhibition, to facilitate F-actin bundling and microtubule coupling through EB3 in neurons (Worth et al., 2013). This raises the possibility that the localization of drebrin at the cap of macrophage podosomes might similarly coordinate actin remodeling activities with microtubule-dependent processes, like endocytosis.

Drebrin's C-terminal region binds dynamin, likely contributing to integrin β1 endocytosis and cell migration (Yu et al., 2022). While the actin-binding domain of drebrin interacts with F-actin, its C-terminal region's interaction with dynamin may help localize drebrin to the podosome ring, a process that works alongside dynamin's established role in linking the actin cytoskeleton to podosomes (Ochoa et al., 2000) and its interaction with BAR-domain proteins during maturation of podosomes (Li et al., 2021). Without the CC and Hel domains, the PP-C-term-GFP and C-term-GFP constructs fail to localize properly, as observed in this study. This demonstrates that although dynamin binding occurs through the C-terminal domain, as shown by previous studies, this interaction alone is insufficient for cap localization without the actin-tethering capabilities provided by the CC and Hel domains.

The PP region in drebrin, which is essential for afadin binding and adherens junction stabilization in endothelial cells (Rehm et al., 2013), proves nonessential for localization to macrophage podosome caps, as demonstrated by the ΔADFH-ΔPP-GFP construct, which still localizes to the cap. The findings indicate that drebrin performs different functions in distinct cell types by changing its interactions according to the cell environment and the types of adhesion structures present. Macrophages exhibit podosome ring adhesion proteins like integrins which depend primarily on dynamin-mediated control rather than afadin which highlights the dominant role of the C-terminus over the PP region within this system.

Collectively, these experimental results demonstrate drebrin's podosome cap localization in macrophages depends on multiple factors including CC and Hel domains' F-actin binding capabilities, C-terminus regulation and potential stabilization through dynamin and microtubule interactions via EB3. This reveals drebrin as an essential controller of podosome cytoskeletal configuration.

5.2   Drebrin-EB3-Clathrin Axis

The proximity ligation assays from this study demonstrate that drebrin is in close spatial proximity to both EB3 and CHC at the podosome periphery. These findings hint at both a functional and spatial basis for the coordinated interaction occurring at this particular site. Additional unpublished work coming from the our lab has identified drebrin as a novel component of the podosome cap. In this context, drebrin was observed to localize more peripherally than α-actinin, supporting a model where actin filaments are crosslinked more centrally and peripheral bundling at the cap edge (Linder and Cervero, 2020). Drebrin-EB3 binding has been demonstrated in vitro and confirmed through proximity ligation assay in this study. Drebrin functions as a positive regulator of podosome-microtubule tip contacts as decreased numbers and frequencies of these contacts were observed after siRNA-mediated depletion of drebrin in macrophages. Immunoprecipitation from macrophage lysates demonstrated that drebrin co-precipitates with both EB3 and CHC, and its depletion resulted in increased surface levels of MT1-MMP and elevated extracellular matrix degradation. 3D confocal imaging demonstrated frequent associations between EEA1-positive early endosomes and podosomes. These combined results

support a model in which drebrin first interacts with clathrin during vesicle formation near the plasma membrane and subsequently engages with EB3 deeper in the cytoplasm to facilitate vesicle transfer onto the microtubule network (Fig. 5.1).

These observations align with and are contextualized by previous reports in the literature. Geraldo et al. (2008) demonstrated that drebrin binds specifically to EB3 but not EB1 as was confirmed via fluorescence resonance energy transfer (FRET) coupled with fluorescence lifetime imaging microscopy (FLIM) results in neuronal growth cones showing this interaction in situ. Worth et al. (2013) demonstrated that drebrin in neuronal growth cones links dynamic microtubules to F-actin in filopodia through its interaction with EB3, a mechanism critical for neuritogenesis and neuronal migration. This interaction has also been observed in epithelial systems, where Bazellières et al. (2012) showed that drebrin E forms a complex with EB3, myosin IIB, and βII-spectrin that couples microtubules to the apical F-actin network during epithelial cell morphogenesis. Alvarez-Suarez et al. (2021) additionally showed that drebrin localizes to postsynaptic podosomes in C2C12 myotubes, where it colocalizes with condensed F-actin, and that its depletion through siRNA-mediated knockdown or inhibition of its interaction with actin using BTP2 results in disorganized podosome-associated microtubules, as evidenced by a reduced number of EB3 foci underneath AChR clusters and decreased active actin-rich podosomes. Dominant-negative inhibition of the EB3-drebrin interaction in cerebellar granule neurons (CGNs) randomized motility and disrupted the transition to radial migration directions, demonstrating the specificity of this interaction and its critical role in linking microtubule movements to actomyosin dynamics during nucleokinesis and neuronal migration (Trivedi et al., 2017). Expression of EB3 truncation mutants (EB3M and EB3DeltaC) that disrupt the EB3-drebrin interaction decreased F-actin treadmilling and induced growth cone collapse, reinforcing the functional importance of this interaction in regulating cytoskeletal architecture and neuronal polarization (Zhao et al., 2017). Findings by Poobalasingam et al. (2022) showed that EB3, rather than EB1, is preferentially localized at microtubule plus-ends in filopodia, suggesting that EB3 may play a more prominent role in linking microtubules to actin-rich structures.

Further evidence relating to clathrin and endocytosis supports the proposed model. Wiesner et al. (2013) reported that depletion of Rab5a, a key regulator of early endosomes, increases surface levels of MT1-MMP, consistent with the observed effects of drebrin depletion. Yang et al. (2022) demonstrated that branched actin networks, similar to those observed in podosome cores, promote membrane invagination during clathrin-mediated endocytosis by exerting force at the edges of clathrin-coated structures (CCSs). These findings suggest that the mechanical principles underlying actin-driven membrane remodeling may also inform our understanding of podosome function, given their shared reliance on Arp2/3-dependent branched actin polymerization. Fernández-Barrera and Alonso (2018) on the other hand described a mechanism in which INF2 interacts with microtubules to promote tubulin acetyltransferase 1 (α-TAT1) expression via the actin-MRTF-SRF transcriptional circuit.

Altogether, the levied data from the proximity ligation assays support a model in which drebrin functions as a central hub that bridges clathrin-mediated endocytosis with intracellular transport along microtubules through its interaction with EB3. The evidence presented here integrates original experimental findings with broader literature in the field, positioning the drebrin-EB3-CHC axis as a key regulator of podosome organization and function and identifies podosomes as the preferred sites for clathrin-mediated endocytosis in macrophages (Fig. 5.1).
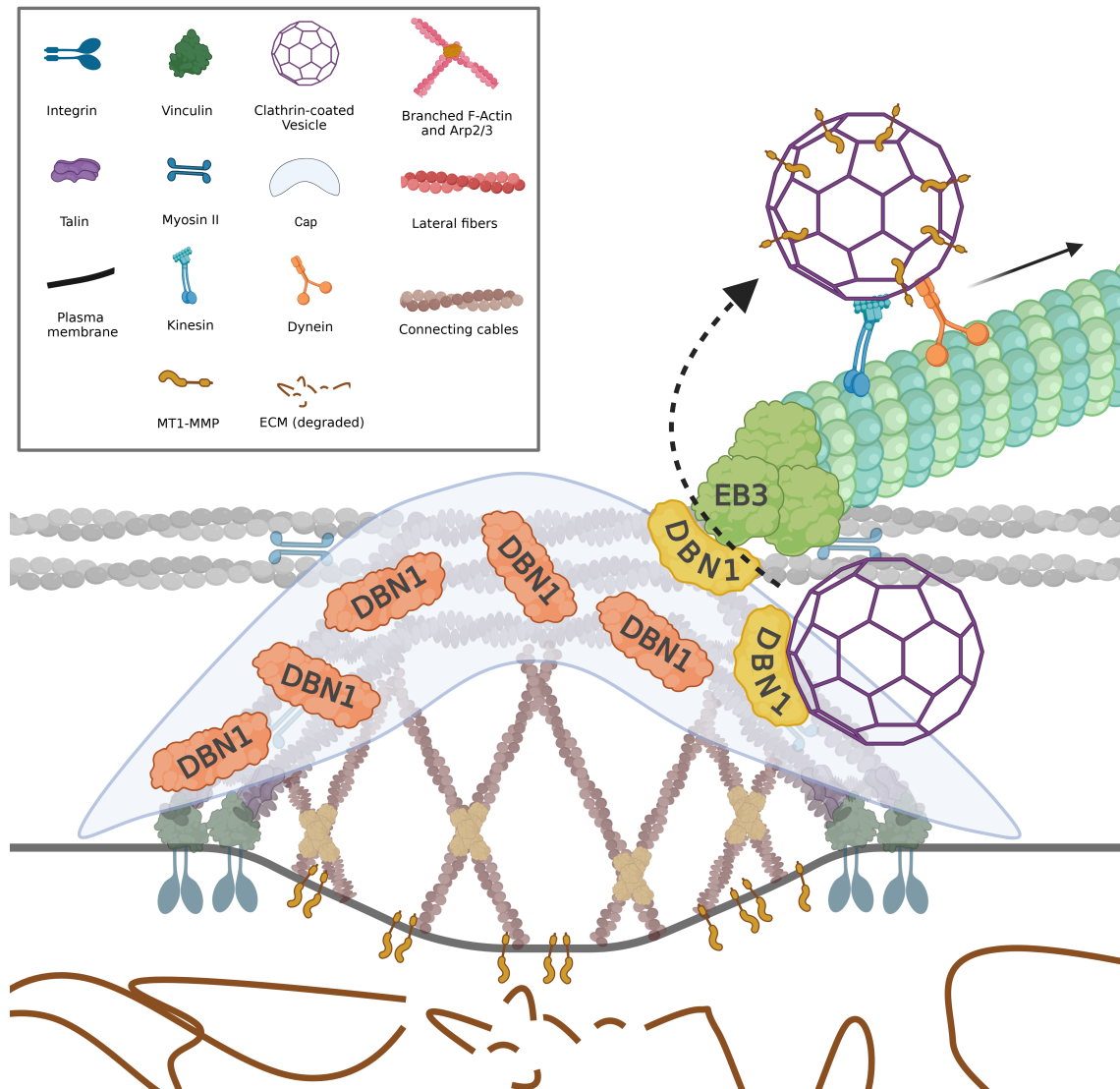
Figure 5.1: **Drebrin links clathrin-coated vesicles to EB3-tagged microtubules +tips at podosomes.** The model illustrates drebrin's dual role at the podosome cap periphery, where it interacts with EB3 at microtubule (+)-ends while associating with clathrin-coated vesicles. A proposed "on-ramp" mechanism shows drebrin facilitating vesicle transfer to microtubules via EB3, with kinesin/dynein motors enabling bidirectional transport. This spatial organization positions drebrin as a critical hub integrating endocytosis and microtubule-based trafficking in podosome regulation.

5.3   +TIP heterogeneity in macrophages

The connection between +TIP heterogeneity and endocytosis may be found in drebrin which functions as an actin-binding protein that interacts with EB3. Drebrin connects microtubule ends to actin filaments (Geraldo et al., 2008) which positions it as a potential key player in cytoskeletal regulation at points of endocytosis. Our laboratory's latest research results show that drebrin functions as a podosome cap protein at the actin-dense core of these adhesive structures. The function of podosomes as sites for matrix remodeling and endocytosis depends on coordinated interactions between actin and microtubules. Because drebrin connects EB3-decorated microtubules to actin structures in both podosomes and areas close to clathrin-coated pits it seems to function as an essential link for cytoskeletal coordination across multiple cellular processes. Direct evidence linking drebrin to clathrin-heavy chain 1 is still limited but its position near clathrin-coated pits and podosome caps shows it probably supports actin structure stabilization during vesicle formation and adhesion site turnover (Boulant et al., 2011). The observed EB3 and CLIP-170 heterogeneity may thus spatially segregate microtubules, with EB3-enriched tips associating with actin networks at podosomes, potentially through drebrin, while CLIP-170-decorated tips facilitate vesicle offloading at cortical sites.

CLIP-170 overexpression combined with EB3 immunostaining demonstrates diverse microtubule plus-end (+TIP) decoration, indicating that individual microtubules can be decorated by either CLIP-170, EB3, or both. This suggests distinct functional roles for different subsets of microtubules in endocytic regulation. The dynamic regulation of microtubule growth by +TIPs such as CLIP-170 and EB3 along with their uneven distribution across microtubule populations indicates that specific microtubule subsets might be selectively recruited for distinct cellular tasks. However, it is also conceivable that both endocytic and exocytic events may occur at the same +TIP, suggesting a potential convergence of trafficking pathways at shared microtubule sites. The observed variability aligns with models proposed by (Akhmanova and Steinmetz, 2008), who demonstrated that +TIPs form dynamic networks at microtubule plus ends, where their composition regulates microtubule dynamics, interactions with cellular structures, and force generation. This suggests that microtubule functional identity is defined by their +TIP "signature," enabling specialized roles in processes like vesicle transport. During clathrin-mediated endocytosis heterogeneity may specify microtubule function either as facilitating "on ramps" for vesicle transport or as "off ramps".

The unique composition of +TIP networks causes microtubule tip heterogeneity which leads to the creation of functionally separate subpopulations in different areas. Microtubule tips dominated by CLIP-170 that use liquid-liquid phase separation (LLPS) stabilization act as off-ramps, a term introduced in this thesis, while delivering cargo through cortical anchoring. Although the concept of these stabilizing structures is discussed in Miesch et al. (2023), the term "off-ramps" is newly introduced in this thesis. In contrast, EB3-enriched microtubule tips use dynamic LLPS condensates to serve as on-ramps that recruit cargo during transient microtubule growth. The compartmentalization of microtubule functions to organize transport mechanisms and coordinate cytoskeletal movements

(Gundersen, 2002) supports a system in which microtubule function is determined by +TIP composition.

EB3-mediated release of CLIP-170 from microtubule ends (Komarova et al., 2005) may serve to fine-tune microtubule dwell times at the cell cortex, thereby influencing processes such as cell polarization, migration, or vesicle delivery. The proportional regulation of these proteins could ensure dynamic microtubule-cortex interactions, allowing rapid adaptation to extracellular cues or mechanical forces. The experimental overexpression of CLIP-170 may extend these protein interactions while improving their connection to endocytic systems or actin networks related to podosomes. This aligns with the concept of "selective tracking", where +TIP composition determines microtubule interactions with cortical sites (Akhmanova and Hoogenraad, 2005). In endocytosis, selectivity ensures only microtubules with optimal +TIP profiles support vesicle trafficking, while others remain uninvolved or, in the context of podosomes, may instead stabilize adhesion structures.

Microtubule diversity created by +TIP variations creates a dynamic framework which enables spatial control over endocytosis and podosome function. By acting as "on ramps," certain microtubules may direct vesicles to specific regions or anchor podosomes, while "off ramps" prevent excessive vesicle fusion or podosome formation. As a podosome cap element Drebrin likely adjusts actin dynamics at points where microtubules transport cargo or maintain adhesion complexes. New research into the components of +TIPs during live-cell endocytic assays together with podosome activity studies will help determine the specific recruitment mechanisms for different microtubule types. Researching the regulation of +TIP heterogeneity by membrane tension and matrix stiffness might uncover the mechanisms behind cellular adaptation of endocytic capacity and invasive potential (Linder et al., 2011).

The distinct decoration patterns of microtubule plus-ends by CLIP-170 and EB3 offer an effective way to achieve functional variation across the microtubule network. Certain microtubule subsets develop specific functions that include actin coordination at podosomes and vesicle transport facilitation as well as cortical interaction mediation to enhance clathrin-mediated endocytosis and podosome-mediated matrix remodeling. The connection between drebrin and clathrin is complemented by drebrin's dual functionality as both a podosome cap protein and EB3 interactor which makes it a prime candidate for connecting microtubule diversity to these processes. Microtubule identity, mediated by +TIPs, directs cellular activities through precise spatial control, modeling cytoskeletal coordination in endocytosis and adhesion.

5.4   BioPixel Macrophage Detection Performance

The performance metrics of BioPixel show a strong macrophage detection capability with a mean IoU of 0.85 and a median IoU of 0.91. According to cell segmentation literature IoU scores exceeding 0.8 qualify as excellent, which supports these findings (Edlund et al., 2021). While IoU measures mask overlap, average precision (AP) evaluates detection performance across confidence thresholds. For instance, the LIVECell dataset shows overall segmentation AP scores between 47.8 and 47.9 percent while individual cell types reach AP

scores up to 64 to 66 percent. Models trained on LIVECell data surpass those trained on datasets like EVICAN by achieving AP scores between 36.7% and 59.6% while EVICAN models only achieve 24.6%. Although IoU and AP are not directly comparable, BioPixel's high IoU scores align with these benchmarks, demonstrating its competitiveness against leading segmentation and detection models.

The model demonstrates its effectiveness with a mean Recall Overlap of 0.96 and a median of 0.99, reflecting its ability to capture nearly all ground truth pixels while minimizing missed detections. The balanced performance between precision and recall is evident in the F1 Score which shows a mean of 0.90 and a median of 0.95. The measured F-measures equate to or exceed the F-measure results established within other cell segmentation research like cytoplasmic segmentation studies which report values between 0.89 and 0.94 (Wang et al., 2024).

BioPixel achieves high detection reliability through a minimal false positive rate (FPR) (mean 0.03, median 0.00) and a false negative rate (FNR) (mean 0.08, median 0.04) along with zero false positive (FP) and only five false negative (FN) among 75 masks. The results show no false detections while successfully identifying 70 macrophages with minimal misses. This performance outcome matches advanced segmentation techniques demonstrated in tracking studies which report high macrophage detection accuracy rates up to 97.5% (Park et al., 2023).

Boundary IoU was considered as an evaluation metric due to its increased sensitivity to boundary alignment errors compared to standard Mask IoU, particularly for large objects (Cheng et al., 2021). Boundary IoU emphasizes contour fidelity by measuring overlap only within a narrow band around predicted and ground truth boundaries, making it well-suited for detecting subtle boundary discrepancies that may be overlooked by global overlap metrics. In the specific application described, Boundary IoU yielded low scores (mean = 0.11, median = 0.04). This outcome is attributed to the irregular, dynamic morphologies of macrophages, which include pseudopodial extensions. In such cases, small contour shifts - even when the overall shape is preserved - can result in disproportionately low Boundary IoU scores, reducing its suitability for biologically meaningful interpretation. To address the limitations of strict boundary-based metrics, radial similarity was introduced as an alternative approach.

Radial similarity, which compares segmented objects to idealized radial profiles, offers a more robust measure of morphological fidelity in cells with ambiguous or flexible boundaries. BioPixel achieved a mean radial similarity of 0.82 (median = 0.95, SD = 0.22, n = 70), indicating strong consistency with expected macrophage shape characteristics. This approach aligns with findings by Chen and Murphy (2023), who argue that shape- and composition-based metrics provide a more appropriate assessment for segmentation of complex cell types, especially when precise edge delineation is biologically or technically unreliable.

Recent developments like the Boundary Difference over Union (DoU) Loss offer promising improvements in segmentation training by focusing on regional boundary accuracy rather than global overlap. Originally developed for medical image segmentation (Sun

et al., 2023), this approach calculates differences within localized boundary regions and can guide deep learning models to produce morphologically realistic boundaries — a potential path forward for improving segmentation accuracy in complex cell types like macrophages.

5.5 Advances in BioPixel Detection Over Poji

In addition to macrophage segmentation, BioPixel was evaluated for podosome detection, demonstrating similarly strong performance across key metrics.

The segmentation performance of the BioPixel algorithm demonstrates a high degree of accuracy in detecting podosomes, as evidenced by multiple evaluation metrics. The mean Intersection over Union (IoU) of 0.64, with a median of 0.72, indicates substantial spatial overlap between predicted and ground truth masks, suggesting that the model effectively captures the general location and extent of podosomes in both 2D and 3D. This performance surpasses the semi-automated approach of Poji (Herzog et al., 2020), which relies on user-defined parameters for podosome detection and lacks quantitative validation metrics such as IoU. While Poji offers flexibility in parameter adjustment, its dependence on manual tuning introduces subjectivity and variability, whereas BioPixel's automated pipeline ensures consistent and reproducible results across dimensions.

A Recall Overlap of 0.93 (median: 0.97) shows that BioPixel detects nearly all annotated podosomes, with minimal missed regions. This suggests that the algorithm rarely misses true podosome instances, a critical requirement for reliable downstream analysis.

The F1 Score achieved a mean of 0.76 and a median of 0.84. The False Positive Rate (FPR) was consistently zero across all samples, demonstrating that the algorithm produces negligible false positive detections under the current evaluation setup. This quantifiable and near-zero FPR underscores BioPixel's reliability in minimizing erroneous detections, a key advantage for downstream biological interpretation.

The False Negative Rate (FNR), with a mean of 0.17 and a median of 0.07, indicates that while some podosomes are not perfectly captured, the frequency of missed instances remains relatively low. Variability in this metric, reflected in a standard deviation of 0.24, may point to differences in podosome morphology or image quality across samples, warranting further investigation into specific failure cases. BioPixel's evaluation framework supports targeted improvements in such edge cases.

As in the macrophage detection evaluation, Radial Similarity was used to assess morphological fidelity in podosomes, where BioPixel achieved a mean score of 0.80 (median: 0.86). These results suggest that the segmented podosomes closely resemble the radial symmetry and structural characteristics of the ground truth annotations, indicating that the algorithm preserves important morphological features essential for biological interpretation.

While benchmarking was conducted in 2D due to annotation feasibility, the BioPixel algorithm is inherently designed for 3D segmentation, which is its primary advantage over Poji. Poji, while adaptable to multi-plane analysis, requires manual slice-by-slice adjustments and lacks integrated 3D segmentation capabilities. The BioPixel algorithm's native 3D processing ensures a more comprehensive and automated solution for volumetric

podosome analysis, eliminating the need for laborious manual interventions required by Poji.

From a technical standpoint, Poji's Fiji macro code, while functional, exhibits several critical limitations that hinder usability, reproducibility, and maintainability. Most notably, its variable naming is inconsistent, opaque, and often cryptic—using arbitrary abbreviations (e.g., 'aaa', 'bbb'), single-letter counters ('g', 'k'), and semantically ambiguous names (e.g., 'mul_Arr', 'scpi', 'resArray'). These choices obscure the code's logic and purpose, making it difficult for users to understand, debug, or modify. Coupled with minimal inline documentation, this naming scheme creates unnecessary cognitive overhead for researchers and developers. Additionally, Poji lacks automated error handling, standardized validation metrics, and clear modular separation of functions, increasing the likelihood of user error and limiting adaptability across datasets. In contrast, BioPixel leverages modern machine learning frameworks and follows standard software engineering practices that emphasize code readability, transparency, and reproducibility. Its fully automated architecture and quantifiable outputs make it more suitable for high-throughput and collaborative research environments.

In summary, the BioPixel algorithm achieves robust and morphologically accurate podosome segmentation with minimal false positives and strong recall, making it a superior tool for quantitative podosome analysis in both 2D and 3D fluorescence microscopy images. Its automated pipeline, validated by comprehensive metrics, outperforms Poji in consistency, objectivity, and scalability. While Poji remains a useful tool for exploratory or legacy applications, its dependence on manual intervention, lack of quantitative benchmarking, and poor code maintainability underscore the advantages of adopting the BioPixel algorithm for modern, reproducible podosome research.

5.6 Conclusion

This thesis has established BioPixel as an effective tool for segmenting and detecting macrophages and podosomes, with a mean IoU of 0.85 for macrophages and 0.64 for podosomes, performing reliably across 2D and 3D datasets. The algorithm's automated approach and consistent outputs improve upon tools like Poji, particularly for scalability in research settings. Biologically, the work has clarified drebrin's involvement in podosome organization, showing that its CC, Hel, and C-terminal domains are critical for cap localization, while its interactions with EB3 and clathrin connect endocytosis to microtubule dynamics. The study of +TIP heterogeneity suggests that specialized microtubule subsets may support distinct cellular functions. Future work could refine BioPixel by exploring additional computational enhancements or applying it to other imaging types, expanding its utility in cell biology.

This work has advanced the understanding of podosome dynamics by combining biological insights with computational approaches. The investigation into drebrin-EB3-clathrin interactions has shed light on podosome function, while BioPixel has provided a consistent method for examining cellular structures. Together, these efforts enhance our ability to explore complex cellular processes, with BioPixel improving such analyses.

6 Safety and waste disposal

6.1 Biosafety level 2

All authorized personnel were instructed on the hazards and conduct to be observed in the laboratory area prior to commencing work in the S2 area and at annual intervals thereafter, and whenever new biological agents and processes were introduced. The time and content of the instruction were documented by signature. All individuals authorized to enter the laboratory were subjected to an examination by UKE's company physician prior to commencing work and at annual intervals thereafter, along with an examination at the end of employment, in accordance with the regulations of the Employer's Liability Insurance Association G42 (risk of infection) and G43 (genetic engineering work). Immunization against hepatitis B virus was offered free of charge.

In the laboratory area, eating, drinking, chewing gum, smoking, applying cosmetics, and storing food or beverages were prohibited. Pipetting was performed exclusively with pipetting aids. The use of laboratory equipment which could inflict injury (glass, needles, scalpels) was reduced to a necessary minimum. Used needles were not placed back into the plastic protective sleeves, bent or kinked (recapping rule).

Lab coats were only worn in the S1 and S2 laboratories, where they were mandatory. Upon leaving the laboratory area, lab coats were taken off and hung up in the hallway wardrobe. Disposable gloves were worn when handling infectious or hazardous materials. They were not worn when using common equipment, such as when using the telephone. Gloves were removed when leaving the S2 area.

Work with infectious or potentially infectious materials particularly ones that may generate aerosols (e.g., pipetting, transferring and mixing liquids, opening vessels that are under positive or negative pressure) was performed in Class II safety workbenches. Operating instructions posted around the workbenches were followed. To ensure functional airflow, only equipment and materials necessary for the current task were present within the workbench. Air suction gaps at the work window and rear wall were not covered. Open flames (gas burners or such) were not used here. Materials and equipment used in the workbenches were either autoclaved after use or their surfaces were disinfected by wiping with e.g. 70 % ethanol before removal from the workbench. Upon finishing work, the work bench surface and any tools remaining under the work bench (e.g., pipetting aid) were disinfected and the UV light of the work bench was activated.

Disinfection was carried out in accordance with the recommendations of the Federal Health Office (BGA), or the Robert Koch Institute (RKI), and the German Society for Hygiene and Microbiology (DGHM).

Waste that may be contaminated with infectious materials or GMO's was disposed of only after sterilization (autoclaving for 20 minutes at 121 °C for liquid waste, 134 °C for solid waste). All waste containing DNA/RNA was also autoclaved. The autoclaves were operated only by properly instructed staff. Closed containers were used for temporary storage and transport to autoclaving in the scullery. If there was a risk that the containers were contaminated on their outer surface during loading, they were immediately wiped with inactivation solution. After sterilization, the waste was considered biologically safe and was disposed of according to UKE waste guidelines. Sharp or pointed disposable items made of metal or glass, e.g., scalpels and needles, were collected immediately after use in special containers designed to prevent perforation and autoclaved along with solid, combustible waste. Used needles were not pulled off the syringe, bent off or put back into the plastic protective covers (recapping rule). Liquid waste was collected in sealable and autoclavable plastic containers (max. 1000 mL capacity). Containers were filled only up to 80 % of their maximum capacity. Containers with liquid waste were temporarily stored in solid, closed containers. During transport to the autoclaves, care was taken to ensure that liquids would not leak. Methanol, formaldehyde or other organic solvents are not permitted to be autoclaved and were disposed of separately.

6.2   Safety notes and disposal of hazardous substances

Table 6.1: Safety notes and disposal of hazardous substances.

Chemical	H[1] statements	P[2] statements	GHS[3]	Disposal
2-Propanol	H225 - H319 - H336	P210 - P233 - P240 - P241 - P242 - P305 + P351 + P338		Collected separately
EDTA	H319	P305 + P351 + P338		Autoclave waste
Kanamycin sulfate	H360	P201 - P202 - P280 - P308 + P313		Autoclave waste
Methanol	H225 - H301 + H311 + H331 - H370	P210 - P233 - P280 - P301 + P310 - P303 + P361 + P353 - P304 + P340 + P311		Collected separately
Paraformaldehyde	H228 - H302 + H332 - H315 - H317 - H318 - H335 - H341 - H350	P202 - P210 - P270 - P280 - P305 + P351 + P338 - P308 + P313		Collected separately
Triton X 100	H302 - H318 - H411	P270 - P273 - P280 - P305 + P351 + P338 - P310		Collected separately

[1]Hazard [2]Precautionary [3]Globally Harmonized System of Classification and Labelling of Chemicals

7   Use of AI Declaration

This dissertation was conducted in accordance with the guidelines for the use of generative AI systems (gKI) as outlined by the University of Hamburg (latest available version: January 2024, applicable through May 2025). AI tools were employed in a **strictly auxiliary and selective capacity**, primarily for technical, organizational, and coding assistance. At no point was AI used in a manner that replaced original intellectual contributions, and all AI-assisted outputs were critically reviewed, edited, and validated before inclusion in this work.

Specifically, the following AI tools were utilized in an assisted and controlled manner:

- **Literature Assistance (Limited Use, Manually Verified):**

  - **Notebook LM (Google)** was used *in a supplementary capacity* to identify potentially relevant literature that might have been overlooked in traditional searches (e.g., PubMed, Google Scholar). All sources were independently verified to ensure reliability and accuracy.

  - **ChatGPT (GPT-4 Turbo)** was occasionally used to *clarify complex scientific concepts* encountered in the literature. Any insights gained were critically assessed against peer-reviewed sources before integration.

- **Technical and Formatting Assistance (Strictly for Efficiency, No Content Generation):**

  - **ChatGPT (GPT-4 Turbo)** was used *for LaTeX syntax automation* to assist in formatting tasks efficiently.

  - **Gemini 2.0 (Google)** assisted in *converting citations into BibTeX entries*, ensuring accuracy and consistency.

  - **Deepseek R1** was employed *to verify compliance with coding standards* (PEP257 for docstrings, PEP8 for formatting).

- **Programming and Code Assistance (Selective and Supervised Use, No Blind Automation):**

  - **ChatGPT (GPT-4 Turbo)** was used in a *limited and controlled manner* to assist in drafting Python functions and refining complex implementations.

All AI-generated code was manually reviewed, adjusted, and validated before inclusion.

– **GitHub Copilot and Cody** were used in tandem for *AI-assisted autocompletion* of code lines and boilerplate structures (e.g., loops, function scaffolding). Only code that was logically sound and fit the specific requirements was accepted; no suggestions were blindly incorporated.

• **Writing Support (Minimal Assistance for Clarity and Structure, No Automated Text Generation):**

– As a native English speaker, I authored all content independently. AI tools were used in a *limited capacity* to refine academic tone, improve stylistic consistency, and enhance clarity, in line with scholarly writing standards.

– At no point was AI used to **generate substantial portions of text or develop original arguments**. All AI-assisted refinements were critically assessed and manually adapted to maintain scientific accuracy and coherence.

No AI tools were used in:

• **Experimental design, execution, or data interpretation.**

• **The core scientific analysis of results.**

• **Generating novel insights or drawing conclusions.**

Scientific writing and programming inherently require precision, and while AI-assisted tools were used in a *strictly supportive role*, every decision, analysis, and interpretation in this dissertation was made independently. AI served as an **efficiency-enhancing aid rather than a creative or analytical substitute**. The final manuscript represents my own intellectual contribution, with AI playing a minor, supervised role in select aspects of formatting, literature navigation, and coding assistance.

All AI involvement was in full compliance with the university's guidelines on **good scientific practice and transparency**. This approach reflects a responsible and balanced integration of modern tools into academic research while ensuring the highest standards of originality, integrity, and rigor.

Bibliography

J. Abramson, J. Adler, J. Dunger, and et al. Accurate structure prediction of biomolecular interactions with alphafold 3. *Nature*, 630(8019):493–500, jun 2024. doi: 10.1038/s41586-024-07487-w.

A. Akhmanova and C. Hoogenraad. Microtubule plus-end-tracking proteins: mechanisms and functions. *Current Opinion in Cell Biology*, 17(1):47–54, feb 2005. doi: 10.1016/j.ceb.2004.11.001.

A. Akhmanova and M. Steinmetz. Tracking the ends: a dynamic protein network controls the fate of microtubule tips. *Nature Reviews Molecular Cell Biology*, 9(4):309–322, apr 2008. doi: 10.1038/nrm2369.

A. Akhmanova and M. Steinmetz. Microtubule +tips at a glance. *Journal of Cell Science*, 123(Pt 20):3415–3419, 2010. doi: 10.1242/jcs.062414.

K. Alblazi and C. Siar. Cellular protrusions–lamellipodia, filopodia, invadopodia and podosomes–and their roles in progression of orofacial tumours: current understanding. *Asian Pacific Journal of Cancer Prevention*, 16(6):2187–2191, 2015. doi: 10.7314/apjcp.2015.16.6.2187.

P. Alvarez-Suarez, N. Nowak, A. Protasiuk-Filipunas, H. Yamazaki, T. Prószyński, and M. Gawor. Drebrin regulates acetylcholine receptor clustering and organization of microtubules at the postsynaptic machinery. *International Journal of Molecular Sciences*, 22(17):9387, aug 2021. doi: 10.3390/ijms22179387.

M. Amyere, B. Payrastre, U. Krause, P. Van Der Smissen, A. Veithen, and P. Courtoy. Constitutive macropinocytosis in oncogene-transformed fibroblasts depends on sequential permanent activation of phosphoinositide 3-kinase and phospholipase c. *Molecular Biology of the Cell*, 11(10):3453–3467, oct 2000. doi: 10.1091/mbc.11.10.3453.

J. Andersen, J. Thomsen, E. Overgaard, C. Lassen, L. Brandt, I. Vilstrup, A. Kryger, and S. Mikkelsen. Computer use and carpal tunnel syndrome: a 1-year follow-up study. *JAMA*, 289(22):2963–2969, jun 2003. doi: 10.1001/jama.289.22.2963.

C. Antonescu, F. Aguet, G. Danuser, and S. Schmid. Phosphatidylinositol-(4,5)-bisphosphate regulates clathrin-coated pit initiation, stabilization, and size. *Molecular Biology of the Cell*, 22(14):2588–2600, jul 2011. doi: 10.1091/mbc.E11-04-0362.

C. Antonescu, T. McGraw, and A. Klip. Reciprocal regulation of endocytosis and metabolism. *Cold Spring Harbor Perspectives in Biology*, 6(7):a016964, jul 2014. doi: 10.1101/cshperspect.a016964.

J. Arens, T. Duong, and L. Dehmelt. A morphometric screen identifies specific roles for microtubule-regulating genes in neuronal development of p19 stem cells. *PLoS ONE*, 8 (11):e79796, 2013. doi: 10.1371/journal.pone.0079796.

W. Arthur and K. Burridge. Rhoa inactivation by p190rhogap regulates cell spreading and migration by promoting membrane protrusion and polarity. *Molecular Biology of the Cell*, 12(9):2711–2720, 2001. doi: 10.1091/mbc.12.9.2711.

H. Bachimanchi and G. Volpe. Diffusion models for super-resolution microscopy: a tutorial. *Journal of Physics: Photonics*, 7(1):013001, jan 2025. ISSN 2515-7647. doi: 10.1088/2515-7647/ada101. URL http://dx.doi.org/10.1088/2515-7647/ada101.

M. Baldassarre, A. Pompeo, G. Beznoussenko, C. Castaldi, S. Cortellino, M. McNiven, A. Luini, and R. Buccione. Dynamin participates in focal extracellular matrix degradation by invasive cells. *Molecular Biology of the Cell*, 14(3):1074–1084, 2003. doi: 10.1091/mbc.e02-05-0308.

A. Bayati, R. Kumar, V. Francis, and P. McPherson. Sars-cov-2 infects cells after viral entry via clathrin-mediated endocytosis. *Journal of Biological Chemistry*, 296:100306, 2021. doi: 10.1016/j.jbc.2021.100306.

E. Bazellières, D. Massey-Harroche, M. Barthélémy-Requin, F. Richard, J. Arsanto, and A. Le Bivic. Apico-basal elongation requires a drebrin-e-eb3 complex in columnar human epithelial cells. *Journal of Cell Science*, 125(4):919–931, feb 2012. doi: 10.1242/jcs.092676.

M. E. Berginski, S. M. Gomez, and J. E. Bear. Automated analysis of invadopodia dynamics in live cells. *PeerJ*, 2:e462, 2014. doi: 10.7717/peerj.462.

R. Bhuwania, S. Cornfine, Z. Fang, M. Krüger, E. J. Luna, and S. Linder. Supervillin couples myosin-dependent contractility to podosomes and enables their turnover. *Journal of Cell Science*, 125(9):2300–2314, 2012. doi: 10.1242/jcs.100032.

B. Blouw, D. Seals, I. Pass, B. Diaz, and S. Courtneidge. A role for the podosome/invadopodia scaffold protein tks5 in tumor growth in vivo. *European Journal of Cell Biology*, 87:555–567, 2008. doi: 10.1016/j.ejcb.2008.02.008.

B. Bouchet and A. Akhmanova. Microtubules in 3d cell motility. *Journal of Cell Science*, 130(1):39–50, 2017. doi: 10.1242/jcs.189431.

S. Boulant, C. Kural, J. Zeeh, F. Ubelmann, and T. Kirchhausen. Actin dynamics counteract membrane tension during clathrin-mediated endocytosis. *Nature Cell Biology*, 13 (9):1124–1131, aug 2011. doi: 10.1038/ncb2307.

B. Bugyi and M. Kellermayer. The discovery of actin: "to see what everyone else has seen, and to think what nobody has thought". *Journal of Muscle Research and Cell Motility*, 41(1):3–9, 2020. doi: 10.1007/s10974-019-09515-z.

G. Burgstaller and M. Gimona. Actin cytoskeleton remodelling via local inhibition of contractility at discrete microdomains. *Journal of Cell Science*, 117(2):223–231, 2004. doi: 10.1242/jcs.00839.

G. Burgstaller and M. Gimona. Podosome-mediated matrix resorption and cell motility in vascular smooth muscle cells. *American Journal of Physiology-Heart and Circulatory Physiology*, 288(6):H3001–H3005, 2005. doi: 10.1152/ajpheart.01002.2004.

S. Burns, A. J. Thrasher, M. P. Blundell, L. Machesky, and G. E. Jones. Configuration of human dendritic cell cytoskeleton by rho gtpases, the was protein, and differentiation. *Blood*, 98(4):1142–1149, 2001. doi: 10.1182/blood.V98.4.1142.

Y. Calle, N. O. Carragher, A. J. Thrasher, and G. E. Jones. Inhibition of calpain stabilises podosomes and impairs dendritic cell motility. *Journal of Cell Science*, 119(11):2375–2385, 2006. doi: 10.1242/jcs.02939.

M. Caplow and J. Shanks. Evidence that a single monolayer tubulin-gtp cap is both necessary and sufficient to stabilize microtubules. *Molecular Biology of the Cell*, 7(4):663–675, 1996. doi: 10.1091/mbc.7.4.663.

B. M. Carlson. *The Human Body*. Academic Press, 2019. ISBN 9780128042540. doi: 10.1016/B978-0-12-804254-0.00001-6.

E. Caron and A. Hall. Identification of two distinct mechanisms of phagocytosis controlled by different rho gtpases. *Science*, 282(5394):1717–1721, nov 1998. doi: 10.1126/science.282.5394.1717.

P. Cervero, L. Panzer, and S. Linder. Podosome reformation in macrophages: Assays and analysis. In A. S. Coutts, editor, *Adhesion Protein Protocols*, pages 97–120. Springer, 2013. doi: 10.1007/978-1-62703-538-5_6.

P. Cervero, C. Wiesner, A. Bouissou, R. Poincloux, and S. Linder. Lymphocyte-specific protein 1 regulates mechanosensory oscillation of podosomes and actin isoform-based actomyosin symmetry breaking. *Nature Communications*, 9(1):515, 2018. doi: 10.1038/s41467-018-02904-x.

A. Chabadel, I. Bañon-Rodríguez, D. Cluet, B. Rudkin, B. Wehrle-Haller, E. Genot, P. Jurdic, I. Anton, and F. Saltel. Cd44 and beta3 integrin organize two functionally distinct actin-based domains in osteoclasts. *Molecular Biology of the Cell*, 18(12):4899–4910, 2007. doi: 10.1091/mbc.e07-04-0378.

M. Chalfie and J. Thomson. Organization of neuronal microtubules in the nematode caenorhabditis elegans. *The Journal of Cell Biology*, 82(1):278–289, 1979. doi: 10.1083/jcb.82.1.278.

H. Chen and R. Murphy. Evaluation of cell segmentation methods without reference segmentations. *Molecular Biology of the Cell*, 34(6):ar50, may 2023. doi: 10.1091/mbc.E22-08-0364.

W. Chen. Proteolytic activity of specialized surface protrusions formed at rosette contact sites of transformed cells. *Journal of Experimental Zoology*, 251(2):167–185, 1989. doi: 10.1002/jez.1402510206.

B. Cheng, R. Girshick, P. Dollár, A. C. Berg, and A. Kirillov. Boundary iou: Improving object-centric image segmentation evaluation, 2021. URL https://arxiv.org/abs/2103.16562.

O. Collin, P. Tracqui, A. Stephanou, Y. Usson, J. Clément-Lacroix, and E. Planus. Spatiotemporal dynamics of actin-rich adhesion microdomains: influence of substrate flexibility. *Journal of Cell Science*, 119(9):1914–1925, 2006. doi: 10.1242/jcs.02838.

G. M. Cooper. *The Cell: A Molecular Approach*. Sinauer Associates, 2nd edition, 2000. ISBN 0-87893-106-6.

K. Cutler, C. Stringer, T. Lo, L. Rappez, N. Stroustrup, S. Brook Peterson, P. Wiggins, and J. Mougous. Omnipose: a high-precision morphology-independent solution for bacterial cell segmentation. *Nature Methods*, 19(11):1438–1448, nov 2022. doi: 10.1038/s41592-022-01639-4.

O. Daumke, A. Roux, and V. Haucke. Bar domain scaffolds in dynamin-mediated membrane fission. *Cell*, 156(5):882–892, feb 2014. doi: 10.1016/j.cell.2014.02.017.

T. David-Pfeuty and S. J. Singer. Altered distributions of the cytoskeletal proteins vinculin and alpha-actinin in cultured fibroblasts transformed by rous sarcoma virus. *Proceedings of the National Academy of Sciences of the United States of America*, 77:6687–6691, 1980.

A. deCathelineau and P. Henson. The final step in programmed cell death: phagocytes carry apoptotic cells to the grave. *Essays in Biochemistry*, 39:105–117, 2003. doi: 10.1042/bse0390105.

A. DePina and G. Langford. Vesicle transport: the role of actin filaments and myosin motors. *Microscopy Research and Technique*, 47(2):93–106, 1999. doi: 10.1002/(SICI)1097-0029(19991015)47:2⟨93::AID-JEMT2⟩3.0.CO;2-P.

A. Desai and T. Mitchison. Microtubule polymerization dynamics. *Annual Review of Cell and Developmental Biology*, 13:83–117, 1997. doi: 10.1146/annurev.cellbio.13.1.83.

O. Destaing, F. Saltel, J.-C. Géminard, P. Jurdic, and F. Bard. Podosomes display actin turnover and dynamic self-organization in osteoclasts expressing actin-green fluorescent protein. *Molecular Biology of the Cell*, 14(2):407–416, 2003. doi: 10.1091/mbc.e02-07-0389.

P. Di Benedetto, P. Ruscitti, Z. Vadasz, E. Toubi, and R. Giacomelli. Macrophages with regulatory functions, a possible new therapeutic perspective in autoimmune diseases. *Autoimmunity Reviews*, 18(10):102369, 2019. doi: 10.1016/j.autrev.2019.102369.

B. Diaz et al. Tks5-dependent, nox-mediated generation of reactive oxygen species is necessary for invadopodia formation. *Science Signaling*, 2:ra53, 2009. doi: 10.1126/scisignal.2000368.

G. Doherty and H. McMahon. Mechanisms of endocytosis. *Annual Review of Biochemistry*, 78:857–902, 2009. doi: 10.1146/annurev.biochem.78.081307.110540.

R. Dong, K. Cwynarski, A. Entwistle, F. Marelli-Berg, F. Dazzi, E. Simpson, J. M. Goldman, J. V. Melo, R. I. Lechler, I. Bellantuono, A. Ridley, and G. Lombardi. Dendritic cells from cml patients have altered actin organization, reduced antigen processing, and impaired migration. *Blood*, 101(9):3560–3567, 2003. doi: 10.1182/blood-2002-06-1841.

C. Edlund, T. Jackson, N. Khalid, N. Bevan, T. Dale, A. Dengel, S. Ahmed, J. Trygg, and R. Sjogren. Livecell-a large-scale dataset for label-free live cell segmentation. *Nature Methods*, 18(9):1038–1045, sep 2021. doi: 10.1038/s41592-021-01249-6.

J. Evans, I. Correia, O. Krasavina, N. Watson, and P. Matsudaira. Macrophage podosomes assemble at the leading lamella by growth and fragmentation. *Journal of Cell Biology*, 161(4):697–705, 2003. doi: 10.1083/jcb.200212037.

J. Fernández-Barrera and M. Alonso. Coordination of microtubule acetylation and the actin cytoskeleton by formins. *Cellular and Molecular Life Sciences*, 75(17):3181–3191, sep 2018. doi: 10.1007/s00018-018-2855-3.

D. Fletcher and R. Mullins. Cell mechanics and the cytoskeleton. *Nature*, 463(7280): 485–492, 2010. doi: 10.1038/nature08908.

M. Ford, I. Mills, B. Peter, Y. Vallis, G. Praefcke, P. Evans, and H. McMahon. Curvature of clathrin-coated pits driven by epsin. *Nature*, 419(6905):361–366, sep 2002. doi: 10.1038/nature01020.

E. Frixione. Recurring views on the structure and function of the cytoskeleton: a 300-year epic. *Cell Motility and the Cytoskeleton*, 46(2):73–94, 2000. doi: 10.1002/1097-0169(200006)46:2⟨73::AID-CM1⟩3.0.CO;2-0.

G. Gaidano, L. Bergui, M. Schena, M. Gaboli, O. Cremona, P. Marchisio, and F. Caligaris-Cappio. Integrin distribution and cytoskeleton organization in normal and malignant monocytes. *Leukemia*, 4:682–687, 1990.

W. Gao, J. Liu, M. Liu, Y. Yao, Z. Liu, L. Liu, H. He, and H. Zhou. Macrophage 3d migration: A potential therapeutic target for inflammation and deleterious progression in diseases. *Pharmacological Research*, 167:105563, 2021. doi: 10.1016/j.phrs.2021.105563.

M. I. García Arguinzonis. *Analysis of signal transduction pathways and the cytoskeleton in VASP-deficient cell lines and mouse models.* Doctoral thesis, Universität Würzburg, Fakultät für Biologie, Würzburg, 2003. URN: urn:nbn:de:bvb:20-opus-6195.

C. Garnham, A. Vemu, E. Wilson-Kubalek, I. Yu, A. Szyk, G. Lander, R. Milligan, and A. Roll-Mecak. Multivalent microtubule recognition by tubulin tyrosine ligase-like family glutamylases. *Cell*, 161(5):1112–1123, 2015. doi: 10.1016/j.cell.2015.04.003.

C. Gawden-Bone, Z. Zhou, E. King, A. Prescott, C. Watts, and J. Lucocq. Dendritic cell podosomes are protrusive and invade the extracellular matrix using metalloproteinase mmp-14. *Journal of Cell Science*, 123:1427–1437, 2010. doi: 10.1242/jcs.056515.

A. Gennerich and R. Vale. Walking the walk: how kinesin and dynein coordinate their steps. *Current Opinion in Cell Biology*, 21(1):59–67, 2009. doi: 10.1016/j.ceb.2008.12.002.

S. Geraldo, U. Khanzada, M. Parsons, J. Chilton, and P. Gordon-Weeks. Targeting of the f-actin-binding protein drebrin by the microtubule plus-tip protein eb3 is required for neuritogenesis. *Nature Cell Biology*, 10(10):1181–1189, oct 2008. doi: 10.1038/ncb1778.

M. Gimona, K. Djinovic-Carugo, W. Kranewitter, and S. Winder. Functional plasticity of ch domains. *FEBS Letters*, 513(1):98–106, 2002. doi: 10.1016/s0014-5793(01)03240-9.

M. Gimona, I. Kaverina, G. Resch, E. Vignal, and G. Burgstaller. Calponin repeats regulate actin filament stability and formation of podosomes in smooth muscle cells. *Molecular Biology of the Cell*, 14(6):2482–2491, 2003. doi: 10.1091/mbc.e02-11-0743.

F. Ginhoux and M. Guilliams. Tissue-resident macrophage ontogeny and homeostasis. *Immunity*, 44(3):439–449, 2016. doi: 10.1016/j.immuni.2016.02.024.

O. Glebov, N. Bright, and B. Nichols. Flotillin-1 defines a clathrin-independent endocytic pathway in mammalian cells. *Nature Cell Biology*, 8(1):46–54, jan 2006. doi: 10.1038/ncb1342.

B. Goode and M. Eck. Mechanism and function of formins in the control of actin assembly. *Annual Review of Biochemistry*, 76:593–627, 2007. doi: 10.1146/annurev.biochem.75.103004.142647.

Z. Gu, J. Kordowska, G. Williams, C. Wang, and C. Hai. Erk1/2 mapk and caldesmon differentially regulate podosome dynamics in a7r5 vascular smooth muscle cells. *Experimental Cell Research*, 313(5):849–866, 2007. doi: 10.1016/j.yexcr.2006.12.005.

G. G. Gundersen. Microtubule capture: Iqgap and clip-170 expand the repertoire. *Current Biology*, 12(19):R645–R647, 2002. doi: 10.1016/S0960-9822(02)01156-9.

B. Guo, Y. Qi, H. Wu, R. Zha, L. Wang, X. Zhang, and W. Huang. Nanosensor quantitative monitoring of ros/rns homeostasis in single phagolysosomes of macrophages during bactericidal processes. *Chemical Communications (Cambridge)*, 61(1):97–100, 2024. doi: 10.1039/d4cc05423g.

S. Heasman and A. Ridley. Mammalian rho gtpases: new insights into their functions from in vivo studies. *Nature Reviews Molecular Cell Biology*, 9(9):690–701, 2008. doi: 10.1038/nrm2476.

W. Henne, E. Boucrot, M. Meinecke, E. Evergren, Y. Vallis, R. Mittal, and H. McMahon. Fcho proteins are nucleators of clathrin-mediated endocytosis. *Science*, 328(5983):1281–1284, jun 2010. doi: 10.1126/science.1188462.

H. Henrie, D. Bakhos-Douaihy, I. Cantaloube, A. Pilon, M. Talantikite, V. Stoppin-Mellet, A. Baillet, C. Poüs, and B. Benoit. Stress-induced phosphorylation of clip-170 by jnk promotes microtubule rescue. *The Journal of Cell Biology*, 219(7):e201909093, 2020. doi: 10.1083/jcb.201909093.

D. Herb, M. Trenti, M. Mantela, C. Simserides, J. Ankerhold, and M. Rossini. Quantumdna: A python package for analyzing quantum charge dynamics in dna and exploring its biological relevance, 2025. URL https://arxiv.org/abs/2502.06883.

H. Herrmann, H. Bär, L. Kreplak, S. Strelkov, and U. Aebi. Intermediate filaments: from cell architecture to nanomechanics. *Nature Reviews Molecular Cell Biology*, 8(7): 562–573, 2007. doi: 10.1038/nrm2197.

R. Herzog, K. van den Dries, P. Cervero, and S. Linder. Poji: a fiji-based tool for analysis of podosomes and associated proteins. *Journal of Cell Science*, 133:jcs238964, 2020. doi: 10.1242/jcs.238964.

A. Heydarabadipour and H. M. Sauro. Alias4sbml: A python package for generating alias nodes in sbml models, 2025. URL https://arxiv.org/abs/2502.11318.

T. Hohl, A. Rivera, L. Lipuma, A. Gallegos, C. Shi, M. Mack, and E. Pamer. Inflammatory monocytes facilitate adaptive cd4 t cell responses during respiratory fungal infection. *Cell Host & Microbe*, 6(5):470–481, 2009. doi: 10.1016/j.chom.2009.10.007.

F. Huber, A. Boire, M. López, and G. Koenderink. Cytoskeletal crosstalk: when three different personalities team up. *Current Opinion in Cell Biology*, 32:39–47, 2015. doi: 10.1016/j.ceb.2014.10.005.

D. Hume. The mononuclear phagocyte system. *Current Opinion in Immunology*, 18(1): 49–53, 2006. doi: 10.1016/j.coi.2005.11.008.

N. Hundt, M. Preller, O. Swolski, A. Ang, H. Mannherz, D. Manstein, and M. Müller. Molecular mechanisms of disease-related human β-actin mutations p.r183w and p.e364k. *The FEBS Journal*, 281(23):5279–5291, 2014. doi: 10.1111/febs.13068.

Y. Inoue, N. Tanaka, Y. Tanaka, S. Inoue, K. Morita, M. Zhuang, T. Hattori, and K. Sugamura. Clathrin-dependent entry of severe acute respiratory syndrome coronavirus into target cells expressing ace2 with the cytoplasmic tail deleted. *Journal of Virology*, 81 (16):8722–8729, aug 2007. doi: 10.1128/JVI.00253-07.

H. Ishikawa, R. Bischoff, and H. Holtzer. Mitosis and intermediate-sized filaments in developing skeletal muscle. *The Journal of Cell Biology*, 38(3):538–555, 1968. doi: 10.1083/jcb.38.3.538.

M. Jasnin, J. Hervy, S. Balor, A. Bouissou, A. Proag, R. Voituriez, J. Schneider, T. Mangeat, I. Maridonneau-Parini, W. Baumeister, S. Dmitrieff, and R. Poincloux. Elasticity of podosome actin networks produces nanonewton protrusive forces. *Nature Communications*, 13(1):3842, jul 2022. doi: 10.1038/s41467-022-30652-6.

M. Johansson and et al. Eosinophils adhere to vascular cell adhesion molecule-1 via podosomes. *American Journal of Respiratory Cell and Molecular Biology*, 31:413–422, 2004.

B. Joosten, M. Willemse, J. Fransen, A. Cambi, and K. van den Dries. Super- resolution correlative light and electron microscopy (sr-clem) reveals novel ultrastructural insights into dendritic cell podosomes. *Frontiers in Immunology*, 9:1908, 2018. doi: 10.3389/ fimmu.2018.01908.

J. Jumper, R. Evans, A. Pritzel, and et al. Highly accurate protein structure prediction with alphafold. *Nature*, 596(7873):583–589, aug 2021. doi: 10.1038/s41586-021-03819-2.

M. Kaksonen and A. Roux. Mechanisms of clathrin-mediated endocytosis. *Nature Reviews Molecular Cell Biology*, 19(5):313–326, may 2018. doi: 10.1038/nrm.2017.132.

N. Kaul, V. Soppina, and K. Verhey. Effects of α-tubulin k40 acetylation and detyrosination on kinesin-1 motility in a purified system. *Biophysical Journal*, 106(12):2636–2643, 2014. doi: 10.1016/j.bpj.2014.05.008.

B. Kelly, S. Graham, N. Liska, P. Dannhauser, S. Höning, E. Ungewickell, and D. Owen. Clathrin adaptors. ap2 controls clathrin polymerization with a membrane-activated switch. *Science*, 345(6195):459–463, jul 2014. doi: 10.1126/science.1254836.

S. Khaitlina. Tropomyosin as a regulator of actin dynamics. *International Review of Cell and Molecular Biology*, 318:255–291, 2015. doi: 10.1016/bs.ircmb.2015.06.002.

J. Kollman, J. Polka, A. Zelter, T. Davis, and D. Agard. Microtubule nucleating gamma-tusc assembles structures with 13-fold microtubule-like symmetry. *Nature*, 466(7308): 879–882, 2010. doi: 10.1038/nature09207.

Y. Komarova, G. Lansbergen, N. Galjart, F. Grosveld, G. Borisy, and A. Akhmanova. Eb1 and eb3 control clip dissociation from the ends of growing microtubules. *Molecular Biology of the Cell*, 16(11):5334–5345, nov 2005. doi: 10.1091/mbc.e05-07-0614.

Y. Komarova, C. De Groot, I. Grigoriev, S. Gouveia, E. Munteanu, J. Schober, S. Honnappa, R. Buey, C. Hoogenraad, M. Dogterom, G. Borisy, M. Steinmetz, and A. Akhmanova. Mammalian end binding proteins control persistent microtubule growth. *The Journal of Cell Biology*, 184(5):691–706, 2009. doi: 10.1083/jcb.200807179.

P. Kopp, R. Lammers, M. Aepfelbacher, G. Woehlke, T. Rudel, N. Machuy, W. Steffen, and S. Linder. The kinesin kif1c and microtubule plus ends regulate podosome dynamics in macrophages. *Molecular Biology of the Cell*, 17(6):2811–2823, 2006. doi: 10.1091/mbc.e05-11-1010.

E. Korn. Actin polymerization and its regulation by proteins from nonmuscle cells. *Physiological Reviews*, 62(2):672–737, 1982. doi: 10.1152/physrev.1982.62.2.672.

S. Kühn and M. Geyer. Formins as effector proteins of rho gtpases. *Small GTPases*, 5: e29513, 2014. doi: 10.4161/sgtp.29513.

A. Labernadie, A. Bouissou, P. Delobelle, S. Balor, R. Voituriez, A. Proag, I. Fourquaux, C. Thibault, C. Vieu, R. Poincloux, G. Charrière, and I. Maridonneau-Parini. Protrusion force microscopy reveals oscillatory force generation and mechanosensing activity of human macrophage podosomes. *Nature Communications*, 5:5343, 2014. doi: 10.1038/ncomms6343.

G. Lansbergen, I. Grigoriev, Y. Mimori-Kiyosue, T. Ohtsuka, S. Higa, I. Kitajima, J. Demmers, N. Galjart, A. Houtsmuller, F. Grosveld, and A. Akhmanova. Clasps attach microtubule plus ends to the cell cortex through a complex with ll5beta. *Developmental Cell*, 11(1):21–32, 2006. doi: 10.1016/j.devcel.2006.05.012.

O. Larbolette, B. Wollscheid, J. Schweikert, P. Nielsen, and J. Wienands. Sh3p7 is a cytoskeleton adapter protein and is coupled to signal transduction from lymphocyte antigen receptors. *Molecular and Cellular Biology*, 19(2):1539–1546, feb 1999. doi: 10.1128/MCB.19.2.1539.

E. Lawrence and M. Zanic. Rescuing microtubules from the brink of catastrophe: Clasps lead the way. *Current Opinion in Cell Biology*, 56:94–101, 2019. doi: 10.1016/j.ceb.2018.10.011.

E. Lawrence, S. Chatterjee, and M. Zanic. More is different: Reconstituting complexity in microtubule regulation. *Journal of Biological Chemistry*, 299(12):105398, 2023. doi: 10.1016/j.jbc.2023.105398.

M. Ledbetter and K. Porter. A "microtubule" in plant cell fine structure. *The Journal of Cell Biology*, 19(1):239–250, 1963. doi: 10.1083/jcb.19.1.239.

V. Lehto, T. Hovi, T. Vartio, R. Badley, and I. Virtanen. Reorganization of cytoskeletal and contractile elements during transition of human monocytes into adherent macrophages. *Laboratory Investigation*, 47(4):391–399, 1982.

J. Li, K. Fujise, H. Wint, Y. Senju, S. Suetsugu, H. Yamada, K. Takei, and T. Takeda. Dynamin 2 and bar domain protein pacsin 2 cooperatively regulate formation and maturation of podosomes. *Biochemical and Biophysical Research Communications*, 571: 145–151, sep 2021. doi: 10.1016/j.bbrc.2021.07.041.

S. Linder and P. Cervero. The podosome cap: past, present, perspective. *European Journal of Cell Biology*, 99(5):151087, jun 2020. doi: 10.1016/j.ejcb.2020.151087.

S. Linder, D. Nelson, M. Weiss, and M. Aepfelbacher. Wiskott-aldrich syndrome protein regulates podosomes in primary human macrophages. *Proceedings of the National Academy of Sciences*, 96(17):9648–9653, 1999. doi: 10.1073/pnas.96.17.9648.

S. Linder, H. Higgs, K. Hüfner, K. Schwarz, U. Pannicke, and M. Aepfelbacher. The polarization defect of wiskott-aldrich syndrome macrophages is linked to dislocalization of the arp2/3 complex. *Journal of Immunology*, 165(1):221–225, 2000a. doi: 10.4049/jimmunol.165.1.221.

S. Linder, K. Hufner, U. Wintergerst, and M. Aepfelbacher. Microtubule-dependent formation of podosomal adhesion structures in primary human macrophages. *Journal of Cell Science*, 113(23):4165–4176, 2000b. doi: 10.1242/jcs.113.23.4165.

S. Linder, C. Wiesner, and M. Himmel. Degrading devices: Invadosomes in proteolytic cell invasion. *Annual Review of Cell and Developmental Biology*, 27:185–211, 2011. doi: 10.1146/annurev-cellbio-092910-154216.

H. Lodish, A. Berk, C. Kaiser, M. Krieger, M. Scott, A. Bretscher, and et al. *Molecular Cell Biology*. W. H. Freeman and Company, New York, 6th edition, 2007.

H. Lodish, A. Berk, C. Kaiser, M. Krieger, A. Bretscher, H. Ploegh, and et al. *Cell Organization and Movement I: Microfilaments*. W.H. Freeman, eighth edition, 2016. ISBN 978-1-4641-8339-3.

J. Lohr, P. Stojanov, M. Lawrence, D. Auclair, B. Chapuy, C. Sougnez, P. Cruz-Gordillo, B. Knoechel, Y. Asmann, S. Slager, A. Novak, A. Dogan, S. Ansell, B. Link, L. Zou, J. Gould, G. Saksena, N. Stransky, C. Rangel-Escareño, J. Fernandez-Lopez, A. Hidalgo-Miranda, J. Melendez-Zajgla, E. Hernández-Lemus, A. Schwarz-Cruz y Celis, I. Imaz-Rosshandler, A. Ojesina, J. Jung, C. Pedamallu, E. Lander, T. Habermann, J. Cerhan, M. Shipp, G. Getz, and T. Golub. Discovery and prioritization of somatic mutations in diffuse large b-cell lymphoma (dlbcl) by whole-exome sequencing. *Proceedings of the National Academy of Sciences*, 109(10):3879–3884, 2012. doi: 10.1073/pnas.1121343109.

A. Lomakin, I. Semenova, I. Zaliapin, P. Kraikivski, E. Nadezhdina, B. Slepchenko, A. Akhmanova, and V. Rodionov. Clip-170-dependent capture of membrane organelles by microtubules initiates minus-end directed transport. *Developmental Cell*, 17(3):323–333, 2009. doi: 10.1016/j.devcel.2009.07.010.

Y. Lu, C. Liu, Y. Xu, H. Cheng, S. Shi, C. Wu, and X. Yu. Stathmin destabilizing microtubule dynamics promotes malignant potential in cancer cells by epithelial-mesenchymal transition. *Hepatobiliary Pancreatic Diseases International*, 13(4):386–394, 2014. doi: 10.1016/s1499-3872(14)60038-2.

A. Mantovani, A. Sica, and M. Locati. Macrophage polarization comes of age. *Immunity*, 23(4):344–346, 2005. doi: 10.1016/j.immuni.2005.10.001.

R. Massol, W. Boll, A. Griffin, and T. Kirchhausen. A burst of auxilin recruitment determines the onset of clathrin-coated vesicle uncoating. *Proceedings of the National Academy of Sciences of the United States of America*, 103(27):10265–10270, jul 2006. doi: 10.1073/pnas.0603369103.

R. May, E. Caron, A. Hall, and L. Machesky. Involvement of the arp2/3 complex in phagocytosis mediated by fcgammar or cr3. *Nature Cell Biology*, 2(4):246–248, apr 2000. doi: 10.1038/35008673.

S. Mayor, R. Parton, and J. Donaldson. Clathrin-independent pathways of endocytosis. *Cold Spring Harbor Perspectives in Biology*, 6(6):a016758, jun 2014. doi: 10.1101/cshperspect.a016758.

M. McKinley, V. D. O'Loughlin, E. Pennefather-O'Brien, and R. Harris. *Human Anatomy*. McGraw Hill Education, 4th edition, 2015. ISBN 978-0-07-352573-0.

B. McMichael, P. Kotadiya, T. Singh, L. Holliday, and B. Lee. Tropomyosin isoforms localize to distinct microfilament populations in osteoclasts. *Bone*, 39(4):694–705, 2006. doi: 10.1016/j.bone.2006.04.031.

F. McNally and R. Vale. Identification of katanin, an atpase that severs and disassembles stable microtubules. *Cell*, 75(3):419–429, 1993. doi: 10.1016/0092-8674(93)90377-3.

M. B. M. Meddens, B. Rieger, C. G. Figdor, A. Cambi, and K. van den Dries. Automated podosome identification and characterization in fluorescence microscopy images. *Microscopy and Microanalysis*, 19(1):180–189, 2013. doi: 10.1017/S1431927612014018.

J. Mercer, M. Schelhaas, and A. Helenius. Virus entry by endocytosis. *Annual Review of Biochemistry*, 79:803–833, 2010. doi: 10.1146/annurev-biochem-060208-104626.

E. Metchnikoff. Untersuchungen ueber die mesodermalen phagocyten einiger wirbeltiere. *Biologisches Centralblatt*, 3:560–565, 1883.

J. Miesch, R. T. Wimbish, M.-C. Velluz, and C. Aumeier. Phase separation of +tip networks regulates microtubule dynamics. *PNAS*, 120(35):e2301457120, 2023. doi: 10.1073/pnas.2301457120.

A. Miller. The contractile ring. *Current Biology*, 21(24):R976–R978, 2011. doi: 10.1016/j.cub.2011.10.044.

Y. Mimori-Kiyosue, N. Shiina, and S. Tsukita. The dynamic behavior of the apc-binding protein eb1 on the distal ends of microtubules. *Current Biology*, 10(14):865–868, 2000. doi: 10.1016/s0960-9822(00)00600-x.

T. Mitchison and M. Kirschner. Dynamic instability of microtubule growth. *Nature*, 312 (5991):237–242, 1984. doi: 10.1038/312237a0.

A. Miyauchi and et al. Osteoclast cytosolic calcium, regulated by voltage-gated calcium channels and extracellular calcium, controls podosome assembly and bone resorption. *Journal of Cell Biology*, 111(6):2543–2552, 1990. doi: 10.1083/jcb.111.6.2543.

K. Mizutani and et al. Essential role of neural wiskott-aldrich syndrome protein in podosome formation and degradation of extracellular matrix in src-transformed fibroblasts. *Cancer Research*, 62:669–674, 2002.

V. Moreau, F. Tatin, C. Varon, and E. Génot. Actin can reorganize into podosomes in aortic endothelial cells, a process controlled by cdc42 and rhoa. *Molecular and Cellular Biology*, 23(19):6809–6822, 2003. doi: 10.1128/MCB.23.19.6809-6822.2003.

D. Mosser and J. Edwards. Exploring the full spectrum of macrophage activation. *Nature Reviews Immunology*, 8(12):958–969, 2008. doi: 10.1038/nri2448.

S. Mostowy and P. Cossart. Septins: the fourth component of the cytoskeleton. *Nature Reviews Molecular Cell Biology*, 13(3):183–194, feb 2012. doi: 10.1038/nrm3284.

R. Mullins, J. Heuser, and T. Pollard. The interaction of arp2/3 complex with actin: nucleation, high affinity pointed end capping, and formation of branching networks of filaments. *Proceedings of the National Academy of Sciences*, 95(11):6181–6186, 1998. doi: 10.1073/pnas.95.11.6181.

D. A. Murphy and S. A. Courtneidge. The 'ins' and 'outs' of podosomes and invadopodia: Characteristics, formation and function. *Nature Reviews Molecular Cell Biology*, 12(7): 413–426, 2011. doi: 10.1038/nrm3141.

P. J. Murray and T. A. Wynn. Protective and pathogenic functions of macrophage subsets. *Nature Reviews Immunology*, 11(11):723–737, 2011. doi: 10.1038/nri3073.

H. Nakahara and et al. Transmembrane/cytoplasmic domain-mediated membrane type 1-matrix metalloprotease docking to invadopodia is required for cell invasion. *Proceedings of the National Academy of Sciences of the United States of America*, 94(15):7959–7964, 1997. doi: 10.1073/pnas.94.15.7959.

C. Niessen. Tight junctions/adherens junctions: basic structure and function. *Journal of Investigative Dermatology*, 127(11):2525–2532, 2007. doi: 10.1038/sj.jid.5700865.

K. Nishida, K. Matsumura, M. Tamura, T. Nakamichi, K. Shimamori, M. Kuragano, A. Kabir, A. Kakugo, S. Kotani, N. Nishishita, and K. Tokuraku. Effects of three microtubule-associated proteins (map2, map4, and tau) on microtubules' physical properties and neurite morphology. *Scientific Reports*, 13(1):8870, 2023. doi: 10.1038/s41598-023-36073-9.

E. Nogales and H. Wang. Structural mechanisms underlying nucleotide-dependent self-assembly of tubulin and its relatives. *Current Opinion in Structural Biology*, 16(2): 221–229, 2006. doi: 10.1016/j.sbi.2006.03.005.

G. Ochoa, V. Slepnev, L. Neff, N. Ringstad, K. Takei, L. Daniell, W. Kim, H. Cao, M. McNiven, R. Baron, and P. De Camilli. A functional link between dynamin and the actin cytoskeleton at podosomes. *Journal of Cell Biology*, 150(2):377–389, jul 2000. doi: 10.1083/jcb.150.2.377.

T. Oikawa, T. Itoh, and T. Takenawa. Sequential signals toward podosome formation in nih-src cells. *Journal of Cell Biology*, 182:157–169, 2008. doi: 10.1083/jcb.200801042.

T. Oikawa, M. Oyama, H. Kozuka-Hata, S. Uehara, N. Udagawa, H. Saya, and K. Matsuo. Tks5-dependent formation of circumferential podosomes/invadopodia mediates cell-cell fusion. *Journal of Cell Biology*, 197(4):553–568, may 2012. doi: 10.1083/jcb.201111116.

M. Pachitariu and C. Stringer. Cellpose 2.0: how to train your own model. *Nature Methods*, 19(12):1634–1641, dec 2022. doi: 10.1038/s41592-022-01663-4.

K. Pal, Y. Zhao, Y. Wang, and X. Wang. Ubiquitous membrane-bound dnase activity in podosomes and invadopodia. *Journal of Cell Biology*, 220(7):e202008079, 2021. doi: 10.1083/jcb.202008079.

Y. Pan, Y. Yu, X. Wang, and T. Zhang. Tumor-associated macrophages in tumor immunity. *Frontiers in Immunology*, 11:583084, 2020. doi: 10.3389/fimmu.2020.583084.

L. Panzer, L. Trube, M. Klose, B. Joosten, J. Slotman, A. Cambi, and S. Linder. The formins fhod1 and inf2 regulate inter- and intra-structural contractility of podosomes. *Journal of Cell Science*, 129:298–313, 2016. doi: 10.1242/jcs.177691.

S. Park, T. Sipka, Z. Krivá, G. Lutfalla, M. Nguyen-Chi, and K. Mikula. Segmentation-based tracking of macrophages in 2d+ time microscopy movies inside a living animal. *Computers in Biology and Medicine*, 153:106499, feb 2023. doi: 10.1016/j.compbiomed.2022.106499.

R. Parton and K. Simons. The multiple faces of caveolae. *Nature Reviews Molecular Cell Biology*, 8(3):185–194, mar 2007. doi: 10.1038/nrm2122.

C. Pathak, F. Vaidya, B. Waghela, P. Jaiswara, V. Gupta, A. Kumar, B. Rajendran, and K. Ranjan. Insights of endocytosis signaling in health and disease. *International Journal of Molecular Sciences*, 24(3):2971, feb 2023. doi: 10.3390/ijms24032971.

W. Peitsch, I. Hofmann, J. Bulkescher, M. Hergt, H. Spring, U. Bleyl, S. Goerdt, and W. Franke. Drebrin, an actin-binding, cell-type characteristic protein: induction and localization in epithelial skin tumors and cultured keratinocytes. *Journal of Investigative Dermatology*, 125(4):761–774, oct 2005. doi: 10.1111/j.0022-202X.2005.23793.x.

R. Pelham and F. Chang. Actin dynamics in the contractile ring during cytokinesis in fission yeast. *Nature*, 419(6902):82–86, 2002. doi: 10.1038/nature00999.

T. Pollard and G. Borisy. Cellular motility driven by assembly and disassembly of actin filaments. *Cell*, 112(4):453–465, 2003. doi: 10.1016/s0092-8674(03)00120-x.

T. Poobalasingam, F. Bianco, F. Oozeer, and P. Gordon-Weeks. The drebrin/eb3 pathway regulates cytoskeletal dynamics to drive neuritogenesis in embryonic cortical neurons. *Journal of Neurochemistry*, 160(2):185–202, jan 2022. doi: 10.1111/jnc.15502.

L. Pradeau-Phélut and S. Etienne-Manneville. Cytoskeletal crosstalk: A focus on intermediate filaments. *Current Opinion in Cell Biology*, 87:102325, 2024. doi: 10.1016/j.ceb.2024.102325.

G. Praefcke and H. McMahon. The dynamin superfamily: universal membrane tubulation and fission molecules? *Nature Reviews Molecular Cell Biology*, 5(2):133–147, feb 2004. doi: 10.1038/nrm1313.

A. Proag, A. Bouissou, T. Mangeat, R. Voituriez, P. Delobelle, C. Thibault, C. Vieu, I. Maridonneau-Parini, and R. Poincloux. Working together: spatial synchrony in the force and actin dynamics of podosome first neighbors. *ACS Nano*, 9(4):3800–3813, 2015. doi: 10.1021/nn506745r.

A. Proag, A. Bouissou, C. Vieu, I. Maridonneau-Parini, and R. Poincloux. Evaluation of the force and spatial dynamics of macrophage podosomes by multi-particle tracking. *Methods*, 94:75–84, feb 2016. doi: 10.1016/j.ymeth.2015.09.002.

V. Procaccio, G. Salazar, S. Ono, M. Styers, M. Gearing, A. Davila, R. Jimenez, J. Juncos, C. Gutekunst, G. Meroni, B. Fontanella, E. Sontag, J. Sontag, V. Faundez, and B. Wainer. A mutation of beta -actin that alters depolymerization dynamics is associated with autosomal dominant developmental malformations, deafness, and dystonia. *The American Journal of Human Genetics*, 78(6):947–960, 2006. doi: 10.1086/504271.

T. Proszynski, J. Gingras, G. Valdez, K. Krzewski, and J. Sanes. Podosomes are present in a postsynaptic apparatus and participate in its maturation. *Proceedings of the National Academy of Sciences of the United States of America*, 106(43):18373–18378, oct 2009. doi: 10.1073/pnas.0910391106.

E.-H. Quezada, M.-K. Arthikala, and K. Nanjareddy. Cytoskeleton in abiotic stress signaling. In G. Santoyo, A. Kumar, M. Aamir, and S. Uthandi, editors, *Mitigation of Plant Abiotic Stress by Microorganisms*, pages 347–371. Academic Press, 2022. ISBN 9780323905688. doi: 10.1016/B978-0-323-90568-8.00016-X.

N. Rafiq, G. Grenci, C. Lim, M. Kozlov, G. Jones, V. Viasnoff, and A. Bershadsky. Forces and constraints controlling podosome assembly and disassembly. *Philosophical Transactions of the Royal Society B: Biological Sciences*, 374(1779):20180228, 2019. doi: 10.1098/rstb.2018.0228.

A. Rasheed and K. Rayner. Macrophage responses to environmental stimuli during homeostasis and disease. *Endocrine Reviews*, 42(4):407–435, 2021. doi: 10.1210/endrev/bnab004.

K. Rehm, L. Panzer, V. van Vliet, E. Genot, and S. Linder. Drebrin preserves endothelial integrity by stabilizing nectin at adherens junctions. *Journal of Cell Science*, 126(16):3756–3769, aug 2013. doi: 10.1242/jcs.129437.

N. Resnik, A. Erman, P. Veranič, and et al. Triple labelling of actin filaments, intermediate filaments and microtubules for broad application in cell biology: uncovering the

cytoskeletal composition in tunneling nanotubes. *Histochemistry and Cell Biology*, 152: 311–317, 2019. doi: 10.1007/s00418-019-01806-3.

A. Roll-Mecak. The tubulin code in microtubule dynamics and information encoding. *Developmental Cell*, 54(1):7–20, 2020. ISSN 1534-5807. doi: 10.1016/j.devcel.2020.06.008.

H. Schachtner and et al. Megakaryocytes assemble podosomes that degrade matrix and protrude through basement membrane. *Blood*, 121:2542–2552, 2013.

D. Seals et al. The adaptor protein tks5/fish is required for podosome formation and function, and for the protease-driven invasion of cancer cells. *Cancer Cell*, 7:155–165, 2005. doi: 10.1016/j.ccr.2005.01.006.

A. Sica and A. Mantovani. Macrophage plasticity and polarization: in vivo veritas. *Journal of Clinical Investigation*, 122(3):787–795, 2012. doi: 10.1172/JCI59643.

S. Sigismund, S. Confalonieri, A. Ciliberto, S. Polo, G. Scita, and P. Di Fiore. Endocytosis and signaling: cell logistics shape the eukaryotic cell plan. *Physiological Reviews*, 92(1): 273–366, jan 2012. doi: 10.1152/physrev.00005.2011.

V. Soppina, J. Herbstman, G. Skiniotis, and K. Verhey. Luminal localization of α-tubulin k40 acetylation by cryo-em analysis of fab-labeled microtubules. *PLoS ONE*, 7(10): e48204, 2012. doi: 10.1371/journal.pone.0048204.

A. Sorkin. Cargo recognition during clathrin-mediated endocytosis: a team effort. *Current Opinion in Cell Biology*, 16(4):392–399, aug 2004. doi: 10.1016/j.ceb.2004.06.001.

L. Spinardi, J. Rietdorf, L. Nitsch, M. Bono, C. Tacchetti, M. Way, and P. Marchisio. A dynamic podosome-like structure of epithelial cells. *Experimental Cell Research*, 295: 360–374, 2004. doi: 10.1016/j.yexcr.2004.01.014.

P. Spuul, T. Daubon, B. Pitter, F. Alonso, I. Fremaux, I. Kramer, E. Montanez, and E. Génot. Vegf-a/notch-induced podosomes proteolyse basement membrane collagen-iv during retinal sprouting angiogenesis. *Cell Reports*, 17(2):484–500, oct 2016. doi: 10.1016/j.celrep.2016.09.016.

T. Stepanova, I. Smal, J. van Haren, U. Akinci, Z. Liu, M. Miedema, R. Limpens, M. van Ham, M. van der Reijden, R. Poot, F. Grosveld, M. Mommaas, E. Meijering, and N. Galjart. History-dependent catastrophes regulate axonal microtubule behavior. *Current Biology*, 20(11):1023–1028, 2010. ISSN 0960-9822. doi: 10.1016/j.cub.2010.04.024.

F. Straub and G. Feuer. Adenosinetriphosphate the functional group of actin. *Biochimica et Biophysica Acta*, 4:455–470, 1950. ISSN 0006-3002. doi: 10.1016/0006-3002(50)90052-7.

C. Stringer and M. Pachitariu. Cellpose3: one-click image restoration for improved cellular segmentation. *Nature Methods*, feb 2025. doi: 10.1038/s41592-025-02595-5.

C. Stringer, T. Wang, M. Michaelos, and M. Pachitariu. Cellpose: a generalist algorithm for cellular segmentation. *Nature Methods*, 18(1):100–106, jan 2021. doi: 10.1038/s41592-020-01018-x.

H. Sui and K. Downing. Structural basis of interprotofilament interaction and lateral deformation of microtubules. *Structure*, 18(8):1022–1031, aug 2010. doi: 10.1016/j.str.2010.05.010.

F. Sun, Z. Luo, and S. Li. Boundary difference over union loss for medical image segmentation, 2023. URL https://arxiv.org/abs/2308.00220.

H. Sun, M. Yamamoto, M. Mejillano, and H. Yin. Gelsolin, a multifunctional actin regulatory protein. *Journal of Biological Chemistry*, 274(47):33179–33182, 1999. doi: 10.1074/jbc.274.47.33179.

J. Swanson. Shaping cups into phagosomes and macropinosomes. *Nature Reviews Molecular Cell Biology*, 9(8):639–649, 2008. doi: 10.1038/nrm2447.

G. Tarone, D. Cirillo, F. G. Giancotti, P. M. Comoglio, and P. C. Marchisio. Rous sarcoma virus-transformed fibroblasts adhere primarily at discrete protrusions of the ventral membrane called podosomes. *Experimental Cell Research*, 159:141–157, 1985.

A. I. Tauber. Metchnikoff and the phagocytosis theory. *Nature Reviews Molecular Cell Biology*, 4(11):897–901, 2003. doi: 10.1038/nrm1244.

S. Tehrani, R. Faccio, I. Chandrasekar, F. Ross, and J. Cooper. Cortactin has an essential and specific role in osteoclast actin assembly. *Molecular Biology of the Cell*, 17:2882–2895, 2006. doi: 10.1091/mbc.e06-03-0187.

N. Trivedi, D. Stabley, B. Cain, D. Howell, C. Laumonnerie, J. Ramahi, J. Temirov, R. Kerekes, P. Gordon-Weeks, and D. Solecki. Drebrin-mediated microtubule-actomyosin coupling steers cerebellar granule neuron nucleokinesis and migration pathway selection. *Nature Communications*, 8:14484, feb 2017. doi: 10.1038/ncomms14484.

I. Van Audenhove, N. Debeuf, C. Boucherie, and J. Gettemans. Fascin actin bundling controls podosome turnover and disassembly while cortactin is involved in podosome assembly by its sh3 domain in thp-1 macrophages and dendritic cells. *Biochimica et Biophysica Acta (BBA) - Molecular Cell Research*, 1853(5):940–952, 2015. doi: 10.1016/j.bbamcr.2015.01.003.

D. van de Willige, C. Hoogenraad, and A. Akhmanova. Microtubule plus-end tracking proteins in neuronal development. *Cellular and Molecular Life Sciences*, 73(10):2053–2077, 2016. doi: 10.1007/s00018-016-2168-3.

K. van den Dries, L. Nahidiazar, J. Slotman, M. Meddens, E. Pandzic, B. Joosten, M. Ansems, J. Schouwstra, A. Meijer, R. Steen, M. Wijers, J. Fransen, A. Houtsmuller, P. Wiseman, K. Jalink, and A. Cambi. Modular actin nano-architecture enables podosome protrusion and mechanosensing. *Nature Communications*, 10:5171, 2019. doi: 10.1038/s41467-019-13079-4.

E. van Goethem, R. Poincloux, F. Gauffre, I. Maridonneau-Parini, and V. Le Cabec. Matrix architecture dictates three-dimensional migration modes of human macrophages: differential involvement of proteases and podosome-like structures. *Journal of Immunology*, 184(2):1049–1061, 2010. doi: 10.4049/jimmunol.0902223.

J. van Haren and T. Wittmann. Microtubule plus end dynamics - do we know how microtubules grow?: Cells boost microtubule growth by promoting distinct structural transitions at growing microtubule ends. *BioEssays*, 41(3):e1800194, 2019. doi: 10.1002/bies.201800194.

S. F. van Helden, M. M. Oud, B. Joosten, N. Peterse, C. G. Figdor, and F. N. van Leeuwen. Pge2-mediated podosome loss in dendritic cells is dependent on actomyosin contraction downstream of the rhoa–rho-kinase axis. *Journal of Cell Science*, 121(7):1096–1106, 2008. doi: 10.1242/jcs.020289.

K. Vaughan, S. Tynan, N. Faulkner, C. Echeverri, and R. Vallee. Colocalization of cytoplasmic dynein with dynactin and clip-170 at microtubule distal ends. *Journal of Cell Science*, 112(Pt 10):1437–1447, 1999. doi: 10.1242/jcs.112.10.1437.

C. Vincent, T. Siddiqui, and L. Schlichter. Podosomes in migrating microglia: components and matrix degradation. *Journal of Neuroinflammation*, 9:190, 2012.

A. Viola, F. Munari, R. Sánchez-Rodríguez, T. Scolaro, and A. Castegna. The metabolic signature of macrophage responses. *Frontiers in Immunology*, 10:1462, 2019. doi: 10.3389/fimmu.2019.01462.

B. Voisin, V. Nadella, T. Doebel, S. Goel, K. Sakamoto, O. Ayush, J. Jo, M. Kelly, T. Kobayashi, J. Jiang, Y. Hu, C. Yan, and K. Nagao. Macrophage-mediated extracellular matrix remodeling controls host staphylococcus aureus susceptibility in the skin. *Immunity*, 56(7):1561–1577.e9, 2023. doi: 10.1016/j.immuni.2023.06.006.

N. Wang, L. Hu, and A. Walsh. Evaluation of cellpose segmentation with sequential thresholding for instance segmentation of cytoplasms within autofluorescence images. *Computers in Biology and Medicine*, 179:108846, sep 2024. doi: 10.1016/j.compbiomed.2024.108846.

A. Weaver. Cortactin in tumor invasiveness. *Cancer Letters*, 265:157–166, 2008. doi: 10.1016/j.canlet.2008.02.066.

A. Wegner. Head to tail polymerization of actin. *Journal of Molecular Biology*, 108(1):139–150, 1976. doi: 10.1016/s0022-2836(76)80100-3.

G. Weiss and U. Schaible. Macrophage defense mechanisms against intracellular bacteria. *Immunological Reviews*, 264(1):182–203, 2015. doi: 10.1111/imr.12266.

M. West, A. Prescott, E. Eskelinen, A. Ridley, and C. Watts. Rac is required for constitutive macropinocytosis by dendritic cells but does not control its downregulation. *Current Biology*, 10(14):839–848, jul 2000. doi: 10.1016/s0960-9822(00)00595-9.

C. Wiesner, J. Faix, M. Himmel, F. Bentzien, and S. Linder. Kif5b and kif3a/kif3b kinesins drive mt1-mmp surface exposure, cd44 shedding, and extracellular matrix degradation in primary macrophages. *Blood*, 116(9):1559–1569, 2010. doi: 10.1182/blood-2009-12-257089.

C. Wiesner, K. El Azzouzi, and S. Linder. A specific subset of rabgtpases controls cell surface exposure of mt1-mmp, extracellular matrix degradation and three-dimensional invasion of macrophages. *Journal of Cell Science*, 126(13):2820–2833, jul 2013. doi: 10.1242/jcs.122358.

D. Wloga, D. Webster, K. Rogowski, M. Bré, N. Levilliers, M. Jerka-Dziadosz, C. Janke, S. Dougan, and J. Gaertig. Ttll3 is a tubulin glycine ligase that regulates the assembly of cilia. *Developmental Cell*, 16(6):867–876, 2009. doi: 10.1016/j.devcel.2009.04.008.

D. Worth, C. Daly, S. Geraldo, F. Oozeer, and P. Gordon-Weeks. Drebrin contains a cryptic f-actin-bundling activity regulated by cdk5 phosphorylation. *Journal of Cell Biology*, 202(5):793–806, sep 2013. doi: 10.1083/jcb.201303005.

J. Wu and A. Akhmanova. Microtubule-organizing centers. *Annual Review of Cell and Developmental Biology*, 33:51–75, 2017. doi: 10.1146/annurev-cellbio-100616-060615.

T. Wynn and K. Vannella. Macrophages in tissue repair, regeneration, and fibrosis. *Immunity*, 44(3):450–462, 2016. doi: 10.1016/j.immuni.2016.02.015.

C. Yang, P. Colosi, S. Hugelier, D. Zabezhinsky, M. Lakadamyali, and T. Svitkina. Actin polymerization promotes invagination of flat clathrin-coated lattices in mammalian cells by pushing at lattice edges. *Nature Communications*, 13(1):6127, oct 2022. doi: 10.1038/s41467-022-33852-2.

A. Yildiz. Sorting out microtubule-based transport. *Nature Reviews Molecular Cell Biology*, 22(2):73, 2021. doi: 10.1038/s41580-020-00320-y.

Q. Yu, F. Tang, F. Cao, X. Tan, L. Weng, and L. Sun. Drebrin promotes lung adenocarcinoma cell migration through inducing integrin β1 endocytosis. *Biochemical and Biophysical Research Communications*, 630:175–182, nov 2022. doi: 10.1016/j.bbrc.2022.09.050.

A. Zambonin-Zallone, A. Teti, A. Carano, and P. Marchisio. The distribution of podosomes in osteoclasts cultured on bone laminae: effect of retinol. *Journal of Bone and Mineral Research*, 3:517–523, 1988. doi: 10.1002/jbmr.5650030507.

A. Zambonin-Zallone et al. Immunocytochemical distribution of extracellular matrix receptors in human osteoclasts. *Experimental Cell Research*, 182:645–652, 1989. doi: 10.1016/0014-4827(89)90266-8.

B. Zhao, D. Meka, R. Scharrenberg, T. König, B. Schwanke, O. Kobler, S. Windhorst, M. Kreutz, M. Mikhaylova, and F. Calderon de Anda. Microtubules modulate f-actin dynamics during neuronal polarization. *Scientific Reports*, 7(1):9583, aug 2017. doi: 10.1038/s41598-017-09832-8.

List of Abbreviations

+TIP	plus-end tracking protein
ADFH	actin-depolymerizing factor homology
AFM	atomic force microscopy
AI	artificial intelligence
AP	average precision
Arp2/3	actin-related protein 2/3
ATP	adenosine triphosphate
BSA	bovine serum albumin
CC	coiled-coil
CCS	clathrin-coated structure
CDC42	cell division control protein 42 homolog
CGN	cerebellar granule neuron
CH	calponin homology
CHC	clathrin heavy chain
CLAHE	contrast-limited adaptive histogram equalization
CLASP	cytoplasmic linker-associated protein
CLIP-170	cytoplasmic linker protein-170
CME	clathrin-mediated endocytosis
CML	chronic myeloid leukemia
CUDA	Compute Unified Device Architecture
DDPM	denoising diffusion probabilistic model
DNaseX	deoxyribonuclease-1-like 1
DoU	Difference over Union
DPBS	Dulbecco's Phosphate-Buffered Saline
EB	end-binding
ECM	extracellular matrix
F-actin	filamentous actin

Fiji	Fiji Is Just ImageJ
FLIM	fluorescence lifetime imaging microscopy
FN	false negative
FNR	false negative rate
FP	false positive
FPR	false positive rate
FRAP	fluorescence recovery after photobleaching
FRET	fluorescence resonance energy transfer
G-actin	globular actin
GFP	green fluorescent protein
GPU	graphics processing unit
GTP	guanine triphosphate
GUI	graphical user interface
Hel	helical
INF2	inverted formin 2
IoU	Intersection over Union
KDE	kernel density estimation
LB	lysogeny broth
LCAO	linear combination of atomic orbitals
LLPS	liquid-liquid phase separation
LSP1	lymphocyte-specific protein 1
MAP	microtubule-associated protein
MIP	maximum intensity projection
ML	machine learning
MMP	matrix metalloproteinase
MT	microtubule
MT1-MMP	membrane type 1-matrix metalloproteinase
MTOC	microtubule-organizing center
NADPH	nicotinamide adenine dinucleotide phosphate
NGS	normal goat serum
NHS	normal horse serum
Nox4	NADPH oxidase 4
OME-TIFF	Open Microscopy Environment TIFF
PBS	phosphate-buffered saline

PCP	podosome cluster precursor
PCR	polymerase chain reaction
PFA	paraformaldehyde
PLA	proximity ligation assay
PP	polyproline
PRR	pattern recognition receptor
PTM	post-translational modification
Pyk2	protein tyrosine kinase 2 beta
p190RhoGAP	p190 Rho GTPase-activating protein
Rho	Ras homolog
RhoA	Ras homolog family member A
RNS	reactive nitrogen species
ROI	region of interest
ROS	reactive oxygen species
RPMI	Roswell Park Memorial Institute medium
SBML	Systems Biology Markup Language
SR-CLEM	super-resolution correlative light and electron microscopy
TAE	Tris-acetate-EDTA
TAM	tumor-associated macrophage
TPU	tensor processing unit
WAS	Wiskott-Aldrich syndrome
WASP	Wiskott-Aldrich syndrome protein
XLA	accelerated linear algebra

A   Supplementary Figures
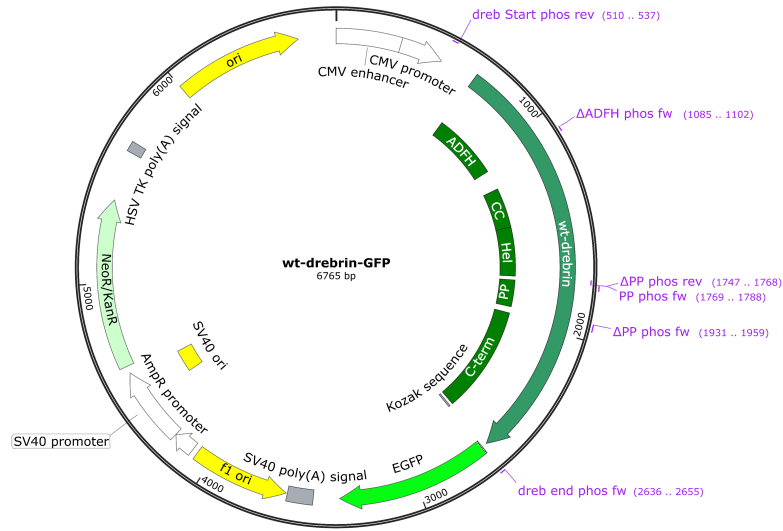
Figure A.1: **Vector map of *wt-drebrin-GFP*.** The construct is driven by a *CMV* promoter and encodes wild-type drebrin with annotated subdomains: actin-depolymerising factor homology (ADFH), coiled-coil (CC), helical (Hel), polyproline (PP), and the C-terminal region. A GFP tag is fused to the C-terminus to enable visualization of the protein (Peitsch et al., 2005).
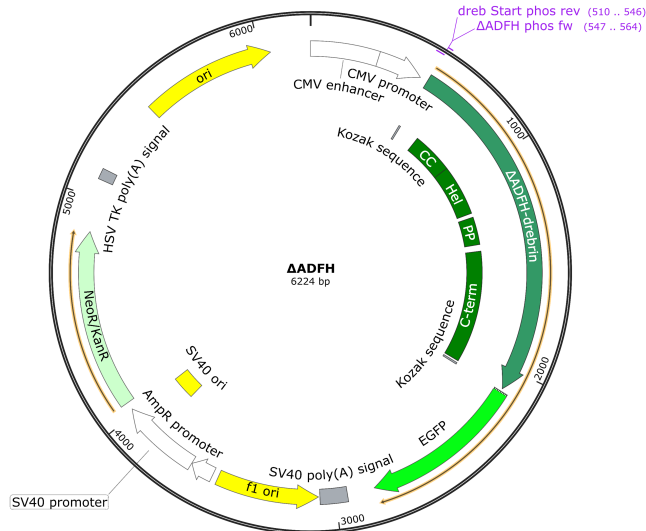
Figure A.2: **Vector map of $\Delta ADFH$-GFP.** The construct is driven by a *CMV* promoter and encodes drebrin lacking the actin-depolymerising factor homology (ADFH) domain. Remaining subdomains include coiled-coil (CC), helical (Hel), polyproline (PP), and the C-terminal region. A GFP tag is fused to the C-terminus for protein visualization.
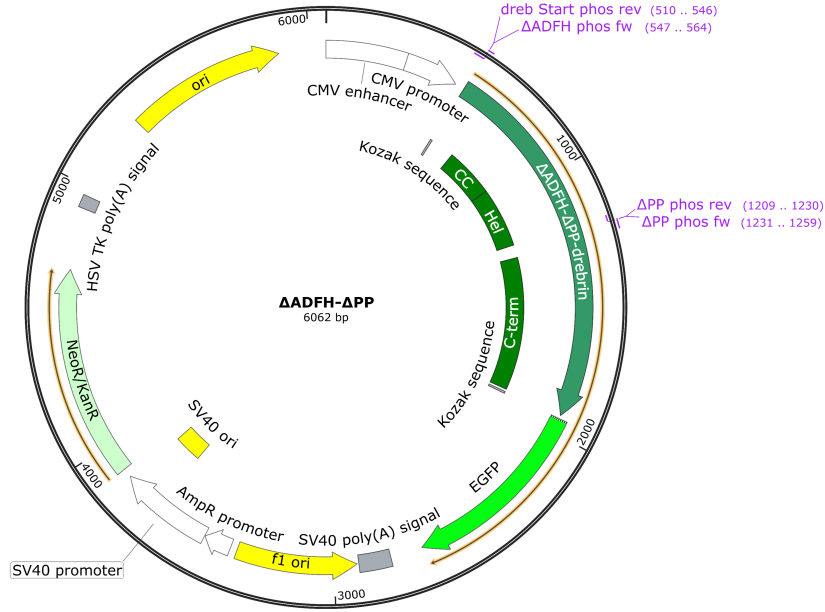
Figure A.3: **Vector map of $\Delta ADFH$-ΔPP-drebrin-GFP.** The construct is driven by a *CMV* promoter and encodes drebrin with deletions in both the actin-depolymerising factor homology (ADFH) and polyproline (PP) domains. Remaining subdomains include coiled-coil (CC), helical (Hel), and the C-terminal region. A GFP tag is fused to the C-terminus for visualization.
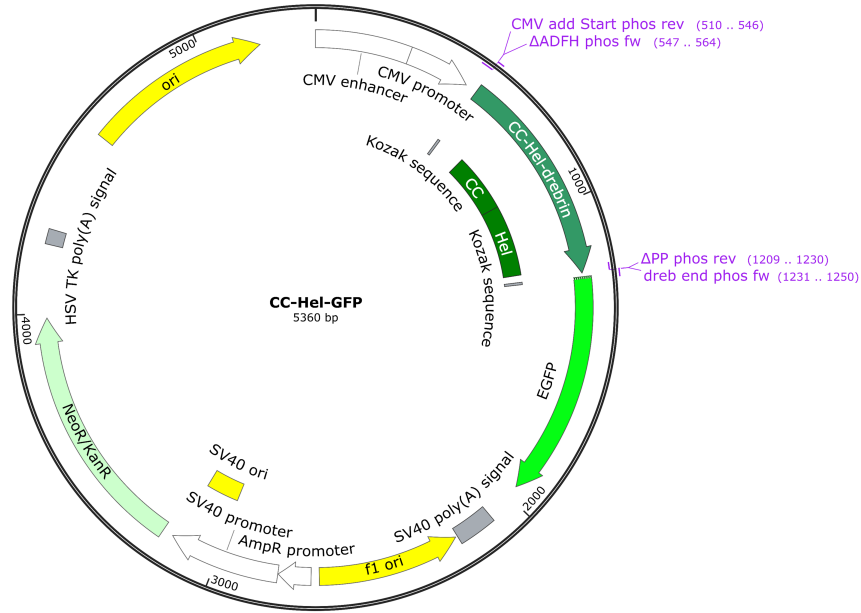
Figure A.4: **Vector map of *CC-Hel-GFP*.** The construct is driven by a *CMV* promoter and encodes a truncated version of drebrin containing only the coiled-coil (CC) and helical (Hel) subdomains. The ADFH, polyproline (PP), and C-terminal regions are deleted. A GFP tag is fused to the C-terminus to enable protein visualization.
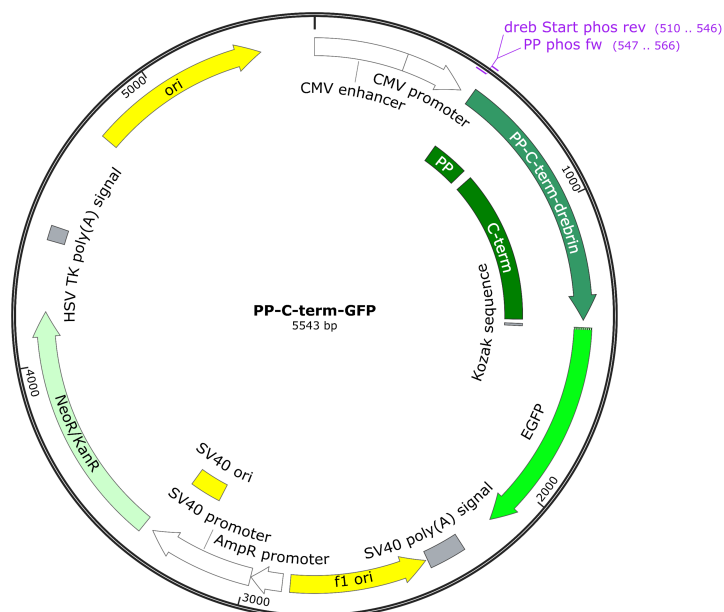
Figure A.5: **Vector map of *PP-C-term-GFP*.** The construct is driven by a *CMV* promoter and encodes a truncated version of drebrin containing only the polyproline (PP) and C-terminal regions. The ADFH, coiled-coil (CC), and helical (Hel) domains are deleted. A GFP tag is fused to the C-terminus to allow visualization of the expressed protein.
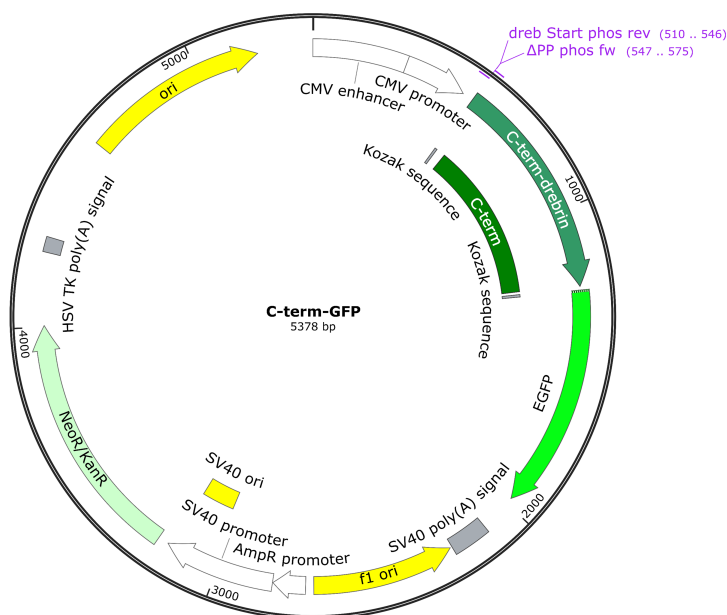
Figure A.6: **Vector map of *C-term-GFP*.** The construct is driven by a *CMV* promoter and encodes a truncated version of drebrin containing only the C-terminal region. All other domains - actin-depolymerising factor homology (ADFH), coiled-coil (CC), helical (Hel), and polyproline (PP) - are deleted. A GFP tag is fused to the C-terminus for protein visualization.
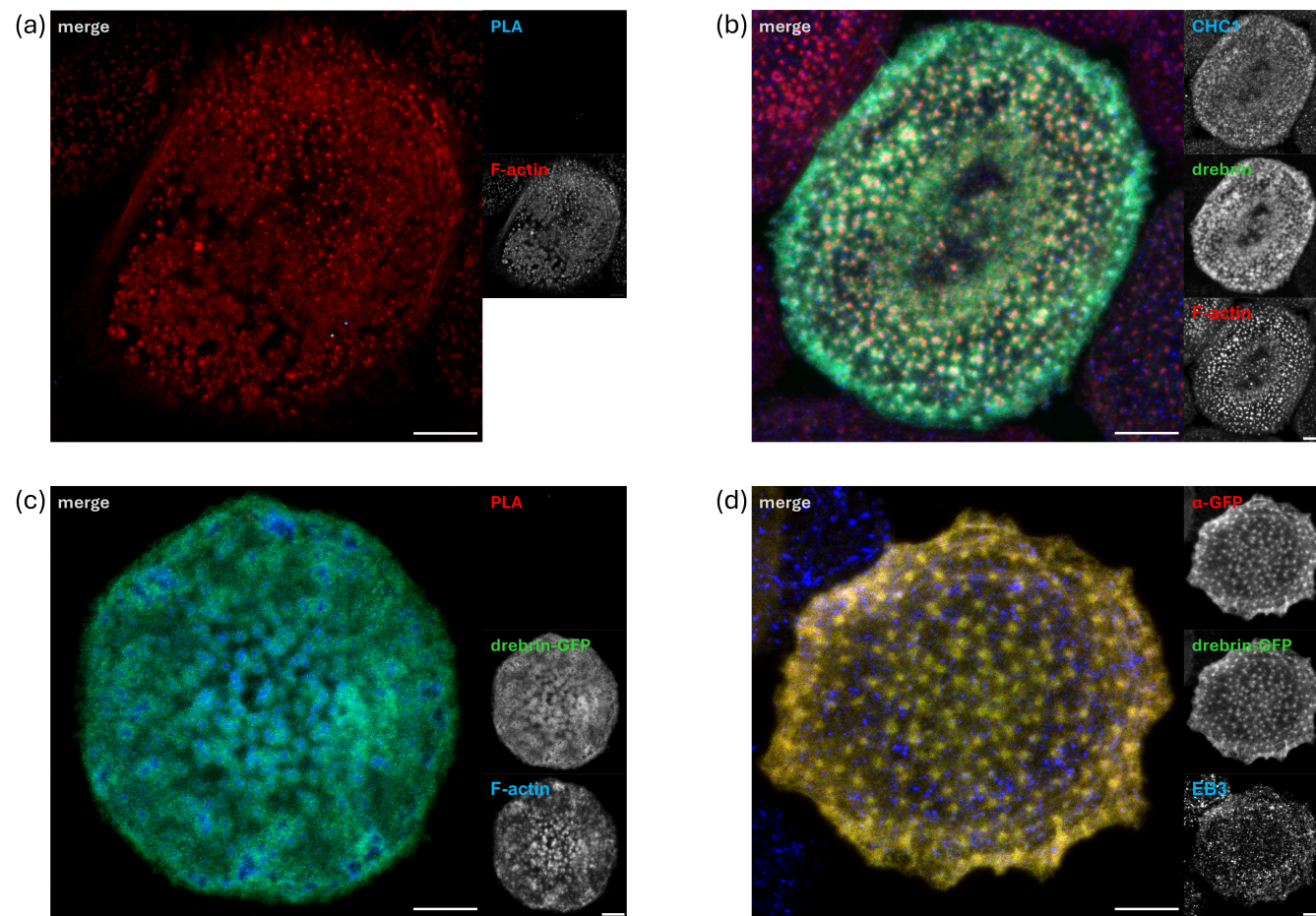
Figure A.7: **Controls for PLA signal and antibody specificity.** (a) Isotype control for clathrin–drebrin PLA using a mouse isotype antibody in place of anti-clathrin, showing merged and single-channel images (PLA: blue, drebrin: green, F-actin: red). (b) Antibody specificity control for clathrin and drebrin immunostaining, showing CHC1 (blue), drebrin (green), and F-actin (red), with minimal background signal. (c) Isotype control for drebrin-GFP-EB3 PLA with mouse isotype antibody replacing anti-GFP, showing merged and single-channel images (PLA: red, drebrin-GFP: green, F-actin: blue). (d) Antibody specificity control for drebrin-GFP and EB3, showing anti-GFP (red), drebrin-GFP (green), and EB3 (blue); overlap of red and green confirms GFP antibody specificity, while EB3 staining shows minimal background. All panels are maximum intensity projections from confocal z-stacks. Scale bars: 5 μm.

List of Figures

List of Tables

List of Equations